MATHEMATICAL MODELS FOR UNDER-DEPOSIT CORROSION IN AERATED AND DE-AERATED SOLUTIONS

By

YA-CHIAO CHANG

A DISSERTATION PRESENTED TO THE GRADUATE SCHOOL
OF THE UNIVERSITY OF FLORIDA IN PARTIAL FULFILLMENT
OF THE REQUIREMENTS FOR THE DEGREE OF
DOCTOR OF PHILOSOPHY

UNIVERSITY OF FLORIDA

2013

To my parents and my husband

ACKNOWLEDGMENTS

I thank my advisor, Professor Mark E. Orazem, for his expertise, guidance, and support in this work. He has shown me not only how to improve my abilities in research, but how to improve my abilities as a person with his unmatched patience. I would like to thank Richard Woollam of BP America for his involvement in sponsoring this project. I also thank my committee members Professor Anuj Chauhan, Professor Loc Vu-Quoc, and Professor Kirk Ziegler. I would like to thank all of the students and post-doc who have worked in Professor Orazem's group during my time at University of Florida. Finally, I would like to thank my husband, my parents, my brother, and my grandfather for their love and encouragement during my studies.

TABLE OF CONTENTS

LIST OF TABLES

LIST OF FIGURES

LIST OF SYMBOLS

a_r	activity of the reacting species
A	surface area, m^2
A_1	constant used for the Eddy diffusivity term to describe the turbulent flow
A_2	constant used for the Eddy diffusivity term to describe the turbulent flow
A_p	constant used for the active-passive transition
b_a	anodic coefficient, V^{-1}
b_c	cathodic coefficient, V^{-1}
c_i	molar concentration of species i, mol/liter
$c_{i,ref}$	bulk concentration of species i, mol/liter
c_r	molar concentration for reactants, mol/liter
c_p	molar concentration for products, mol/liter
D_i	diffusion coefficient for species i, cm^2/s
$D_{i,covered}$	effective diffusion coefficient of species i in the covered region, cm^2/s
$D_{i,bulk}$	effective diffusion coefficient of species i in the bulk region, cm^2/s
$D_i^{(t)}$	position-depend, cm^2/s
E_a	activation energy, V
E_p	potential at which the active-passive transition occurs, V
F	Faraday's constant, 96487 C/equiv
H_i	Henry's constant
i	current density, mA/cm^2

i_0	exchange current density, mA/cm^2
i_a	anodic current density, mA/cm^2
i_c	cathodic current density, mA/cm^2
i_{ct}	charge transfer current density, mA/cm^2
i_k	kinetically controlled current density, mA/cm^2
i_{lim}	mass-transfer-limited current density, mA/cm^2
i_p	passive current density, mA/cm^2
k	rate constant for electrochemical reaction that excludes the exponential dependence on potential
k_f	rate constant in forward reaction
k_b	rate constant in backward reaction
k_j	rate constant of the formation of scale j
$K_{sp,i}$	solubility product of salt i
K_w	dissociation constant for water, mol^2/kg^2
K_{sol}	kinetic constant for the dissolved rate of CO_2
K_i	dissociation constant for water, mol^2/kg^2
N_i	flux of species i, mol/cm^2 s
P_{CO_2}	carbon dioxide partial pressure, bar
R	universal gas constant, 8.3143 J/mol K
R_i	rate of reaction, mol/cm^2 s
r	radial coordinate, m
T	temperature, K
t	time, s
U_i	equilibrium potential for a given reaction, V

v velocity, cm/s

V interfacial potential under equilibrium conditions for a given reaction

z_i charge associated with species i

z^+ dimensionless distance from the metal surface

β Tafel slope, V/decade of current

Γ surface concentration of species

γ fractional surface coverage

δ thickness, cm

ϵ porosity

ε error

η overpotential for a given reaction, V

θ radial coordinate

κ conductivity

λ parameter that controls the steepness of the potential change corresponding to the active-passive transition

ν kinematic viscosity, cm^2/s

ξ potential-dependent weighting factor

ρ fluid density, g/cm^3

ρ_s precipitates density, g/cm^3

τ_o wall shear stress, N/cm^2

ϕ radial coordinate

Φ potential, V

Φ_0 potential of the electrolyte adjacent to the working electrode, V

Φ_m electrode potential, V

Abstract of Dissertation Presented to the Graduate School
of the University of Florida in Partial Fulfillment of the
Requirements for the Degree of Doctor of Philosophy

MATHEMATICAL MODELS FOR UNDER-DEPOSIT CORROSION IN AERATED AND DE-AERATED SOLUTIONS

By

Ya-Chiao Chang

December 2013

Chair: Mark E. Orazem
Major: Chemical Engineering

A 2-D axi-symmetric time-dependent mathematical model was developed to investigate conditions under which the onset of under-deposit corrosion occurs. Model development is presented sequentially. The systems considered included steels in both aerated water and de-aerated electrolyte containing CO_2. One unique feature of this work was that, the presence of anodic and cathodic regions was not assumed *a priori*, but was rather the result of numerical simulations, which revealed galvanic coupling caused by the differential aeration cells. In contrast to models presented in the literature, the conservation equation for each ionic species was employed in this work rather than Laplace's equation. Two geometries were considered. An one-quarter-ellipse geometry was used to describe a water droplet placed on the bare metal surface; whereas, a two-quarter-ellipse geometry was used to represent a predefined deposit surrounded by a bulk solution. Solutions containing O_2 and CO_2 were calculated in both geometries. Two types of precipitates are discussed in the models containing O_2. The precipitate $Fe(OH)_2$ was assumed to be less protective and to inhibit both anodic and cathodic reactions; whereas, $Fe(OH)_3$ was assumed to be protective and to passivate only the iron dissolution reaction. The species $FeCO_3$ was assumed to be the precipitate in the system containing CO_2, which involved additional homogeneous and cathodic reactions.

The results were sensitive to both mesh size and time step size. For the

two-quarter-ellipse geometry models, the area ratio of the covered region to the bare metal surface was found to be important since it influences the location and rate of anodic and cathodic reactions. A systematic study was performed to identify the proper modeling parameters.

The mathematical model included coupled, time-dependent, nonlinear, convective diffusion equations for ionic species; local electroneutrality; homogeneous reactions; formation of primary precipitates; and anodic and cathodic reactions written explicitly in terms of local concentration and potential driving forces. It provides a framework for modeling systems involving homogeneous and heterogeneous reactions and, with simple modifications, can apply to different conditions. The results showed under-deposit corrosion occurs and can lead to more serious problems under some conditions.

CHAPTER 1
INTRODUCTION

On August 19 2000, a 30-inch-diameter natural gas pipeline ruptured near Carlsbd, New Mexico. Twelve lives were claimed by the explosion and fire. The significant reduction in pipe wall thickness resulted from internal corrosion caused this accident. This finding was confirmed by the National Transportation Safety Board [1]. The report pointed out that the combination of microbial films and contaminants such as O_2, CO_2, H_2S, and chlorides initiated the internal corrosion. Catastrophic incidents due to internal corrosion in oil and gas industry are not rare. In the United States, the total annual cost of corrosion-related incidents in gas and oil industry is from 471 to 875 million [2].

The control techniques to prevent internal corrosion have not been improved since 1970s. The current examination involves running an instrumented pig through the pipe using ultrasound techniques to measure wall thickness [3, 4]. However, these can not prevent the incident mentioned above because it is difficult to identify and repair damage covered with corrosive products. Therefore, it is important to build a mathematic model to predict the corrosion and define a limitation to the use of steel pipelines.

The recognition of the internal corrosion problem begins in 1940s and the models have been developed since the mid 1970s. These models can be classified as empirical, semi-empirical, and mechanical, as shown in Table 1-1.

Both empirical and semi-empirical models can provide accurate prediction, but these models require complicated correction factors when new operating parameters are considered, thereby limiting the applicability of the model. Most models focus on the uniform corrosion on metal surface to reduce the complexity of calculation; however, localized corrosion is commonly observed. Under-deposit corrosion is a type of localized corrosion that can lead to a catastrophic consequence due to the lack of predictability. In order to improve present models, a computational model was developed that accounts

for the initial under-deposit environment, mechanisms of the formation of differential cell, the structure of protective film, and chemical reactions associated with O_2 and CO_2.

Under-deposit corrosion containing corrosive species can lead to more serious types of corrosion. The mechanism for the onset of localized corrosion has been studied by many industrial and academic research groups. CORMED [5], Norsok [5], and deWaards [6] built empirical and semi-empirical models that can provide accurate interpolation prediction for corrosion rate; however, more complicated correction factors are required to account for situations where extrapolation or prediction fails. Mechanistic models developed by Gray [7], Nesic [8, 9], and Anderko [10] are based on fundamental theories, but the assumption of predefined anodic and cathodic regions introduces errors in the predicted corrosion rates. In this work, in order to construct a model providing more information of the corrosion mechanisms, the presence of anodic and cathodic regions was determined by local potential distribution caused by the formation of differential aeration cells.

The object of this work is to present a 2-D axi-symmetric time-dependant mathematical model investigating conditions under which the onset of under-deposit corrosion occurs in aerated and de-aerated media. The active-passive transitions of metals like iron was assumed to be the consequence of formation of precipitate. The fluid dynamic was also taken into account by using the eddy diffusivity. The model development will be introduced sequentially in this work. In contrast to previous models, the location of anodic and cathodic regions was not assumed *a priori*, but was rather the result of the numerical simulation. This model also includes the galvanic coupling effect resulted from the formation of precipitates. The conservation equation for each ionic species was employed in this work rather than Laplace's equation. The present study simulates the corrosion process by using fundamental physical and electrochemical laws which providing a framework of understanding the concentration variation of reacting species in the solution. The advantage of this model is it can be adapted to other types

of corrosion with simple modifications. More complicated reactions involving several reaction species such as H_2S and HS^-, more corrosive environment containing Cl^-, and other geometries can be addressed in future work.

Table 1-1. Comparison of prediction models for CO_2/H_2S corrosion.

Model type	Features	Example
Empirical	• provides accurate interpolation prediction • extrapolation prediction failed • parameters are best-fit	CORMED [5] 1980s Norsok [5] 1990s
Semi-empirical	• provides good interpolation prediction • extrapolation prediction may be incorrect • some parameters have physical meanings while others are best-fit	de Waards [5, 6] 1975
Mechanistic	• provide good extrapolation as interpolation prediction	
Electrochemical	• strong theoretical background	Gray [7] 1989
Transport-based		Nesic [9, 11] 1996, 2001
Thermodynamic-based		Anderko [10] 1998

CHAPTER 2
LITERATURE REVIEW

The basic concept of under-deposit corrosion is introduced in sequence as follows, including the mechanism of localized corrosion, properties of differential cells, and the influence of CO_2 and H_2S under humidified condition. Finally, a review of mechanistic models proposed in the past decades is presented.

2.1 Localized and Under-Deposit Corrosion

Internal corrosion can be categorized into two types. One is uniform corrosion which is easy to foresee and can be repaired before an incident occurs. Another is localized corrosion such as pitting, stress corrosion cracking, crevice corrosion, erosion, and...etc Under-deposit corrosion is a type of localized corrosion and will be discussed in this work.

A common cause of ruptured oil and gas pipelines is under-deposit corrosion which is a type of localized corrosion. It is hard to observe because the pit or crevice is often buried under sands or corrosive products. Once it is detected, surface damage is already significant. The onset of under-deposit corrosion is generally explained by the imperfection of corrosion products on a metal surface. The imperfection mostly is associated with the breakdown of the protective scale resulted from the fluid flow [12–14]. Once the metal potential achieves a critical value, the localized corrosion is initiated and leads to more serious problems such as pitting corrosion [15–17]. At the same time, the electrochemistry and the transport process on the metal surface begin to differ from the bulk system [18]. Many attempts have been made to develop a small-scale, inexpensive, and efficient method to simulate the environment in pipelines [19–21]. Models for initiation of localized corrosion are based on concepts associated with transport of species through the passive film and in the occluded region. Alkire et al. [22] developed a simple model neglecting electromigration and considering the transport of the neutral binary electrolytes. Alkire and Siitari revealed that potential and

concentration distributions could be altered by introducing a cathodic reaction inside the pit [23]. Under-deposit corrosion, on the other hand, has been associated with formation of differential cells.

2.2 Differential Cell

Differential cells represent a type of concentration cells in which electrochemical reactions are driven by concentration differences of species between two metals or two points on the same metal surface. The precipitation layer acts as a barrier to reactive species and leads to different reaction rates because of the non-uniform surface. In the oil and gas industry, water reduction and iron dissolution are the common redox reactions. When the surface covered with corrosive products or a cluster of microbes leads to oxygen depletions, the anodic reaction rate increases. On the other hand, the cathodic reaction dominates on the surface without precipitation layers. Differential aeration cells are introduced as an example of differential cell in the following. This situation is seen in Figure 2-1A where the contributions of oxygen reduction and

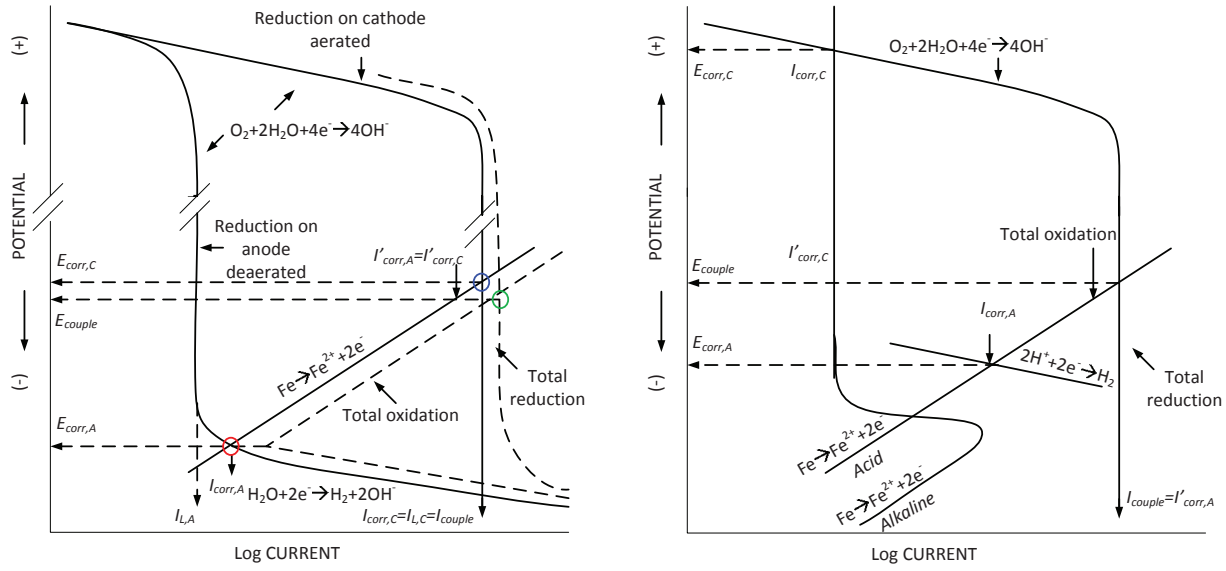

Figure 2-1. Mixed potential analysis for the differential aeration cell : A) under the assumption of uniform electrolyte compositions and current distributions B) with a passivated cathode.

corrosion reactions are given as solid lines.

Many metals like iron, chromium, nickel, titanium and their alloys demonstrate an active-passive transition, which is influenced by the electrolyte pH. The corresponding diagram is given in Figure 2-1B. Two corrosion lines are drawn, one for the acidic electrolyte and the other for the alkaline electrolyte. The substantial difference of corrosion rate between anode and cathode expresses an acceleration of corrosion by the differential aeration effect. Evans [24] demonstrated a water droplet experiment showing the effect accelerates the corrosion near a water line on a metal surface. Other factors such as a restricted access of inhibitors and retention of corrosive species can also increase the under-deposit corrosion rate [25, 26]. Alkire et al. [27] developed a model to calculate current distributions on a metal subjected to differential aeration corrosion. LaQue [28, 29] showed that copper disks corroded along the periphery where the flow was turbulent and the rate of transport of oxygen was higher. Conversely, the iron disks spinning under same conditions corroded at the center where the flow was laminar and decelerated transport of oxygen. The active-passive transition and the distribution of corrosion rate are related to the electrode size, oxygen concentration, and solution conductivity [30, 31]. Good agreement was obtained between calculations and experimental observations [28, 29]. Orazem and Miller [32] proposed that oscillation of current near the passivation potential results from the formation of salt films.

2.3 Corrosion in Presence of Carbon Dioxide

The environment can influence the rate of under-deposit corrosion, especially CO_2 and H_2S in a moisturized condition. The history of studying corrosion in CO_2 containing environment can be traced back to 1940s when this was first found in gas and sweet-oil wells. As recognized, carbonic acid is more corrosive than a completely dissociated acid at the same condition (pH value) [6]. The causes have been investigated extensively by many academic and industrial groups over the past decades [7, 33–35]. Depending on the influence, the factors can be sorted into three categories, medium-related,

Table 2-1. Factors influencing corrosion in CO_2 containing environments [34–36].

Medium-related		Material-related	Interface-related
CO_2 partial pressure	O_2 content	Alloy composition	Temperature
pH value	Fe^{2+} concentration	Microstructure	Fluid flow rate
Sour gas (H_2S)	Brine composition		Multiphase flow
Organic acid (HAc)	Crude Oil		Surface films
			Water wetting

materials-related, and interface-related [36]. These parameters are listed in Table 2-1. These factors are all interconnected and have a direct or indirect impact on mechanisms. For example, the partial pressure of CO_2 directly affects the pH value of the medium, which can alter mechanisms. At higher pH value or higher temperature, a film of iron carbonate is more likely to form, protecting the metal surface and affecting the corrosion rate indirectly [8]. Similarly, the precipitation rate varies according to fluid flow by changing the degree of water-wetting on a metal surface.

The presence of H_2S plays an significant role in the CO_2 containing corrosion because it increases the corrosion potential to a region where localized breakdown and pitting corrosion could occur. The effect is complex due to the co-existence of two competitive products, $FeCO_3$ and FeS [37]. Corrosion containing H_2S has been studied since 1950s. It can accelerate the corrosion rate by giving out additional H^+ ions or decelerate the corrosion rate by forming a thin protective film [6, 38, 39]. On the contrary, several studies showed that as concentration of H_2S less than 500ppm at pH (< 5), there is no precipitation layer on a metal surface. After the concentration exceeds a critical value, the corrosion rate decreases [40, 41]. Moreover, the effect due to temperature change is more significant than the concentration gradient of H_2S [41]. The corrosion behavior of steel in the presence of carbon dioxide and acetic acid have been studied [42]. The effect of the existence of CH_3COOH can be observed at elevated temperatures and the undissociated form of acetic acid can lead to an increasing corrosion rate.

Generally, local defects form a difference of corrosion activities and are commonly believed to serve as the initiator. A microturbulence flow is introduced by an uneven scale on a metal. When hydrodynamic forces reach a critical value known as wall shear stresses, a rupture of the protective scale starts. The study of corrosion in a presence of CO_2 and H_2S involves a combination of all the above factors.

2.4 Review of Mechanistic Models

The elaboration of mechanistic models require strong physical and chemical foundations. The mechanistic models have been classified into three categories, electrochemical, transport-based electrochemical, and thermodynamically-based electrochemical.

2.4.1 Electrochemical Models

The corrosion rate is affected by redox reactions which include anodic dissolution of the metal and cathodic reactions such as evolution of hydrogen or reduction of oxygen. Since iron is a major component in pipelines, the most common anodic reaction is iron dissolution given by [43, 44]

$$\mathrm{Fe} \rightarrow \mathrm{Fe}^{2+} + 2\mathrm{e}^{-} \tag{2–1}$$

One of the cathodic reactions is hydrogen evolution. The hydrogen can be evolved directly from water [45], carbonic acid [9], and acetic acid [42] as described below

$$\mathrm{H_2O} + \mathrm{e}^{-} \rightarrow \frac{1}{2}\mathrm{H_{2(g)}} + \mathrm{OH}^{-} \tag{2–2}$$

$$\mathrm{H_2CO_3} + \mathrm{e}^{-} \rightarrow \frac{1}{2}\mathrm{H_{2(g)}} + \mathrm{HCO_3^{-}} \tag{2–3}$$

and

$$\mathrm{HAc} + \mathrm{e}^{-} \rightarrow \frac{1}{2}\mathrm{H_{2(g)}} + \mathrm{Ac}^{-} \tag{2–4}$$

The current of individual reactions can be formulated as

$$\frac{1}{i_k} = \frac{1}{i_{k,\mathrm{ct}}} + \frac{1}{i_{k,\mathrm{lim}}} \tag{2–5}$$

where the subscript k represents the k_{th} reaction, $i_{k,\mathrm{ct}}$ is charge-transfer current, and $i_{k,\mathrm{lim}}$ is mass transfer-limited current. For the charge transfer steps, $i_{ct,\mathrm{a}}$ and $i_{ct,\mathrm{c}}$ can be expressed by

$$i_{\mathrm{ct},a} = i_{0,a} 10^{\eta/b_a} \tag{2–6}$$

and

$$i_{\mathrm{ct},c} = -i_{0,c} 10^{-\eta/b_c} \tag{2–7}$$

respectively, where η is overpotential, i_0 is exchange current density, and b is Tafel slope for each reaction. There is no limiting current for iron dissolution and water reduction because the unlimited quantity of iron in the metal and water molecular in bulk solution. For the acetic acid reduction, the current is limited by the diffusion of reacting species to the metal surface. Because of the specific property of carbonic acid, the dehydration degree of carbonic acid should be incorporated [46].

After all the parameters are specified, the corrosion potential and current density can be solved through the charge balance at steady state

$$\sum i_k = 0 \tag{2–8}$$

The corrosion rate can therefore be calculated from the anodic current density.

2.4.2 Transport-Based Electrochemical

In the electrochemical model, the transport process is simplified by assuming a linear distribution of concentration through a stagnant boundary layer. However, the corrosion behavior changes when a layer is formed. Therefore, the transport of reacting species through the layer of corrosive products should be incorporated to derive a more practical model [47, 48].

The driving force of species in an aqueous solution can be classified by three sources: convection if a species is moving with the fluid velocity $\mathbf{v}$, diffusion if there is a difference in concentration ∇c_i, and migration if a species has charge z_i and is under a

potential gradient $-\nabla\Phi$. The flux of a species i can be expressed by

$$\mathbf{N}_i = -\frac{F}{RT} z_i D_i c_i \nabla\Phi - D_i \nabla c_i + c_i \mathbf{v} \tag{2–9}$$

The relationship between current and charged species is

$$\mathbf{i} = F \sum_i z_i \mathbf{N}_i \tag{2–10}$$

Each species is conserved and can be written as a combination equation of homogeneous chemical reactions and the flux of species.

$$\frac{\partial c_i}{\partial t} = -\nabla \cdot \mathbf{N}_i + R_i \tag{2–11}$$

R_i is the source of i species resulting from homogeneous reactions and can be expressed as

$$R_i = k_f \prod_r c_r - k_b \prod_p c_p \tag{2–12}$$

where k_f and k_b are the rate constants for forward and backward reactions, and c_r and c_p are the concentration for reactants and products, respectively. In a CO_2 containing solution, the homogeneous reactions could be hydration of CO_2, dissociation of water and other organic acids, and the formation of protective film [49].

For an aqueous solution containing n solutes, there are n expressions in the form of Equation 2–11. The electroneutrality equation

$$\sum_i^n z_i c_i = 0 \tag{2–13}$$

is needed to calculate the electrical potential Φ. The migration term in Equation 2–9 is negligible if the electrolyte is supported by an inert ionic species [50]. The mass conservation for the species in bulk solution can be presented by [47, 51]

$$\frac{\partial(\epsilon c_i)}{\partial t} = \frac{\partial}{\partial x}\left[\epsilon^{1.5}(D_i + D_i^{(t)})\frac{\partial c_i}{\partial x}\right] + \epsilon R_i \tag{2–14}$$

where $D_i^{(t)}$ is a position-dependent turbulent eddy diffusivity and ϵ is volumetric porosity of the film.

The electrochemical reactions are coupled to the transport equations through the boundary conditions. The corrosion rate can be obtained after the concentration profile is solved.

2.4.3 Thermodynamically-Based Electrochemical

The two mechanistic models described above are restricted to an ideal solution. The thermodynamics of solutions is added to include the effect of interactions among solutes. It is capable of calculating the equilibria of liquid phase, oil phase, and several solid phases in a multi-component system [10, 52].

The concentration of reacting species in the previous electrochemical reactions is replaced by activity a_i. The exchange current density can be formulated as

$$i_{0,k} = i^*_{0,k} \prod_r a_r^m a_{H_2O}^n \tag{2–15}$$

where i_0 is the concentration-independent part, and m and n are the reaction orders related to the activities of the reacting species and water.

If the film is formed, a precipitation rate should be considered and is given by [52, 53]

$$R_j = k_{j,f} \prod_i \Gamma_i^{n_i} \tag{2–16}$$

where $k_{j,f}$ represents the rate constant of the formation of scale j, Γ_i is the surface concentration of species i which is responsible for the precipitation reaction, and n_i is the reaction order. Since the anodic dissolution and cathodic reactions are assumed to take place only on the uncovered region, the partial current is introduced as a function of surface coverage by [53]

$$i' = i \left(1 - \sum_j \gamma_j \right) \tag{2–17}$$

where γ_j is the fraction of the surface covered by scale j.

This calculation can achieve good agreement with experimental results over a certain range of temperature, however, it neglects the influence of localized corrosion resulting from the partially covered metal. Therefore, this simplified model should be extended to predict corrosion inside pipelines in oil and gas industry.

CHAPTER 3
NUMERICAL APPROACH

Under-deposit corrosion is a type of localized corrosion that can lead to a catastrophic consequence in gas and oil industry. Many models for corrosion in fluids containing CO_2 have been developed [5–10]. Most empirical and semi-empirical models can provide accurate interpolation prediction for corrosion rate; however, more complicated correction factors are required to account for situations where extrapolation or prediction fails. Other models based on mechanistic models pre-defined the anodic and cathodic regions and may, therefore, introduces errors in the predicted corrosion rate. In this work, in order to construct a model providing more information of the corrosion mechanisms, the presence of anodic and cathodic regions was determined by local potential distribution caused by the formation of differential cells.

The object of this work is to present a 2-D axi-symmetric mathematical model that can be used to investigate conditions under which the onset of under-deposit corrosion occurs in both aerated (containing dissolved O_2) and de-aerated (containing dissolved CO_2) media. Model development is presented sequentially. In contrast to previous models, the location of anodic and cathodic regions was not assumed *a priori*, but was rather the result of the numerical simulation. The present study simulates the corrosion process by using fundamental physical and electrochemical laws which providing a framework of understanding the concentration variation of reacting species in the solution. The advantage of this model is it can be adapted to other types of corrosion with simple modifications. More complicated reactions involving several reaction species such as HS^- and H_2S can be addressed in future work.

3.1 Problem Description

Many attempts have been made to propose a mechanism for the localized corrosion resulting from the breakdown of scales on a metal surface for the solutions containing O_2 and CO_2. However, several essential properties of under-deposit corrosion such

as the formation of concentration cells and the transport of reacting species through a diffusion barrier have been neglected. In addition, a transient analysis is required to predict the time frame for corrosion failure.

3.1.1 Aerated Solution (O_2)

Generally, oxygen has high affinity to form a stable oxide layer (normally micrometers thick), which provides inertness to corrosive environment. However, the protection against the corrosive media can be destroyed by the chemical or physical heterogeneity at the surface such as a crack or a defect. Once the critical acidification and the corrosion potential are reached, localized corrosion is initiated. Metal dissolution promotes the growth of pits with oxygen reduction outside the pit. Sands and precipitations formed in the bulk solution can be transported by the fluids in pipelines and deposit on the metal surface. Under the deposit, if the oxygen concentration becomes significantly less than that in the bulk, differential aeration (or concentration) cells are generated. In this work, the corrosion rate is proportional to the difference between the oxygen content in under-deposit area and bulk system. Therefore, understanding the diffusion process in the diffusion barrier is a good starting point for studying the under-deposit corrosion since the diffusion of reacting species through a porous deposit layer has a great effect on the localized corrosion beneath deposit.

Model development took place through a sequence of models of increasing complexities. To understand the concentration variation of oxygen on the electrode surface, oxygen diffusion to a metal surface in a water droplet was modeled. Metal dissolution can occur in the region under deposit where oxygen is depleted. Oxygen reduction takes place in the oxygen-rich area. The anodic and cathodic region are formed due to the local environmental differences. Two types of precipitates were assumed to be form in the solutions containing dissolved O_2: $Fe(OH)_2$ was assumed to be the primary precipitate and less protective and the other one is $Fe(OH)_3$ which was assumed to be protective. To model the diffusion process through a diffusion barrier

such as a porous layer, a layer of loosely-packed sands can be employed instead of the water droplet. In order to construct a general model which can provide an more accurate prediction of the under-deposit corrosion rate, different environment, types of deposit, and reactions involving several reaction species such as CO_2, HCO_3^-, and CO_3^{2-} were taken into account in the de-aerated media.

3.1.2 De-aerated Solution (CO_2)

In pipelines, sands and precipitations formed in the bulk solution can be transported by the fluids and deposit on the metal surface. Under-deposit corrosion model in aerated solution provides us a framework to study condition containg CO_2 and the approaches used in O_2 models were implemented into the CO_2 models. Under the deposit in a solution containing CO_2, if the CO_2 concentration becomes significantly less than that in the bulk, concentration cells are generated. The dissociation product (i.e., CO_3^{-2}) has high affinity to form a stable carbonate layer, which provides inertness to corrosive environment. However, the uneven distribution of the deposition of corrosion products could form another concentration cell and enhance corrosion rate.

Model development takes place through a sequence of steps of increasing complexities. For solutions containing dissolved carbon dioxide, it comprises CO_2, HCO_3^-, CO_3^{2-}, H^+, and OH^-. A change of acidity is the consequence of the dissociation of carbonic acid. The rates of dissociations are also dependant on the value of pH; therefore, a corrected prediction of local pH value is important. In comparison with strong acid solutions at the same pH, the corrosion rate is enhanced in de-aerated solutions containing dissolved CO_2 [34]. A large number of mechanisms of the dissociation of carbonic acid have been proposed [6, 7, 9, 34, 54–57]. Two mechanisms were studied in this work. Nordsveen [47] considered the presence of H_2CO_3 and its contribution to the cathodic reaction by including the hydration reaction of CO_2. The direct reduction of H_2CO_3 and H^+ are both considered in the cathodic reactions of the CO_2 models. The hydration of CO_2 and two dissociation steps of H_2CO_3 are

also considered. To understand the concentration variation of H^+ on the electrode surface and the two dissociation steps of H_2CO_3, CO_2 diffusion to a metal surface in a water droplet was modeled. Remita et al. [58] assumed the reaction rate of the first deprotonation reaction is fast enough to ignore the existence of H_2CO_3 and only hydrogen evolution was considered in the cathodic reaction. Metal dissolution was preferred in the region under deposit where H_2CO_3 and H^+ were depleted. Until enough Fe^{2+} was generated and reacted with CO_3^{2-} to form $FeCO_{3,(s)}$ in the center. To model the diffusion process through a diffusion barrier such as a porous layer, a layer of loosely-packed sands surrounded by a bulk solution was employed instead of a single water droplet.

3.2 Simulated Geometries

A finite-element method (COMSOL Multiphysics) was used to solve the equations governing this system. The coordinates r, θ, and ϕ are shown in Figure 3-1. Under the assumption of axial symmetry, an one-quarter-ellipse geometry was used to represent a water droplet saturated with air and placed on the metal surface as shown in Figure 3-2A [24]. A geometry consisting of two concentric quarter-ellipses was used to represent the deposits surrounded by a bulk solution, as is shown in Figure 3-2B.

3.2.1 Droplet Model

As a first step toward development of a model for under-deposit corrosion inside pipelines, a model is being developed to simulate the Evan's drop. A schematic presentation of the droplet on a metal surface is shown in Figure 3-2A. Under the assumption of axially symmetry, a quarter-ellipse geometry could be used to reduce the number of nodes needed to represent the droplet. The local potential distribution can give rise to formation of distinct cathodic and anodic regions on the metal surface. The length of the diffusion path for oxygen or carbon dioxide from the air-water interface to

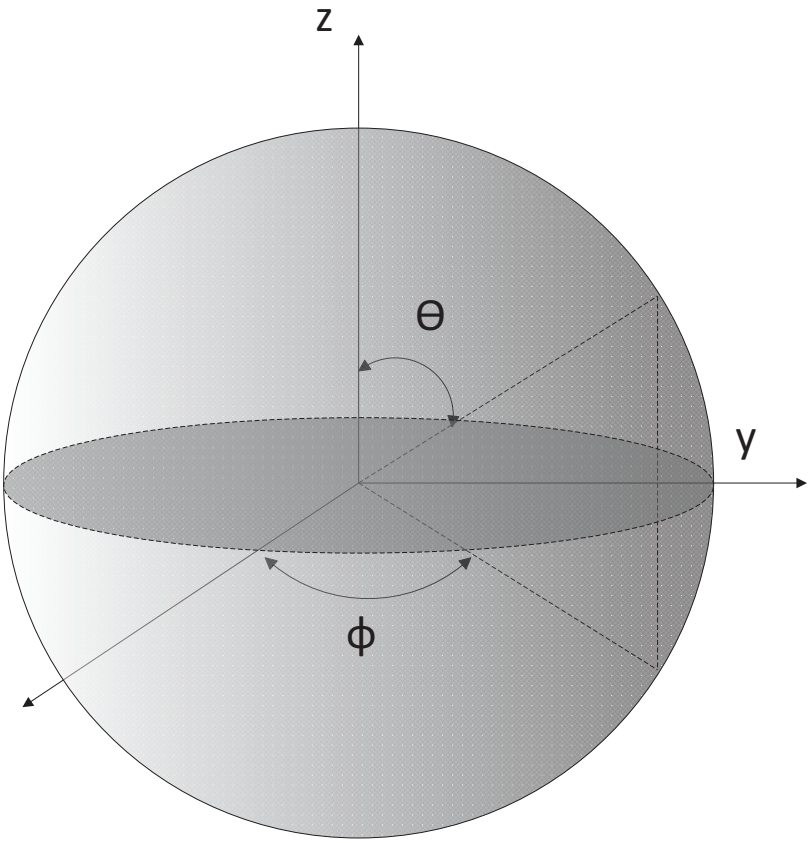

Figure 3-1. The coordinates r, θ, and ϕ used in the calculations.

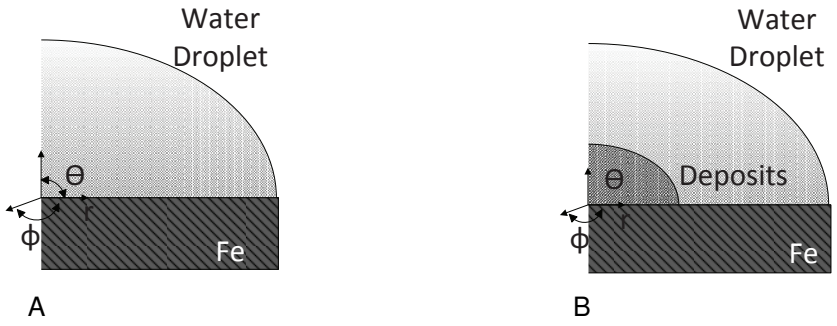

Figure 3-2. Schematic representations of: A) a water droplet on a metal surface; and B) deposits surrounded by bulk solutions.

metal surface varies along the radius of the metal covered by the droplet, thus creating a local potential distribution.

3.2.2 Deposit Model

The droplet model is extended. The scale is enlarged to simulate a defect resulted from the corrosive deposits and sands inside a pipeline. The geometry comprising two concentric quarter-ellipses was used to represent the deposits surrounded by a bulk solution, as shown in Figure 3-2B. The covered area is treated as a porous medium, and the effective diffusion coefficient of species $D_{i,covered}$ was expressed by the Bruggeman approximation [50, 59]

$$D_{i,covered} = \epsilon^{1.5} D_i \tag{3–1}$$

where ϵ is the porosity volume fraction. In the bulk region, the eddy diffusivity term $D_i^{(t)}$ was used to account for the influence of turbulence on mass transfer [47, 51].

$$D_{i,bulk} = D_i + D_i^{(t)} \tag{3–2}$$

The corresponding expressions for the eddy diffusivity are

$$\frac{D_i^{(t)}}{\nu} = \begin{cases} \dfrac{4A_1 z^{+3} - 5A_2 z^{+4}}{1 - 4A_1 z^{+3} + 5A_2 z^{+4}} & \text{for } z^+ \leq 20 \\ \dfrac{z^+}{2.5} - 1 & \text{for } z^+ > 20 \end{cases} \tag{3–3}$$

where ν is the kinematic viscosity and $z^+ = \sqrt{\tau_0 \rho}/\nu$ is the dimensionless distance from the metal surface. The wall shear stress τ_0 was assigned a value of 0.16 Pa in this work. It is below the critical value that the initiation of localized corrosion at carbon steel is independent of flow under CO_2 corrosion condition [60]. The dissolved gas was assumed to diffuse from the top of the droplet. The concentration distribution of the dissolved gas was dependent on the diffusivity differences between the deposit ($D_{i,covered}$) and the bulk region ($D_i^{(t)}$). The concentration gradient for reacting species (O_2) along the metal surface decreases due to the turbulent flow, as shown in Figure 3-3.

The blue curves represent the concentration distribution in laminar flow and the black

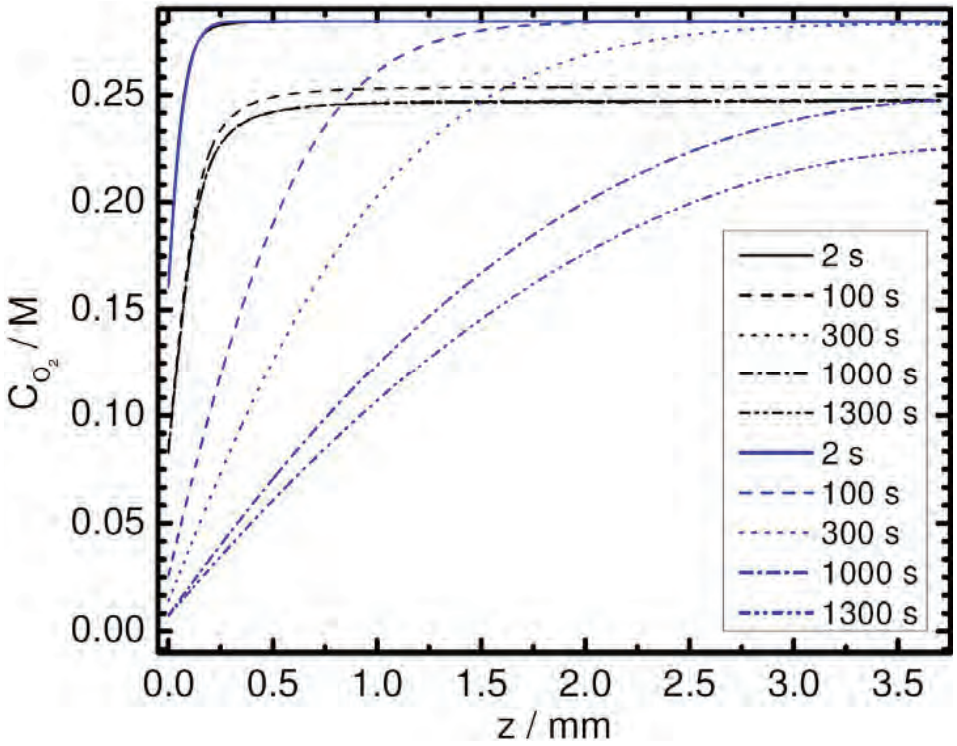

Figure 3-3. The concentration distribution of O_2 along the metal surface. The blue curves represent the conditions with laminar flow and the black ones represent the conditions with turbulent flow.

ones are for the turbulent conditions.

3.3 The Mathematical Model Development

Both Droplet and Deposit models were performed at applied potentials and corrosion potential (open-circuit condition). In the first, the corrosion reaction is represented by active-passive transition behaviors with applies potentials in polarization curves. After showing the polarization curves by applying an outer potential, the induced cathodic and anodic regions under the open-circuit condition are presented. The net current is zero by assuming the anodic and cathodic reactions reach equilibrium state which means the anodic and cathodic reaction rates are equal. The models calculated for the open-circuit potential were expended by adding time variable. The aerated solution was acted as the stepping stone for the under-deposit model and

the de-aerated solution can be calculated by replacing the reacting species and the homogeneous reactions. Both aerated and de-aerated solutions were calculated under two simulated geometries (Droplet and Deposit models). The model development can be classified into three categories: electrochemical reactions, conservation equations and chemical reactions, and active-passive transition in both aerated and de-aerated solutions.

3.3.1 Aerated Solution (O_2)

The dissolved gas varied for the aerated and de-aerated solutions, therefore, cathodic reactions were assumed differently for each solution. Only oxygen was involved in the cathodic reaction for the aerated solution. Water dissociation and formation of ferrous hydroxide were treated as homogeneous reactions in this model; whereas the formation of ferric hydroxide was assumed to have a contribution in anodic reactions.

3.3.1.1 Electrochemical Reactions

The cathodic reaction was assumed to be the reduction of oxygen

$$O_2 + 2H_2O + 4e^- \rightarrow 4OH^- \tag{3–4}$$

The corresponding current density can be expressed as

$$i_{O_2,k} = -i_{0,O_2}[c_{O_2}(0)] \exp\left[-\frac{2.303}{\beta_{O_2}}(\Phi_m - \Phi_0)\right] \tag{3–5}$$

where β_{O_2} is the Tafel slope for the oxygen reduction reaction. The current density i_{O_2} is a function of both the local potential driving force $(\Phi_m - \Phi_0)$ and the concentration of oxygen at the electrode surface $c_{O_2}(0)$. The equilibrium potential for oxygen reduction (U_{O_2}) was included in the value of the exchange current density.

Since iron is a major component in pipeline steel, the anodic reaction was assumed to be iron dissolution, given by [43, 44]

$$Fe \rightarrow Fe^{2+} + 2e^- \tag{3–6}$$

The anodic reaction showing the active to passive transition was assumed to be the consequence of the formation of corrosive products. In the absence of films associated with corrosion products, the kinetic current density $i_{k_{O_2},Fe}$ was given by

$$i_{k_{O_2},Fe} = (i_{0_{O_2},Fe}) \exp\left[\frac{2.303}{\beta_{Fe_{O_2}}}(\Phi_m - \Phi_0)\right] \tag{3–7}$$

where the equilibrium potential for iron dissolution (U_{Fe}) was included in the value of the exchange current density. Passivation was included in the kinetic expression by allowing the fractional surface coverage of corrosive products γ to weight the contributions of the passive and active current densities. Thus,

$$i_{Fe} = (1-\gamma)\, i_{k,Fe} + (\gamma) i_{p,Fe} \tag{3–8}$$

where $i_{p,Fe}$ is the value of the passive current density. The value of γ was determined from the reactions considered in Section 3.3.1.3.

3.3.1.2 Conservation Equations and Chemical Reactions

The model accounted for conservation of ionic species and dissolved oxygen, i.e.,

$$\frac{\partial c_i}{\partial t} = -\nabla \cdot \mathbf{N}_i + R_i \tag{3–9}$$

where R_i is the net rate of production of species i by homogeneous reactions. R_i can be expressed as

$$R_i = k_f \prod_r c_r(r, \theta, t) - k_b \prod_p c_p(r, \theta, t) \tag{3–10}$$

where k_f and k_b are the rate constants for forward and backward reactions, and c_r and c_p are the concentrations for reactants and products.

The homogeneous reactions considered in dissolved O_2 solutions included the dissociation of water

$$H_2O \quad \rightleftarrows \quad H^+ + OH^- \tag{3–11}$$

The rate of production was expressed by

$$R_{H^+} = R_{OH^-} = k_b(K_w - c_{H^+}c_{OH^-}) \tag{3–12}$$

where K_w is the dissociation constant for water. The formation of the ferrous hydroxide precipitates was assumed to follow

$$Fe^{2+} + 2OH^- \rightleftarrows Fe(OH)_{2(s)} \tag{3–13}$$

The reaction rate was expressed as

$$R_{Fe(OH)_2} = \begin{cases} 0 & \text{if } Fe(OH)_2 \leq 0 \\ \\ k_{Fe(OH)_2}[c_{Fe(OH)_2}(c_{OH})^2] - K_{sp,Fe(OH)_2} & \text{if } Fe(OH)_2 > 0 \end{cases} \tag{3–14}$$

where $K_{sp,Fe(OH)_2}$ is the solubility-product constant.

Under the assumption that convection can be neglected, the concentration of dissolved oxygen inside the deposit followed

$$\frac{\partial c_{O_2}}{\partial t} = \nabla^2 c_{O_2} \tag{3–15}$$

The flux of species i was expressed by

$$\mathbf{N}_i = -\frac{F}{RT} z_i D_i c_i \nabla\Phi - D_i \nabla c_i \tag{3–16}$$

The convection term was not employed in this work. Within the deposit, the velocity was assumed to be equal to zero; whereas, outside the deposit, diffusion was assumed to be enhanced by turbulent flow, as is described later. The potential distribution was assumed to be governed by

$$\nabla \cdot (\kappa \nabla\Phi) + F \sum_i z_i \nabla \cdot (D_i \nabla c_i) = 0 \tag{3–17}$$

Equation 3–17 reverts to Laplace's equation under assumption of a uniform conductivity and in the absence of concentration gradients.

3.3.1.3 Active-Passive Transition

Experimental polarization curves for materials showing active-passive transitions often show, in addition, the appearance of an apparent mass-transfer-limited current plateau. This plateau may be associated with deposition of films. The first step was applying an artificial ξ function to describe active-passive transitions. In a general case where an electrochemical reaction is limited by the finite rate of transport of reacting species to the reaction surface, the current may be formulated as

$$\frac{1}{i_{\mathrm{Fe}_\xi}} = \frac{1}{i_{\mathrm{k,Fe}}} + \frac{1}{i_{\mathrm{lim,Fe}}} \tag{3–18}$$

where i_{lim} is the mass-transfer-limited current density and the kinetic current density, i_{k}, is the kinetic current density as shown in Equation 3–7. Passivation was included in the kinetic expression by assigning a potential-dependent weighting factor to passive and active current densities. Thus,

$$i_{\mathrm{Fe}_\xi} = (1-\xi)\, i_{0,\mathrm{Fe}} \left[\frac{\exp\left(\frac{2.303}{\beta_{\mathrm{Fe}}}\left(\Phi_{\mathrm{m}} - \Phi_0 - U_{\mathrm{Fe}}\right)\right)}{1 + \frac{i_{0,\mathrm{Fe}}}{i_{\mathrm{lim,Fe}}} \exp\left(\frac{2.303}{\beta_{\mathrm{Fe}}}\left(\Phi_{\mathrm{m}} - \Phi_0 - U_{\mathrm{Fe}}\right)\right)} \right] + (\xi) i_{\mathrm{p}_{\mathrm{O}_2},\mathrm{Fe}} \tag{3–19}$$

where $i_{\mathrm{p}_{\mathrm{O}_2},\mathrm{Fe}}$ is the value of the passive current density, and

$$\xi = \frac{\exp\left(\lambda\left(\Phi_{\mathrm{m}} - \Phi_0 - E_{\mathrm{p}}\right)\right)}{1 + \exp\left(\lambda\left(\Phi_{\mathrm{m}} - \Phi_0 - E_{\mathrm{p}}\right)\right)} \tag{3–20}$$

is the potential-dependent weighting factor. In Equation 3–20, the parameter λ controls the steepness of the potential change corresponding to the active-passive transition and E_{p} is the potential at which the transition occurs. The relationship between current density and charged species is given by

$$\mathbf{i} = \mathrm{F} \sum_{\mathrm{i}} z_{\mathrm{i}} \mathbf{N}_{\mathrm{i}} \tag{3–21}$$

At the metal surface, the fluxes of Fe^{2+} and OH^- can be written as

$$\mathbf{N}_{\mathrm{Fe}^{2+}}|_{\theta=90^\circ} = \frac{i_{\mathrm{Fe}}(0)}{\mathrm{F}} \tag{3–22}$$

and

$$\mathbf{N}_{OH^-}|_{\theta=90^\circ} = -\frac{i_{O_2}(0)}{F} \tag{3–23}$$

The ξ function shows the mass-transfer-limited current plateau and the results are shown in Chapter 4. Therefore, a similar approach was employed to correlate the formation of precipitates and the transitions. The active-passivation transition was assumed to be resulted from the formation of precipitates in the following calculation. The surface coverage of precipitates (γ) is the ratio of the surface area of deposited precipitates to the surface area of metal surface and can be expressed as

$$\gamma_{Fe(OH)_2} = \frac{A_{Fe(OH)_2}}{A_{\text{metal surface}}} = \frac{c_{Fe(OH)_2} V_{\text{mesh}}/(\rho_{s,Fe(OH)_2}\delta)}{A_{\text{mesh}}} \tag{3–24}$$

where V_{mesh} and A_{mesh} are the volume and surface area, respectively, of the deformed mesh directly above the metal surface, $\rho_{s,Fe(OH)_2}$ is the density of precipitated $Fe(OH)_2$, and δ is the monolayer thickness. The surface coverage was employed to calculate the passive current density associated with the formation of $Fe(OH)_2$. For iron dissolution, the anodic current density was modified following

$$i_{Fe_{O_2}} = \begin{cases} (1-\gamma_{Fe(OH)_2}) i_{k_{O_2},Fe} + (\gamma_{Fe(OH)_2}) i_{p_{O_2},Fe} & \text{if } \gamma_{Fe(OH)_2} \leq 1 \\ \\ i_{p_{O_2},Fe} & \text{if } \gamma_{Fe(OH)_2} > 1 \end{cases} \tag{3–25}$$

where $i_{p_{O_2},Fe}$, the exchange current density for iron dissolution at the metal-precipitate interface, is extremely small as compared to $i_{0_{O2},Fe}$ for iron dissolution at the metal surface. The surface coverage (γ) acts as the same as the ξ function in Equation 3–19. A similar approach was employed for the oxygen reduction reaction with the exception that the reaction on the passive layer surface was less inhibited to account for the semiconductive nature of the precipitates. The oxygen reduction could still occur on the precipitates and the iron dissolution was assumed to be passivated. The cathodic

current density was expressed as

$$i_{O_2} = \begin{cases} -\left[(1-\gamma_{Fe(OH)_2})i_{O_2,k} + (\gamma_{Fe(OH)_2})i_{oxide,O_2}\right] & \text{if } \gamma_{Fe(OH)_2} \leq 1 \\ \\ -i_{oxide,O_2} & \text{if } \gamma_{Fe(OH)_2} > 1 \end{cases} \tag{3–26}$$

where $i_{oxide,O_2} = (i_{p0_{O_2},Fe}) \exp\left[\frac{2.303}{\beta_{Fe_{O_2}}}(\Phi_m - \Phi_0)\right]$, the passive current density for oxygen reduction at precipitate-solution interface.

The ferrous ions can further react with hydrogen ions and oxygen to produce ferric ions, and the ferric ions reacts with hydroxide ions to produce ferric oxide. The net reaction can be written as

$$Fe(OH)_2 + OH^- \rightleftarrows Fe(OH)_{3(s)} + e^- \tag{3–27}$$

The current density was expressed as

$$\frac{i_{Fe(OH)_3}}{F} = k_a(c_{OH^-})\exp\left[\frac{2.303}{\beta_{Fe^{3+}}}(\Phi_m - \Phi_0 - U_{Fe(OH)_3})\right] \tag{3–28}$$

The surface coverage resulted from the formation of $Fe(OH)_3$ can be calculated by using Equation 3–25. The influence of $Fe(OH)_3$ on the anodic reaction can be described as follows

$$i_{Fe_{O_2}} = \begin{cases} (1-\gamma_{Fe(OH)_3})i_{k_{O_2},Fe} + (\gamma_{Fe(OH)_3})i_{p_{O_2},Fe} & \text{if } \gamma_{Fe(OH)_3} \leq 1 \\ \\ i_{p_{O_2},Fe} & \text{if } \gamma_{Fe(OH)_3} > 1 \end{cases} \tag{3–29}$$

3.3.2 De-Aerated Solution (CO_2)

Two mechanisms were studied in the solutions containing dissolved CO_2: One was proposed by Remita, it was under the assumption that the first dissociation step of H_2CO_3 was fast enough to ignore the existence of H_2CO_3. Only hydrogen evolution contributed in the cathodic reaction [58]. Another mechanism was proposed by Nordsveen [47], the presence of H_2CO_3 and both hydrogen evolutions directly from

hydrogen ions and H_2CO_3 were all included. Water dissociation, hydration of carbon dioxide, two dissociation steps of carbonic acid, and formation of ferrous carbonate were treated as homogeneous reactions in this model.

3.3.2.1 Electrochemical Reactions

The main cathodic reactions were assumed to be the hydrogen evolution from H^+ only in the mechanism proposed by Remita [58].

$$2H^+ + 2e^- \rightarrow H_2 \tag{3–30}$$

The corresponding current density of individual cathodic reaction can be expressed as

$$i_{R,H_2} = -i_{R0,H_2}\left[c_{H^+}(0)\right]^{0.5} \exp\left[-\frac{2.303}{\beta_{H_2}}\left(\Phi_m - \Phi_0\right)\right] \tag{3–31}$$

where $\beta_{c_{H_2}}$ is the Tafel slope for the hydrogen evolution reaction from H^+. The current density i_{R,H_2} is a function of both the local potential driving force $(\Phi_m - \Phi_0)$ and the concentration of hydrogen ions at the electrode surface $c_{H^+}(0)$.

The main cathodic reactions were assumed to be the hydrogen evolution from H^+ and H_2CO_3 in the mechanism proposed by Nordsveen [47].

$$2H_2CO_3 + 2e^- \rightarrow H_2 + 2HCO_3^- \tag{3–32}$$

The corresponding current density of individual cathodic reaction can be expressed as

$$i_{N,H_2} = i_{N0,H_2}\left[\frac{c_{H^+}(0)}{c_{H^+,ref}}\right]^{0.5}\left[10^{\frac{\left(\Phi_m-\Phi_0-U_{H_2,ref}\right)}{b_{H_2}}} - 10^{\frac{-\left(\Phi_m-\Phi_0-U_{H_2,ref}\right)}{b_{H_2}}}\right] \tag{3–33}$$

where b_{H_2} is the coefficient for the hydrogen evolution reaction from H^+. The current density i_{N,H_2} is a function of both the local potential driving force $(\Phi_m - \Phi_0)$ and the concentration of hydrogen ions at the electrode surface $c_{H^+}(0)$.

$$i_{H_2CO_3} = i_{0,H_2CO3}\left[\frac{c_{H^+}(0)}{c_{H^+,ref}}\right]^{-0.5}\left[\frac{c_{H_2CO_3}(0)}{c_{H_2CO_3,ref}}\right]\left[10^{\frac{\left(\Phi_m-\Phi_0-U_{H_2CO_3,ref}\right)}{b_{H_2CO_3}}} - 10^{\frac{-\left(\Phi_m-\Phi_0-U_{H_2CO_3,ref}\right)}{b_{H_2CO_3}}}\right] \tag{3–34}$$

where b_{H_2CO3} is the Tafel slope for the hydrogen evolution reaction from H_2CO_3. The current density $i_{H_2CO_3}$ is a function of both the local potential driving force $(\Phi_m - \Phi_0)$ and the concentration of carbonic acid at the electrode surface $c_{H_2CO_3}(0)$.

In the dissolved CO_2 solution, iron dissolution was assumed to be the anodic reaction and can be expressed in Equation 3–6 [43, 44]. The anodic reaction showing the active to passive transition was assumed to be the consequence of the formation of $FeCO_3$. In the absence of films associated with corrosion products, the kinetic current density i_k was given by

$$i_{k_{CO_2},Fe} = i_{0_{CO_2},Fe}\left[10^{\frac{\left(\Phi_m-\Phi_0-E_{Fe^{2+},ref}\right)}{b_{Fe^{2+}}}} - 10^{\frac{-\left(\Phi_m-\Phi_0-E_{Fe^{2+},ref}\right)}{b_{Fe^{2+}}}}\right] \tag{3–35}$$

Passivation was considered in the kinetic expression by including the fractional surface coverage of corrosive products γ to weight the contributions of the passive and active current densities. Thus, Equation 3–8 can also be applied. The value of γ was determined from the formation of ferrous carbonate and will be shown in Section 3.3.2.3.

3.3.2.2 Conservation Equations and Chemical Reactions

The homogeneous reactions considered in the present model included the dissociation of water, as described in Equation 3–11 and Equation 3–12. For the mechanisms proposed by Remita, the homogeneous reactions involving CO_2, HCO_3^-, and CO_3^{2-} are as follows

$$CO_{2(g)} \rightleftarrows CO_2 \tag{3–36}$$

The concentration of dissolved carbon dioxide was expressed by

$$c_{CO_2(aq)bulk} = H_{CO_2} P_{CO_2} \tag{3–37}$$

where H_{CO_2} is the Henry's constant for CO_2 and P_{CO_2} is the partial pressure of CO_2 in the gas phase.

$$H_2O + CO_{2(aq)} \rightleftarrows HCO_3^- + H^+ \tag{3–38}$$

The rate of production was expressed by

$$R_{HCO_3^-} = -R_{CO_{2(aq)}} = k_1 c_{CO_{2(aq)}} - k_{-1} c_{H^+} c_{HCO_3^-} \tag{3–39}$$

where k_1 and k_{-1} are the kinetic constants.

$$HCO_3^- \rightleftarrows CO_3^{2-} + H^+ \tag{3–40}$$

The rate of production was expressed by

$$R_{CO_3^{2-}} = k_2 c_{HCO_3^-} - k_{-2} c_{H^+} c_{CO_3^{2-}} \tag{3–41}$$

where k_2 and k_{-2} are the kinetic constants. The rate of production for H^+ was expressed by

$$R_{H^+} = R_{HCO_3^-} + R_{CO_3^{2-}} \tag{3–42}$$

For the mechanisms for hydration carbon dioxide and the dissociation of H_2CO_3 in the aqueous solution, the mechanism is proposed by Nordsveen [47] assumed the dissociation is a two-step sequence as following

$$CO_{2(g)} \rightleftarrows CO_2 \tag{3–43}$$

The concentration of dissolved carbon dioxide was expressed by

$$c_{CO_2(aq)bulk} = K_{sol} P_{CO_2} \tag{3–44}$$

where K_{sol} is the kinetic constants for the dissolved rate.

$$H_2O + CO_{2(aq)} \rightleftarrows H_2CO_3 \tag{3–45}$$

$$H_2CO_3 \rightleftarrows H^+ + HCO_3^- \tag{3–46}$$

The rate of production was expressed by

$$R_{H_2CO_3} = -k_{f,ca}\, c_{H_2CO_3} + k_{b,ca}\, c_{H^+}\, c_{HCO_3^-} \tag{3–47}$$

where $k_{f,ca}$ and $k_{b,ca}$ are the rate constants.

$$HCO_3^- \rightleftarrows CO_3^{2-} + H^+ \tag{3–48}$$

All the species can be express by using a matrix form as follows [47]:

$$\begin{pmatrix} R_{H_2CO_3} \\ R_{H^+} \\ R_{HCO_3^-} \\ R_{CO_3^{2-}} \end{pmatrix} = \begin{pmatrix} -1 & 0 \\ 1 & 1 \\ 1 & -1 \\ 0 & 1 \end{pmatrix} \begin{pmatrix} k_{f,ca}\, c_{H_2CO_3} - k_{b,ca}\, c_{H^+}\, c_{HCO_3^-} \\ k_{f,bi}\, c_{HCO_3^-} - k_{b,bi}\, c_{H^+}\, c_{CO_3^{2-}} \end{pmatrix} \tag{3–49}$$

The two dissociation reactions are relatively slow compared with the hydration of CO_2 and therefore the equilibrium states could be assumed. H_2CO_3 was determined by the diffusion of CO_2 and hydration reaction while HCO_3^-, CO_3^{2-}, H^+, and OH^- are satisfied with the equilibrium states of water dissociation and dissociation of carbonic acid. The reacting species i (i=HCO_3^-, CO_3^{2-}, H^+, and OH^-) is governed by the diffusion equation with applied boundary conditions. In order to force the equilibrium conditions being satisfied, the feedback loop concept was applied to eliminate the discrepancy as follows.

$$Extra_{wa} = K_w - c_{OH^-}\, c_{H^+} \tag{3–50}$$

$$Extra_{ca} = K_{ca}\, c_{H_2CO_3} - c_{HCO_3^-}\, c_{H^+} \tag{3–51}$$

$$Extra_{bi} = K_{bi}\, c_{HCO_3^-} - c_{CO_3^{2-}}\, c_{H^+} \tag{3–52}$$

The new variables, $Extra_{wa}$, $Extra_{ca}$, and $Extra_{bi}$ were incorporated into diffusion equations as a reaction rate that consumes additional species and generates more for depletion. The mechanism of the iron carbonate precipitation was assumed to follow

$$\begin{aligned} &Fe_{(s)} + 2H_2CO_{3,(aq)} \rightleftharpoons Fe^{2+} + H_{2,(g)} + 2HCO^-_{3,(aq)} \quad \text{if } S \leq 1 \\ &Fe^{2+} + CO^{2-}_3 \rightleftharpoons FeCO_{3,(s)} \qquad\qquad\qquad\qquad\quad \text{if } S > 1 \end{aligned} \tag{3–53}$$

where $S = \frac{c_{Fe^{2+}} c_{CO^{2-}_3}}{K_{sp,FeCO_3}}$ The reaction rate was expressed as a function of S as following

$$R_{FeCO3} = \begin{cases} 0 & \text{if } S \leq 1 \\ \\ A_p \exp(\frac{-E_a}{RT})(\frac{A}{V})K_{sp,FeCO_3}(S-1) & \text{if } S > 1 \end{cases} \tag{3–54}$$

where A_p is a constant , E_a is the activation energy, R is universal gas constant, A is the metal surface area, V is the solution volume, and $K_{sp,FeCO_3}$ is the solubility-product constant.

Under the assumption that convection can be neglected, the concentration of dissolved carbon dioxide inside the deposit followed

$$\frac{\partial c_{CO_2}}{\partial t} = \nabla^2 c_{CO_2} \tag{3–55}$$

The flux of species i was expressed by Equation 3–16 The potential distribution was assumed to be governed by Equation 3–17.

3.3.2.3 Active-Passive Transition

At the metal surface, the flux of Fe^{2+} can be expressed by Equation 3–22; whereas the fluxes of H^+, H_2CO_3, and HCO^-_3 can be written as

$$\mathbf{N}_{H^+}|_{\theta=90^\circ} = -\frac{i_{H_2}(0)}{F} \tag{3–56}$$

$$\mathbf{N}_{H_2CO_3}|_{\theta=90^o} = -\frac{i_{H_2CO_3}(0)}{F} \tag{3–57}$$

and

$$\mathbf{N}_{HCO_3^-}|_{\theta=90^o} = \frac{i_{H_2CO_3}(0)}{F} \tag{3–58}$$

The surface coverage (γ) is the ratio of the surface area of deposited precipitates to the surface area of metal surface and can be expressed as

$$\gamma_{FeCO_3} = \frac{A_{FeCO_3}}{A_{\text{metal surface}}} = \frac{c_{FeCO_3} V_{\text{mesh}}/(\rho_{s,FeCO_3}\delta)}{A_{\text{mesh}}} \tag{3–59}$$

where $\rho_{s,FeCO_3}$ is the density of precipitate $FeCO_3$. The surface coverage was employed to calculate the passive current density due to the formation of $FeCO_3$. For iron dissolution, the anodic current density was using the same approach as described in Equation 3–25.

A similar approach was employed for the hydrogen reduction reactions with the exception that the reaction on the passive layer surface was less inhibited to account for the semiconductive nature of the precipitates. The cathodic current density was expressed as

$$i_c = i_{H_2} + i_{H_2CO_3} \tag{3–60}$$

$$i_{H_{2CO_2}} = \begin{cases} -\left[(1-\gamma_{FeCO_3})i_{H_2} + (\gamma_{FeCO_3})i_{p,H_2}\right] & \text{if } \gamma_{FeCO_3} \leq 1 \\ \\ i_{p,H_2} & \text{if } \gamma_{FeCO_3} > 1 \end{cases} \tag{3–61}$$

where

$$i_{p,H_2} = i_{p0,H_2}\left[\frac{c_{H^+}(0)}{c_{H^+,\text{ref}}}\right]^{0.5}\left[10^{\frac{\left(\Phi_m-\Phi_0-E_{H_2,\text{ref}}\right)}{b_{H_2}}} - 10^{\frac{-\left(\Phi_m-\Phi_0-E_{H_2,\text{ref}}\right)}{b_{H_2}}}\right] \tag{3–62}$$

the passive current density for hydrogen evolution from H^+ at precipitate-solution interface.

$$i_{H_2CO_{3CO_2}} = \begin{cases} -\left[(1-\gamma_{FeCO_3})i_{H_2CO_3} + \gamma_{FeCO_3} i_{p,H_2CO_3}\right] & \text{if } \gamma_{FeCO_3} \leq 1 \\ \\ i_{p,H_2CO_3} & \text{if } \gamma_{FeCO_3} > 1 \end{cases} \tag{3–63}$$

where

$$i_{p,H_2CO_3} = i_{p0,H_2CO_3} \left[\frac{c_{H^+}(0)}{c_{H^+,ref}}\right]^{-0.5} \left[\frac{c_{H_2CO_3}(0)}{c_{H_2CO_3,ref}}\right] \left[10^{\frac{\left(\Phi_m - \Phi_0 - E_{H_2CO_3,ref}\right)}{b_{H_2CO_3}}} - 10^{\frac{-\left(\Phi_m - \Phi_0 - E_{H_2CO_3,ref}\right)}{b_{H_2CO_3}}}\right] \tag{3–64}$$

the passive current density for hydrogen evolution from H_2CO_3 at precipitate-solution interface.

CHAPTER 4
RESULTS AND DISCUSSIONS

The results for systems containing O_2 and CO_2 are sequentially presented in the following.

4.1 Aerated Model-O_2

The corrosion rate is strongly dependent on the presence and properties of surface films and associated chemical and electrochemical reactions. In the present work, iron was used as the reacting species as it is the principle material used in gas and oil pipelines. Iron, chromium, nickel, titanium and their alloys also demonstrate active-passive transitions, which in this paper was assumed to be the consequence of the presence of the corrosive products.

Under certain conditions, the surface under the drop can experience both active and passive behavior. To explore simultaneous active and passive behavior, parameters were chosen to allow the open-circuit potential distribution on the metal surface to encompass the region between passive and active behavior. The open-circuit potential is the potential at which there is no current and the equilibrium potential of a corroding system. The parameters used in the calculations are presented in Table 4-1, 4-2, and 4-3. For the one-quarter-ellipse geometry (see O_2 Evans' Drop in Table 4-2), the shift of passivated area can be illustrated by changes of the total current density. The local pH differences can only be observed when $Fe(OH)_2$ reacts further with OH^- to form $Fe(OH)_3$. The two-concentric-quarter-ellipse geometry (see O_2 Deposit in Table 4-3) was used to evaluate under-deposit corrosion and the influences of both the formation of precipitates and the surrounding turbulent flow [28, 29]. The results are presented in terms of two sets of calculations. The parameters marked Less Active in Table 4-3 lead to a corrosion product that still allows iron dissolution and oxygen reduction react; whereas, the parameters marked Passive in Table 4-3 lead to a corrosion product that strongly inhibits anodic reaction. The results were used to study the influence of the

protectiveness and properties of precipitates. Other influential factors, such as mesh size, drop eccentricity, drop size...etc will be discussed in Section 4.1.3.

Table 4-1. Parameters for the simulations involving anodic reactions that are active-passive controlled with ξ function.

	Active-Passive (ξ function)	
i_{0,O_2}	1.00×10^{-3}	A/cm^2
D_{O_2}	1.97×10^{-5}	cm^2/s
κ	5.50×10^{-4}	S/m
$c_{O_2}(r_0)$	0.284	mol/m^3
U_{O_2}	0.401	V
β_{O_2}	0.09	V/decade
$i_{0,Fe}$	1.00×10^{-3}	A/cm^2
β_{Fe}	0.01	V/decade
U_{Fe}	-0.44	V
E_p	0.1	V
$i_{p,Fe}$	5.00×10^{-5}	A/cm^2
i_{lim}	7.00×10^{-1}	A/cm^2
λ	550	

4.1.1 Active-Passive Transition

Calculated local anodic and cathodic current densities for the active-passive controlled involving ξ function are shown in Figure 4-1. Figure 4-2A shows the concentration distribution of oxygen along the metal surface with applied potential as the parameter. The potential distribution at the maximum concentration gradient was plotted in Figure 4-2B and the cathodic reaction is dominated at the periphery while the anodic reaction is preferred at the center. For the models assuming the passivation resulted from the formation of precipitate, the mass-transfer-limited plateau is also shown in Figure 4-3 as functions of electrode potential for the deposit model at a position $r = 0$. The anodic reaction shows an active-passive transition in which the active corrosion is replaced by passive behavior as the electrode potential increases. The resulting surface-averaged current is presented in Figure 4-4 as individual points corresponding to each applied potential. The role of film formation in passivation is evident in Figure 4-5 in which distributions of current density (Figure 4-5A) and surface coverage (Figure

Table 4-2. Parameters for the O_2 simulations in one-quarter ellipse geometry involving surface coverage.

	O_2 Evans' Drop (one-quarter ellipse as shown in Figure 3-2A)	
i_{0,O_2}	7.0×10^{-7}	A/cm^2
D_{O_2}	1.97×10^{-5}	cm^2/s
$c_{O_2}(\infty)$	0.284	mol/m^3
β_{O_2}	0.12	V/decade
i_{oxide,O_2}	7.0×10^{-7}	A/cm^2
$i_{0,Fe}$	1.00×10^{-8}	A/cm^2
$D_{Fe^{2+}}$	7.20×10^{-6}	cm^2/s
β_{Fe}	0.06	V/decade
$i_{p,Fe}$	1.00×10^{-12}	A/cm^2
κ	4.42×10^{-4}	S/m
D_{H^+}	9.31×10^{-5}	cm^2/s
D_{OH^-}	5.26×10^{-5}	cm^2/s
$D_{NO_3^-}$	1.90×10^{-5}	cm^2/s
D_{K^+}	1.98×10^{-5}	cm^2/s
k_{b,H_2O}	500	
K_w	1.00×10^{-8}	mol^2/m^6
$K_{sp,Fe(OH)_2}$	4.87×10^{-6}	
ϵ	$0.2^{(1.5)}$	
V_{mesh}	7.20×10^{-6}	cm^3/s
ρ	3.4	g/cm^3
δ	7.0×10^{-9}	m
A_{mesh}	7.20×10^{-6}	cm^2/s
$K_{sp,Fe(OH)_3}$	6.3×10^{-38}	

4-5B) are presented at different times for the Evans' drop model. At short times, due to the greater accessibility of oxygen at the water-air interface, the cathodic reaction dominated at the periphery of the droplet. Concentration of O_2 at t$= 10$ s was plotted in Figure 4-6, which shows O_2 is abundant in the periphery region and deficient at the center.

Ferrous ions are produced by the anodic reaction and react with hydroxide ions produced by the cathodic reaction to form ferrous hydroxides. $Fe(OH)_2$ further reacts with the excess OH^- to form ferric hydroxides, which is a an insoluble iron hydroxide complex and could slowly dehydrate to form rust. The Pourbaix diagram presented in Figure 4-7 shows that $Fe(OH)_3$ is the major precipitate under the given conditions. The

Table 4-3. Parameters for the O_2 simulations in two-quarter ellipse geometry involving surface coverage..

	O_2 Deposit (two-quarter ellipse Figure 3-2B)			
	Less Active		Passive	
i_{0,O_2}	1.0×10^{-4}	A/cm^2	3.38×10^{-8}	A/cm^2
D_{O_2}	1.97×10^{-5}	cm^2/s	1.97×10^{-5}	cm^2/s
$c_{O_2}(\infty)$	0.284	mol/m^3	0.284	mol/m^3
β_{O_2}	0.2	V/decade	0.2	V/decade
i_{oxide,O_2}	7.0×10^{-5}	A/cm^2	2.63×10^{-10}	A/cm^2
$i_{0,Fe}$	5.0×10^{-10}	A/cm^2	1.0×10^{-9}	A/cm^2
$D_{Fe^{2+}}$	7.20×10^{-6}	cm^2/s	7.20×10^{-6}	cm^2/s
β_{Fe}	0.5	V/decade	0.5	V/decade
$i_{p,Fe}$	4.96×10^{-11}	A/cm^2	2.54×10^{-15}	A/cm^2
κ	4.42×10^{-4}	S/m	4.42×10^{-4}	S/m
D_{H^+}	9.31×10^{-5}	cm^2/s	9.31×10^{-5}	cm^2/s
D_{OH^-}	5.26×10^{-5}	cm^2/s	5.26×10^{-5}	cm^2/s
$D_{NO_3^-}$	1.90×10^{-5}	cm^2/s	1.90×10^{-5}	cm^2/s
D_{K^+}	1.98×10^{-5}	cm^2/s	1.98×10^{-5}	cm^2/s
k_{b,H_2O}	500		500	
K_w	1.00×10^{-8}	mol^2/m^6	1.00×10^{-8}	mol^2/m^6
$K_{sp,Fe(OH)_2}$	4.87×10^{-6}		4.87×10^{-6}	
ϵ	$0.2^{(1.5)}$		$0.2^{(1.5)}$	
V_{mesh}	7.20×10^{-6}	cm^3/s	7.20×10^{-6}	cm^3/s
ρ	3.4	g/cm^3	3.4	g/cm^3
δ	7.0×10^{-9}	m	7.0×10^{-9}	m
A_{mesh}	7.20×10^{-6}	cm^2/s	7.20×10^{-6}	cm^2/s
$K_{sp,Fe(OH)_3}$	6.3×10^{-38}		6.3×10^{-38}	
ν	1.05×10^{-6}	m^2/s	1.05×10^{-6}	m^2/s
A_1	1.0972×10^{-4}		1.0972×10^{-4}	
A_2	3.295×10^{-6}		3.295×10^{-6}	

alkali region prevails at the edge area as the results of cathodic reaction predominating at periphery when the center shows acidity as the consequence of the formation of precipitates, as shown in Figure 4-8. The formation of $Fe(OH)_3$ can be indicated by the surface coverage which is shown in Figure 4-5B. As time increases, the surface coverage exceeded the full coverage value, i.e., $\gamma = 1$, starting from the periphery and extending to the center until the surface was all covered with precipitates. The anodic reaction was inhibited by the formation of $Fe(OH)_3$, but the cathodic reaction was still

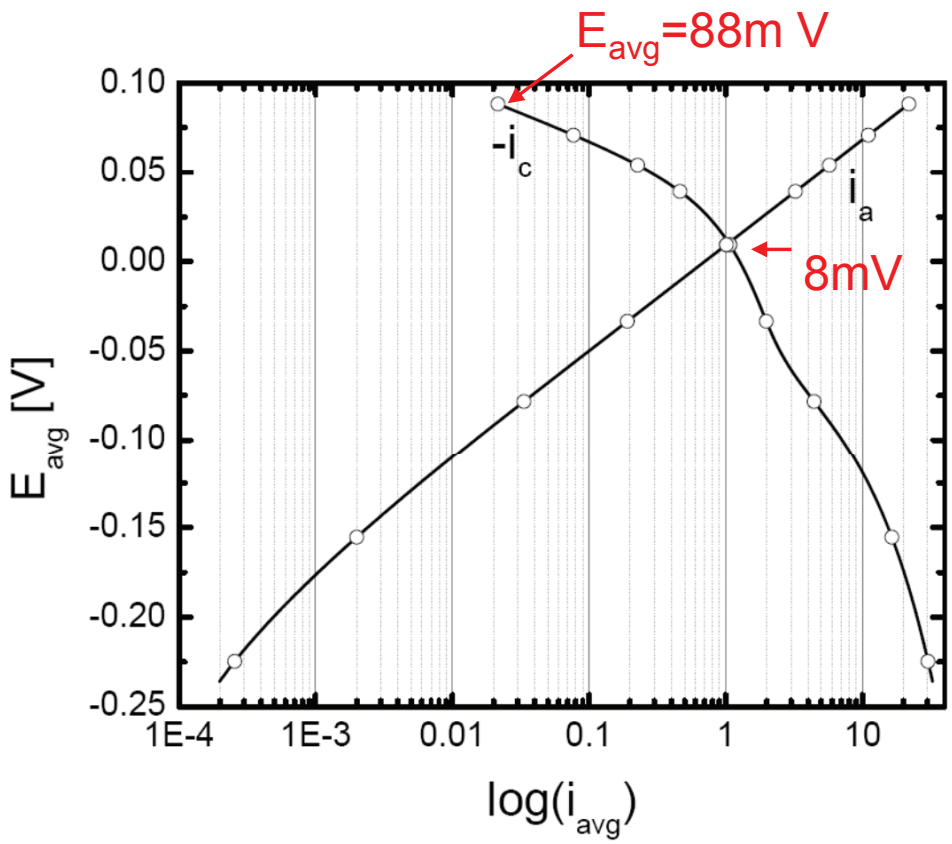

Figure 4-1. Calculated polarization curves showing anodic and cathodic current densities for the model simulating the active-passive transition with ξ function.

active. The active-passive transition was, therefore, a consequence of the formation of precipitates.

4.1.2 The Effect of Precipitation

All types of precipitates formed under the conditions that iron immersed in dissolved O_2 solutions are shown in Figure 4-7. The active-passive transitions was assumed to be a consequence of the formation of $Fe(OH)_2$ and $Fe(OH)_3$. $Fe(OH)_2$ was assumed to be formed as colloidal gel on the metal surface and further reacts with OH^- to form solid $Fe(OH)_3$ depositing on the surface. Therefore, the formation of ferrous hydroxide results in less-protective precipitates and the anodic reaction was partially inhibited by it. In Section 4.1.2.2, $Fe(OH)_3$ passivates the reacting surface as it deposits on the metal surface.

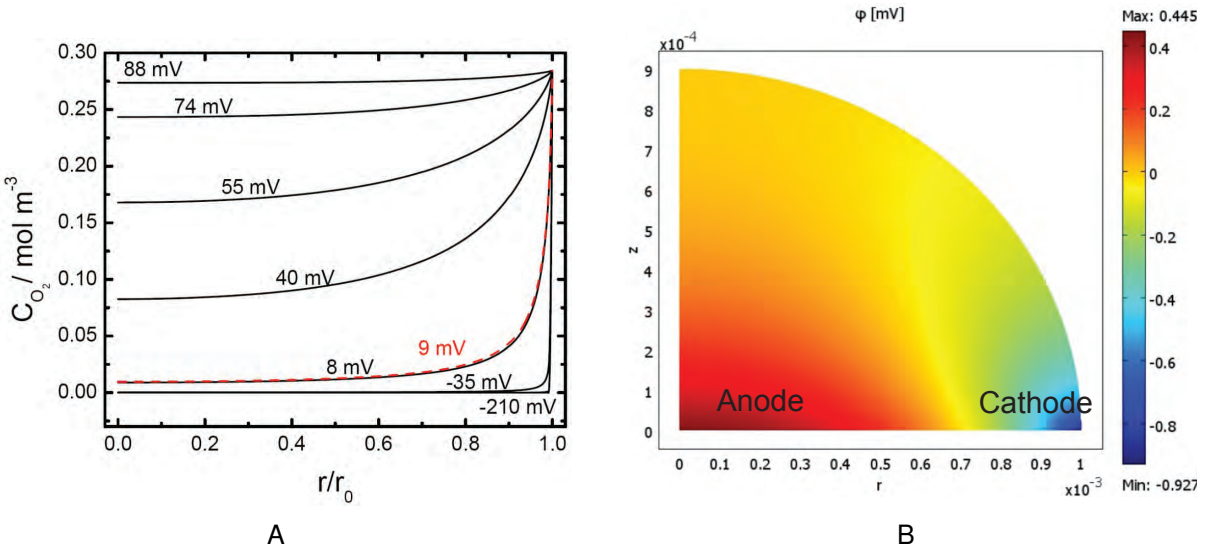

Figure 4-2. Results calculated for the model simulating the active-passive transition with ξ function: A) radial distributions of O_2 along the metal surface with applied potential as the parameter; and B) false color representation of potential for the maximum concentration gradient of O_2.

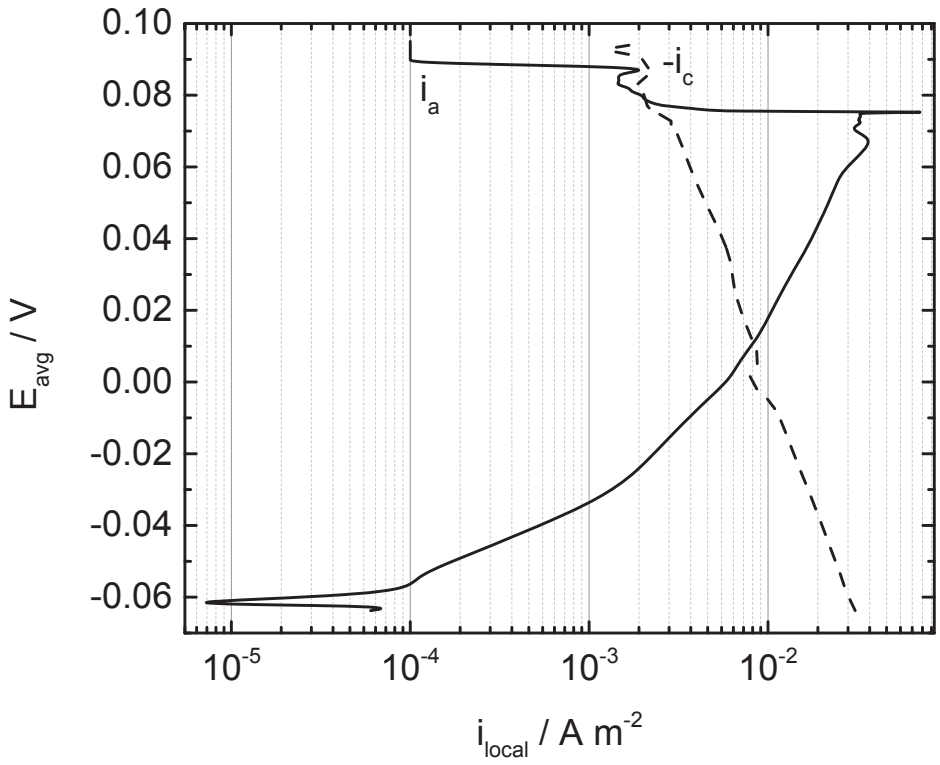

Figure 4-3. Calculated polarization curves showing anodic and cathodic current densities at $r = 0$ for the deposit model.

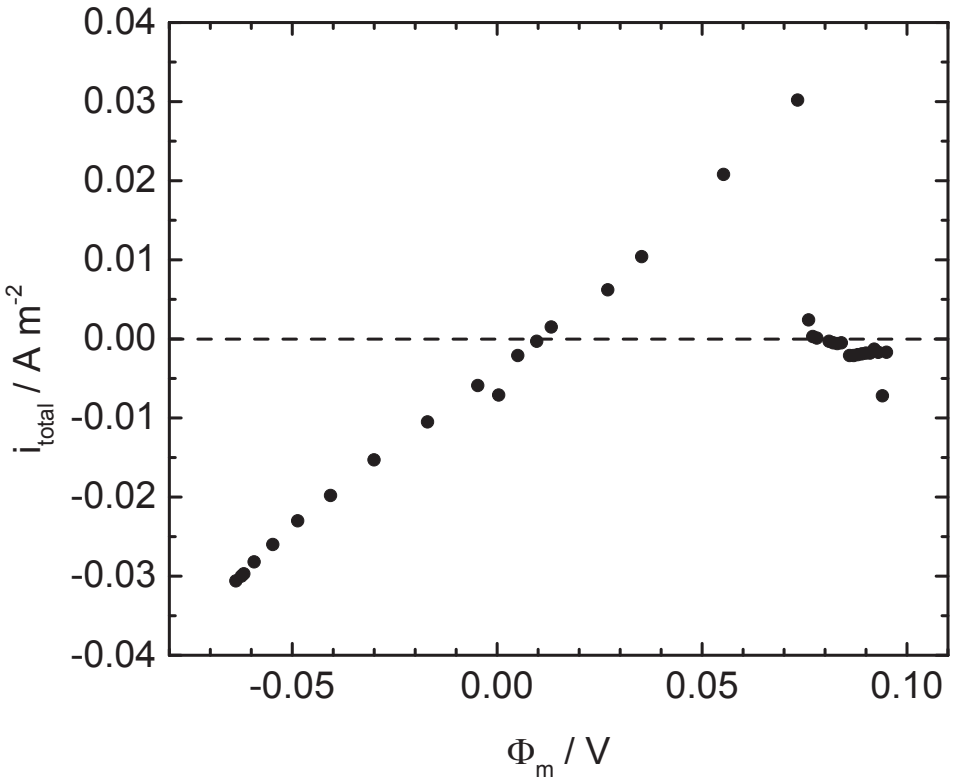

Figure 4-4. Surface-averaged current density calculated for the deposit model at $r = 0$ as a function of applied potential.

4.1.2.1 Less-Protective Precipitates ($Fe(OH)_2$)

In this calculation, the passivation was assumed to result from the less-protective precipitates, $Fe(OH)_2$. $Fe(OH)_3$ accumulates on top of $Fe(OH)_2$ and, therefore, does not play a part in passivation.

The influence of turbulent flow can be observed in Figure 4-9A. At $t = 92$ s, the concentration of oxygen at the electrode surface approached zero. At times $t > 92$ s, the transport of oxygen to the reacting surface in the region with turbulent flow was greater than in the covered region. As a consequence, the cathodic reaction was favorable in the surrounding area, while the anodic reaction dominated in the center. The shift from active to passive behavior was observed as the result of the development of precipitates which is shown in Figure 4-9B. Figure 4-10B represents the total current density distribution after whole metal surface is covered with precipitates.

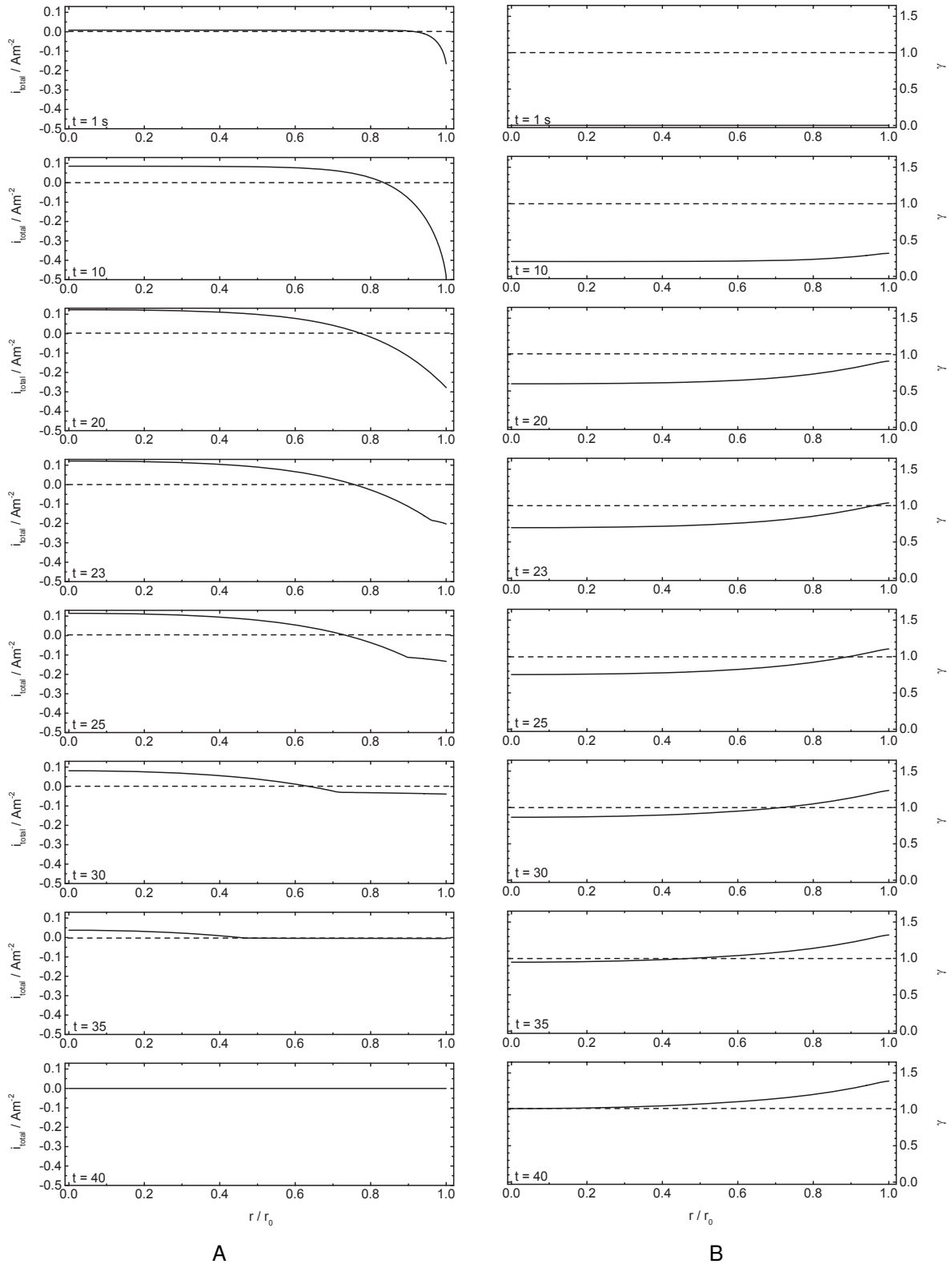

Figure 4-5. Radial distributions calculated for the Evans' drop model with time as a parameter: A) total current density; and B) fractional surface coverage.

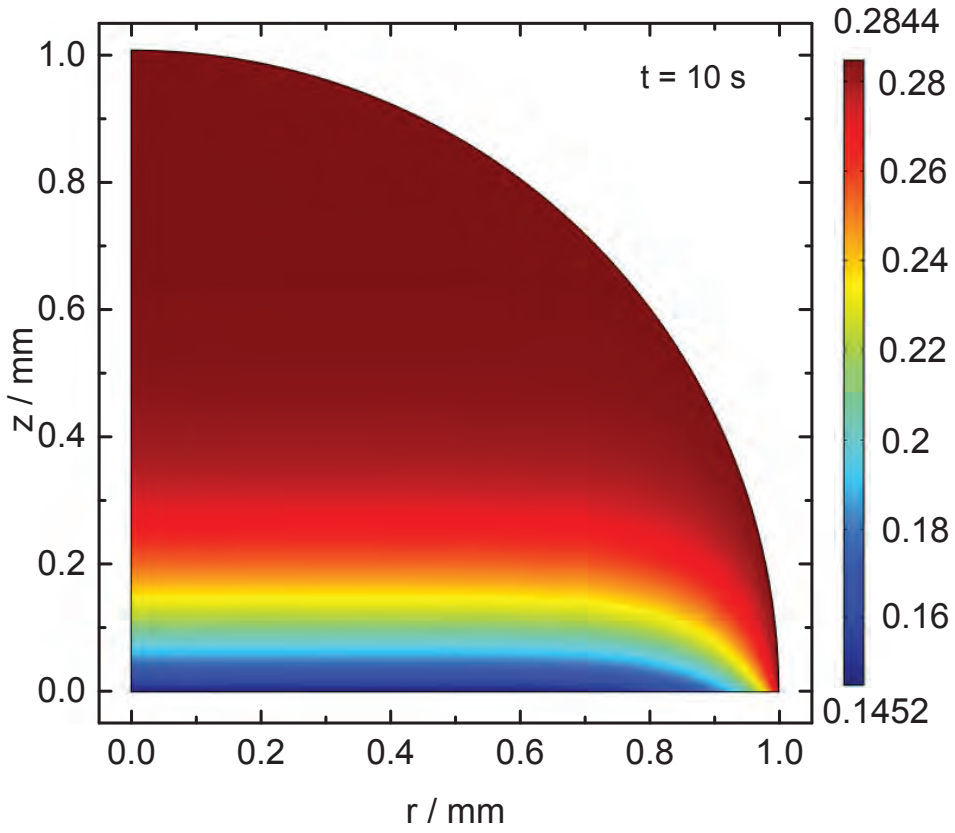

Figure 4-6. The false color representation of concentration distributions of oxygen for the droplet model containing O_2 at t= 10 s.

The corresponding changes of potential distribution are presented in Figure 4-11. The maximum potential difference of 0.1 V was obtained when the outer region was completely covered with precipitates ($t = 96$ s). The precipitates continued to accumulate on the metal surface, and the corrosion remained active under the predefined covered region as a result of the differential oxygenation cell driven by the surrounding turbulent flow.

The stability of films in the exposure of iron to aerated water at room temperature may be influenced by the solubility of ferrous hydroxide. As the film grew and reduced the rate of corrosion, the exchange of fluid with the bulk solution caused the concentrations of Fe^{2+} and OH^- to fall below the super-saturated value, thus favoring dissolution of the film. The dissolution rate of $Fe(OH)_2$ was assumed to be dependant on the solution

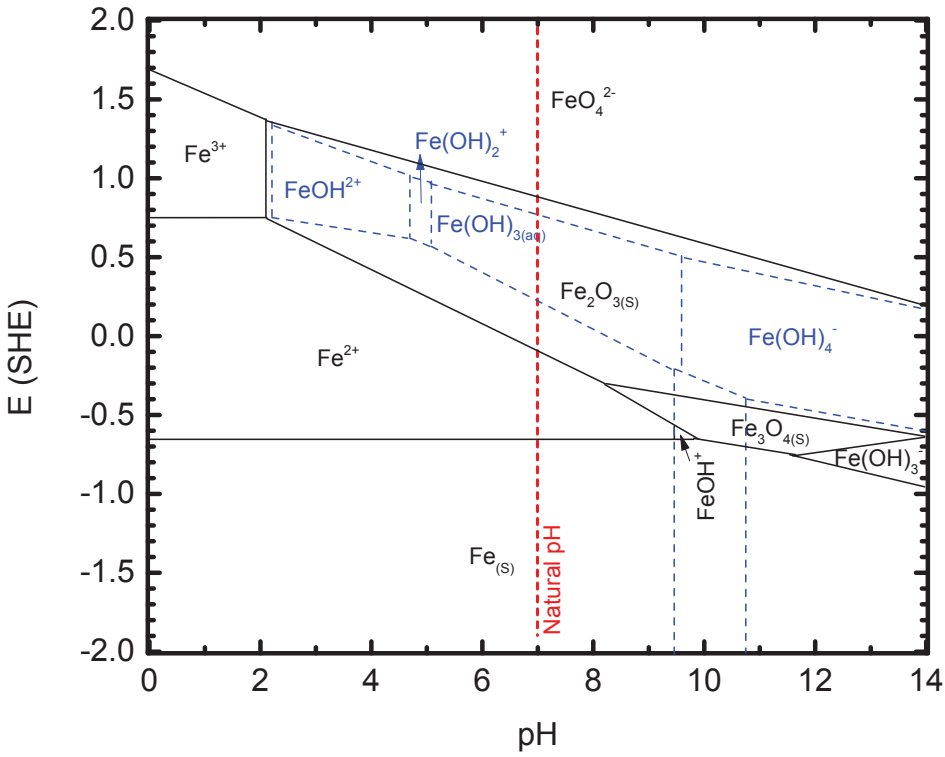

Figure 4-7. A Pourbaix diagram for iron and its various species at 25°C. The diagrams were generated by CorrosionAnalyzer 1.3 Revision 1.3.33 by OLI Systems Inc.

composition, temperature, and pressure. Two different values of solubility product were used in this paper. Whitman [61] calculated the solubility product of $Fe(OH)_2$ to be 8.7×10^{-14} in the ferrous-ion concentration in 20% potassium hydroxide solution. A value of $Fe(OH)_2 = 8.0 \times 10^{-16}$ was obtained by Leussing [62] at a temperature of $25°C$. The impact of the solubility product value can be shown in Figure 4-12 in which fractional surface coverage calculated for the deposit model is presented as a function of radial position with time as a parameter. The film dissolved for the solubility product of 8.7×10^{-14}, but remained intact for $K_{sp} = 8.0 \times 10^{-16}$. Careful examination of Figure 4-12B shows a slight thinning at $r = 1$ mm. For this condition, the anodic reaction occurred near the intersection of predefined porous medium and bulk solution. The potential and current distributions are plotted in Figure 4-13A and 4-13B.

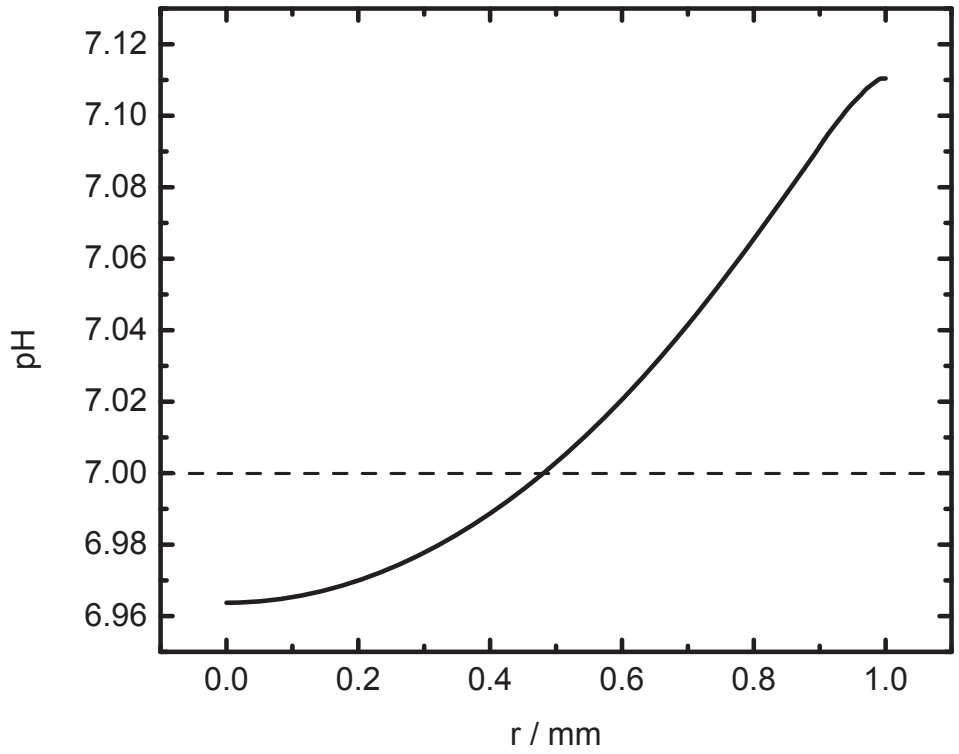

Figure 4-8. Radial distributions of pH calculated for the Evans' drop model.

4.1.2.2 Protective Precipitates ($Fe(OH)_3$)

Ferrous hydroxides can react further with the excess OH^-, producing the secondary precipitates, ferric hydroxides. Ferrous hydroxide was assumed to be in the form of a colloidal gel that did not passivate the metal surface. Only ferric hydroxides was assumed to completely shield the active metal surface. The cathodic reaction was preferred in the surrounding area, while the anodic reaction was favored in the center, as shown in Figure 4-14. As a consequence of protective precipitates, the corrosion rate decreased after the metal surface was fully-covered.

However, for the protective case, the influence of solubility product value is not significant. When the secondary precipitates ($Fe(OH)_3$) is the source of passivation, the change of solubility product only affected the time frame for building up deposits, as shown in Figure 4-15. The precipitates accumulate faster when the solubility product is smaller as shown in Figure 4-15B.

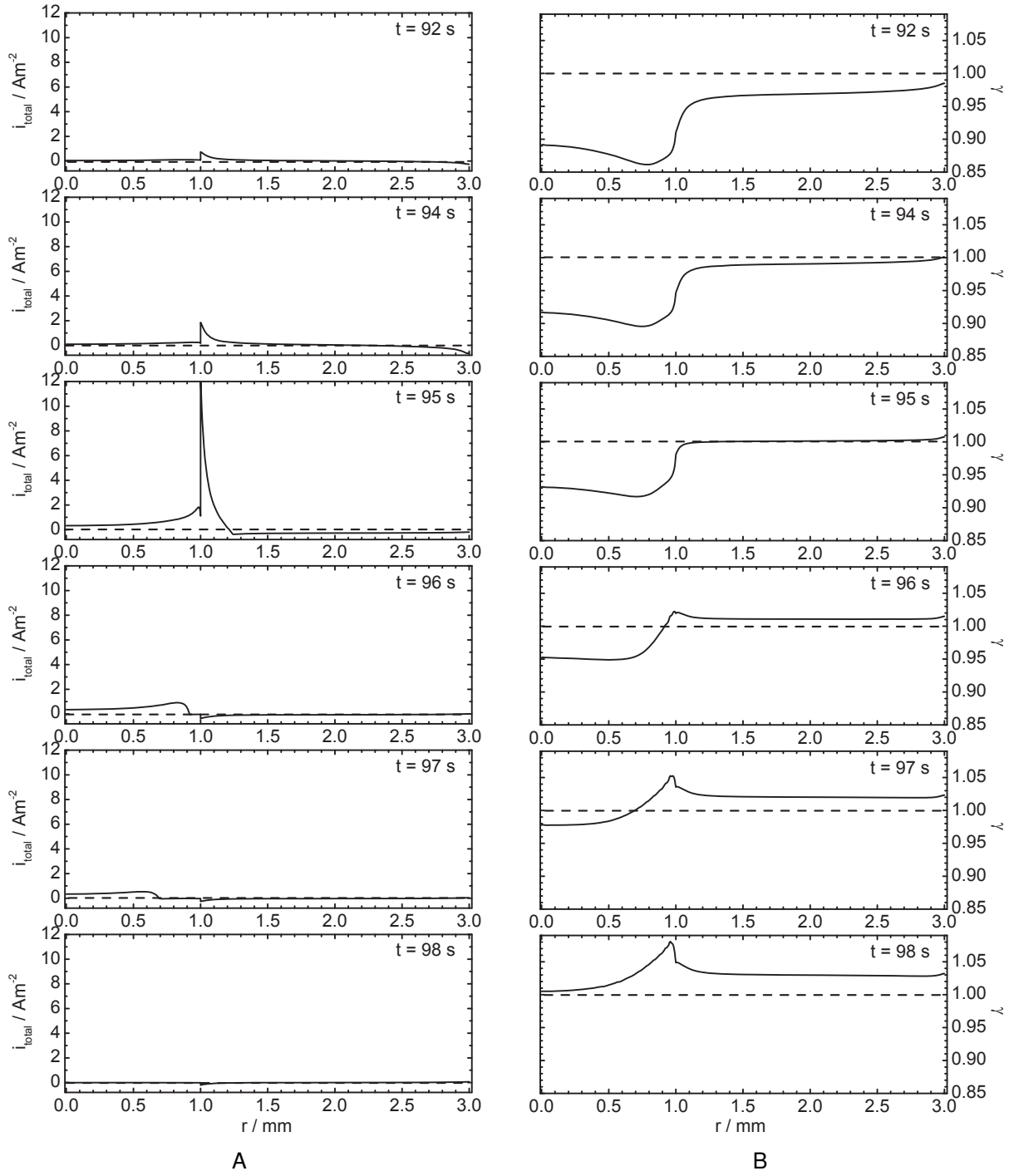

Figure 4-9. Radial distributions of calculated for the deposit model with time as a parameter: A) total current density and B) fractional surface coverage.

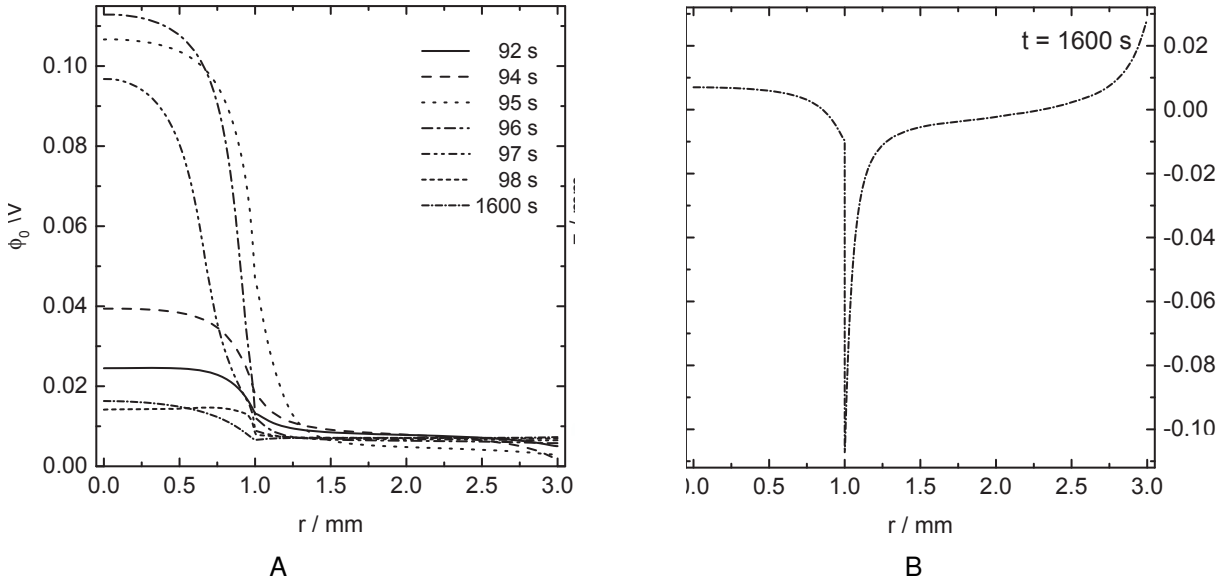

Figure 4-10. Representations of: A) potential distribution along the electrode surface with time as a parameter; B) total current density distribution along the electrode surface at $t = 1600$ s calculated for the deposit model.

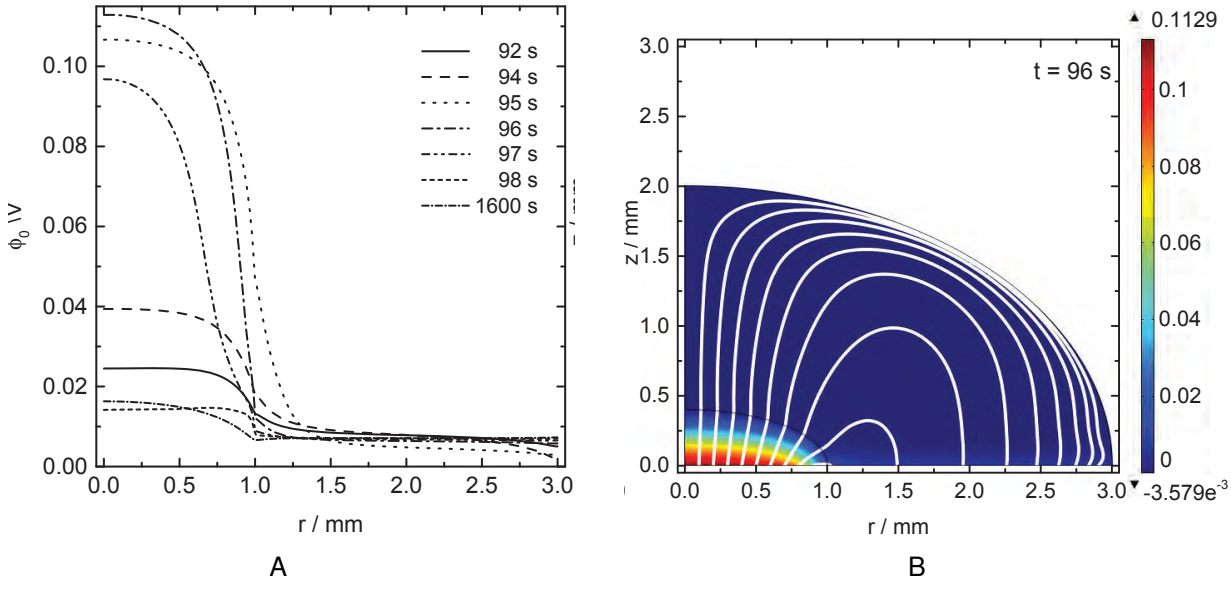

Figure 4-11. Potential distributions for the results presented in Figure 4-9: A) potential along the electrode surface with time as a parameter; B) false color representation of potential for $t = 96$ s with superimposed current lines.

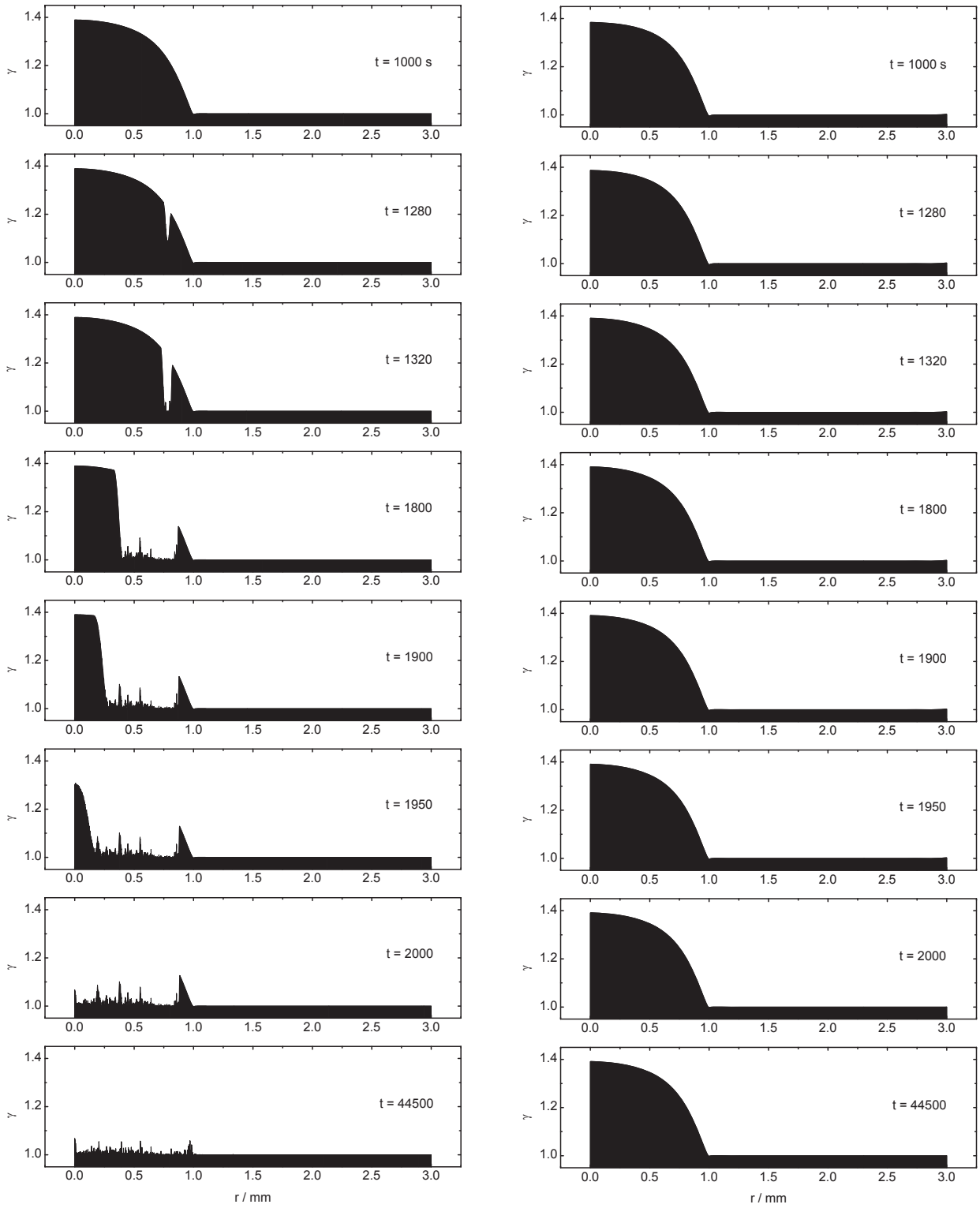

Figure 4-12. Radial distributions of fractional surface coverage calculated for the deposit model with time as a parameter: A) $K_{sp,Fe(OH)_2} = 8.7 \times 10^{-14}$; and B) $K_{sp,Fe(OH)_2} = 8.0 \times 10^{-16}$.

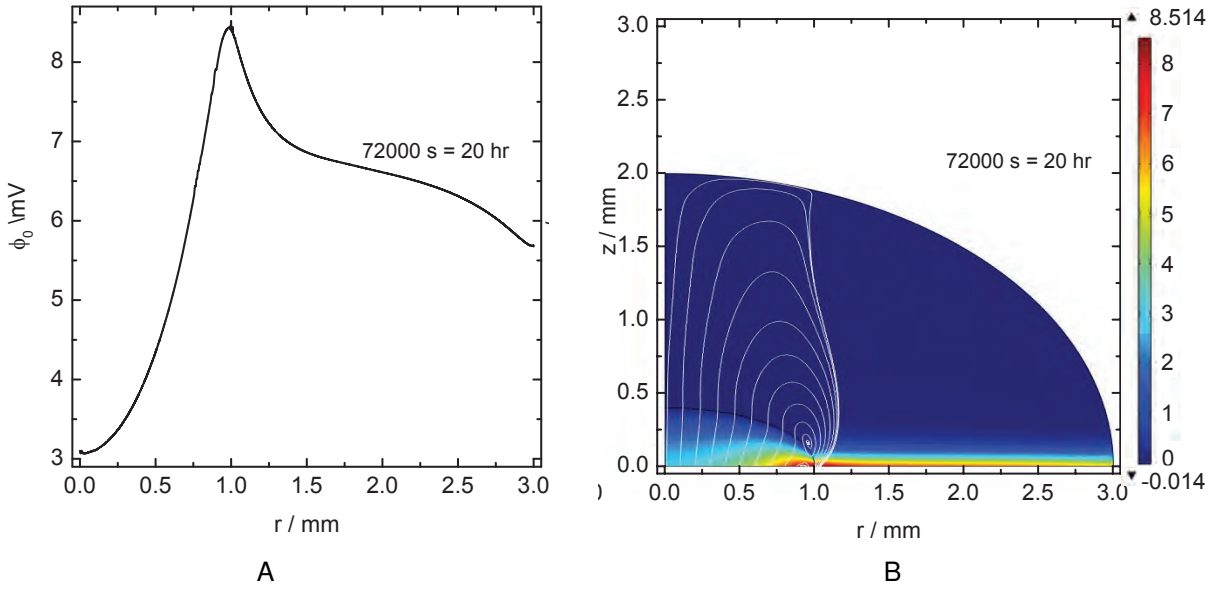

Figure 4-13. Potential distributions: A) along the electrode surface at $t = 72000$ s B) for the false color representation and streamline representation of current density at $t = 72000$ s calculated for the deposit model.

4.1.3 Other Influences

The concentration gradient of dissolved gas is the driving force of the galvanic coupling reactions. The concentration distribution of O_2 in the solution is relevant with the distance between the water-air interface and the metal surface. The size and the shape of the droplet were discussed in the first approach, which is the model applying ξ function to simulate the active-passive transitions. The mesh quality is also discussed since finer mesh results in more accurate solutions and requires more time and costs. As the development of model progresses, the area ratio of covered region and the bare metal surface for the Deposit model also plays an important role and the results will be shown.

4.1.3.1 Comparison between Analytic Solutions and Numerical Solutions

The performance of the numerically computational method is evaluated by using a benchmark. In this case, calculations of a temperature profile for unsteady-state heat conduction was used.

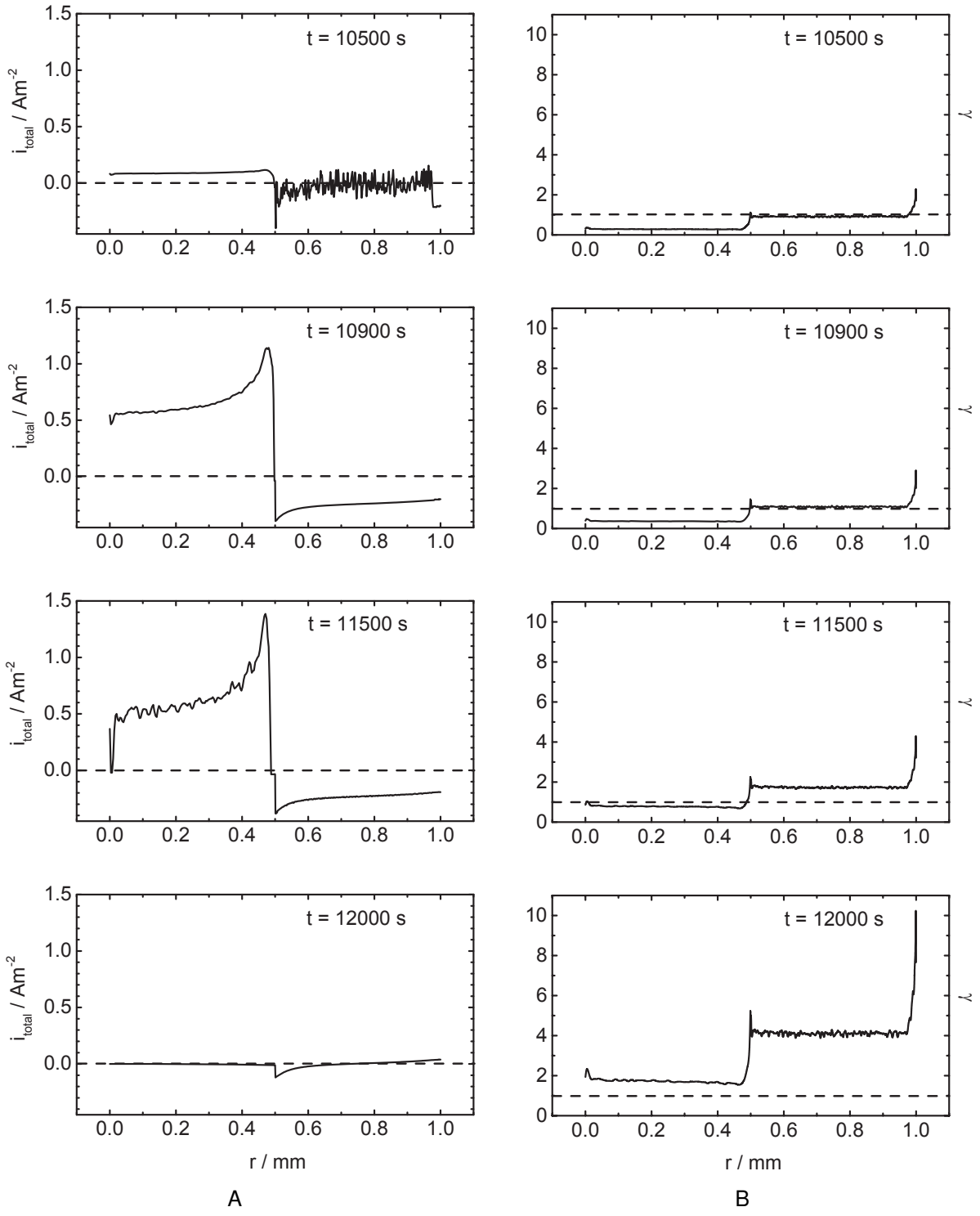

Figure 4-14. Radial distributions of calculated for the deposit model with time as a parameter: A) total current density and B) fractional surface coverage.

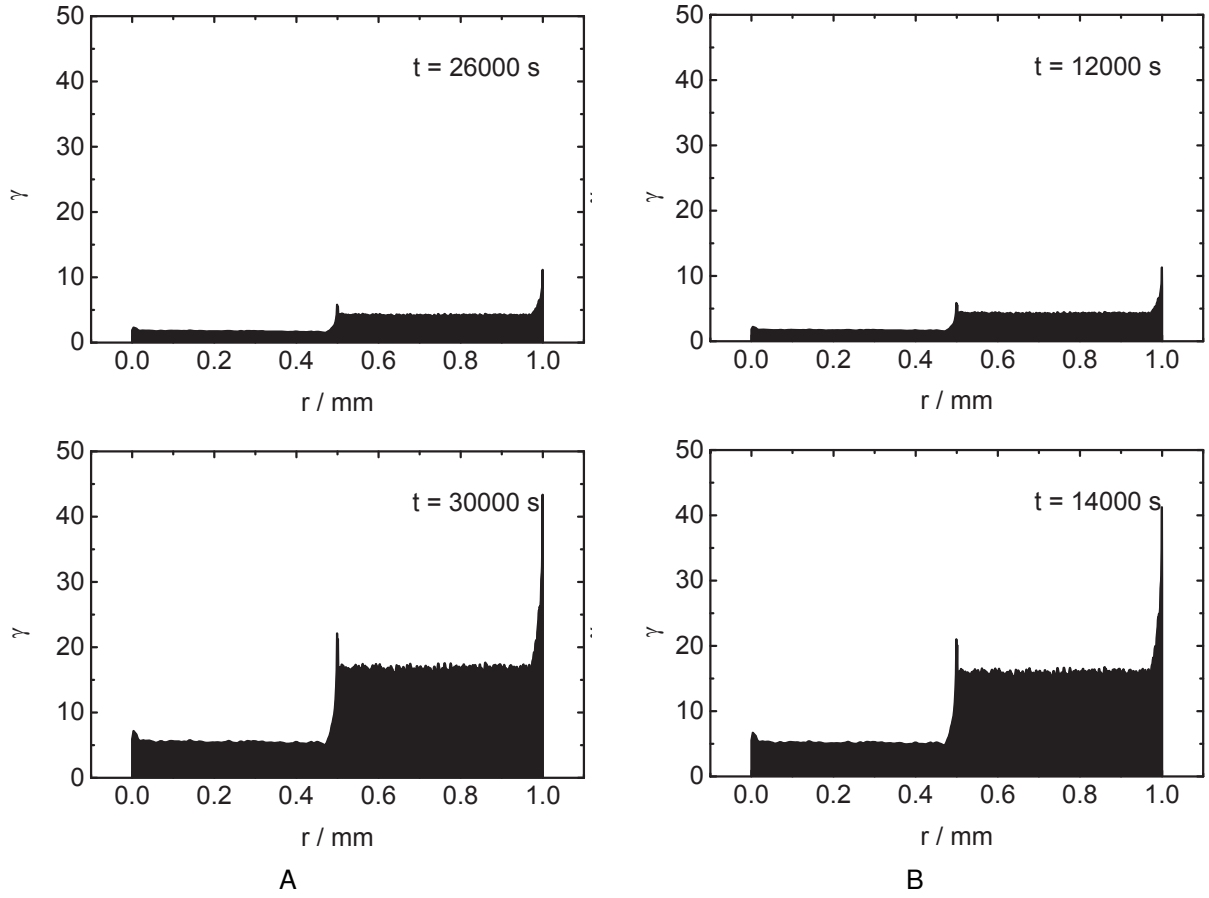

Figure 4-15. Radial distributions of fractional surface coverage calculated for the deposit model with time as a parameter: A) $K_{sp,Fe(OH)_3} = 6.3 \times 10^{-36}$; and B) $K_{sp,Fe(OH)_3} = 6.3 \times 10^{-38}$.

Assuming the convection can be neglected and the time variable is considered, the concentration of dissolved oxygen can be expressed as the conservation equation in an one-dimensional form as

$$\frac{\partial c_{O_2}}{\partial t} = D_{O_2} \nabla^2 c_{O_2} \tag{4–1}$$

The temperature for heat conduction can be described by

$$\frac{\partial T}{\partial t} = \alpha \nabla^2 T \tag{4–2}$$

The analytic solutions for both Equation 4–1 and Equation 4–2 can be obtained by using the same approach. Therefore, the oxygen concentration profile for diffusion equation

is similar to the temperature profile for heat conduction. Section 4.1.3.1 provides a comparison between the concentration profile for unsteady-state diffusion equation using the finite-element package (COMSOL Multi-physics) with those using an analytic method. The iteration procedure in the analytic solution was conducted in MATLAB software. A rectangular geometry was used as the slab, and the entire domain was governed by diffusion equation given as Equation 4–1. At $y = \pm b$, the concentrations were set at saturated concentration c_1. Both analytic and numerical data were analyzed by dimensionless variables.

A solid slab occupying the space between $y = -b$ and $y = +b$ was initially at concentration c_0. At time $t = 0$ the surfaces at $y = \pm b$ are suddenly raised to c_1 and maintained that value [63]. Governing equation is given by Equation 4–2. The slab remains at T_0 at $t = 0$. For $t > 0$, concentration raises to T_1 at $y = \pm b$. Four important methods are used to solve unsteady-state diffusion problems analytically: combination of variables, separation of variables, sinusoidal response, and Laplace transform. The analytic solution of concentration can be written as a function of y in infinite series given by

$$\frac{c_1 - c}{c_1 - c_0} = 2\sum_{n=0}^{\infty} \frac{(-1)^n}{(n+\frac{1}{2})\pi} \exp[-(n+\frac{1}{2})^2\pi^2 \frac{\alpha t}{b^2}] \cos(n+\frac{1}{2})\frac{\pi y}{b} \tag{4–3}$$

The concentration profile was calculated by iterative methods in MATLAB as shown in Figure 4-16A; whereas, the concentration profile for unsteady-state diffution in a sphere of radius a is also calculated and presented in Figure 4-16B. It indicates the difference between the analytic and numerical solutions is small. The errors defined as the relative percentage difference between the magnitude calculated by the analytic solution and that by the numerical solution in COMSOL. Table 4-4 demonstrates the trend of the error decreasing with smaller time steps and higher mesh density.

4.1.3.2 Drop Size

As discussed in Section 4.1.3.2, the cathodic reaction is limited by mass transfer of oxygen. The diffusion of oxygen is affected by the size of the water droplet because the

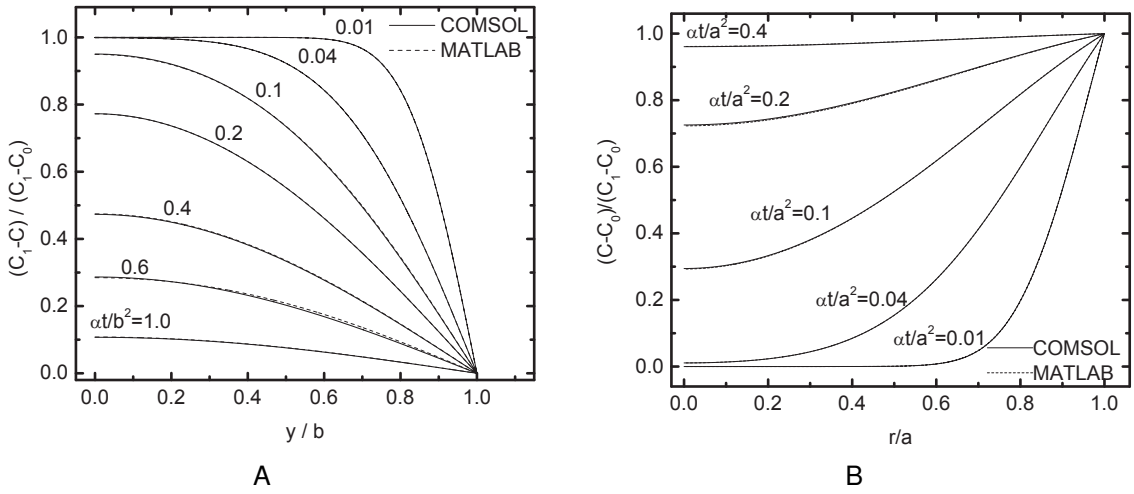

A B

Figure 4-16. Concentration profiles for unsteady-state diffusion. The initial concentration of the slab is c_0, and c_1 is the concentration imposes at the surfaces for time $t > 0$. A) for a slab of finite thickness $2b$; and B) in a sphere of radius a.

Table 4-4. Errors for different mesh density and time step.

	Coarse Mesh with $1s$ Time Step (%)	Finer Mesh with $1ms$ Time Step (%)
α=0.01	08.78	0.21
0.04	13.74	0.21
0.1	16.12	0.04
0.2	20.53	0.15
0.4	89.62	0.33
0.6	09.28	2.45
1	61.11	0.55

drop size controls the distance between the water-air interface and the metal surface. As shown in Figure 4-17, the mass-transfer-limited current density increases with decreasing drop radius. The mass-transfer-limited plateau is more apparent when the droplet size is larger; therefore, 1 mm was used for the radius of the droplet.

4.1.3.3 Drop Eccentricity

The shape of droplet also affects the diffusion-limited current density. As the shape of the droplet becomes more elliptical, the variation in concentration of oxygen along the electrode surface is reduced and the average mass-transfer-limited current density of oxygen is increased. The effect is illustrated in Figure 4-18, which illustrates that

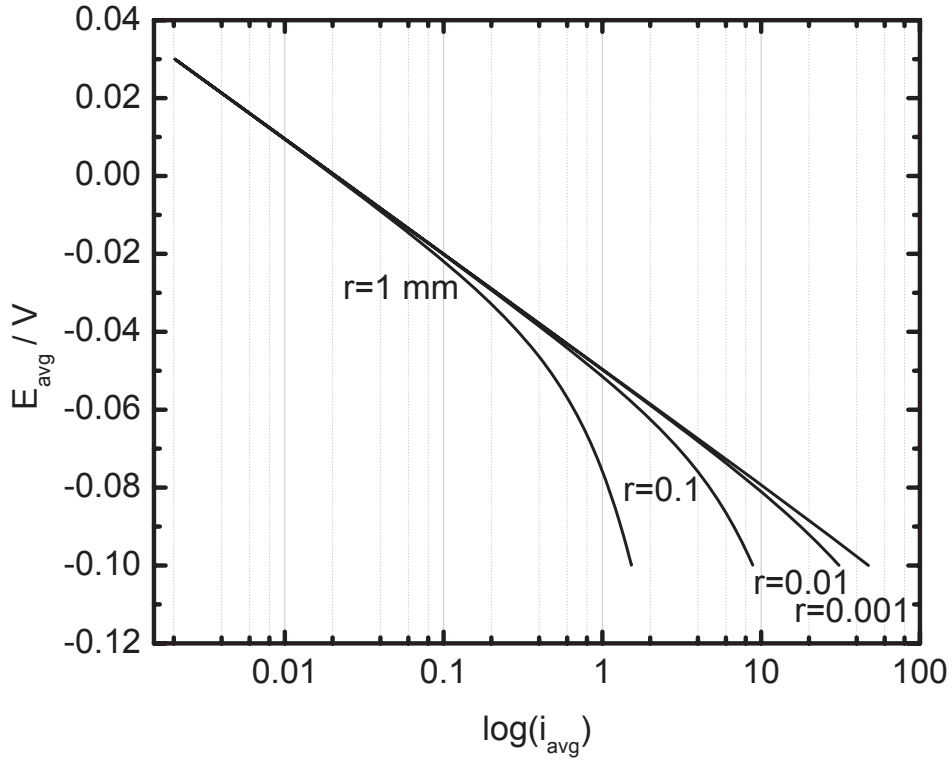

Figure 4-17. Cathodic polarization curve for oxygen reduction with drop radius as a parameter.

limiting diffusion current rises as the droplet becomes more elliptical. The eccentricity 1 was applied in the following models in order to obtain large concentration gradient of dissolved gas.

4.1.3.4 Mesh Density

A finer mesh density provides more accurate results, but requires more calculation time. As the number of elements in the mesh is doubled and the size of elements at the peripheral is reduced, concentration polarization curve shifts. Cathodic and anodic polarization curves are presented in Figure 4-19 with mesh density as a parameter. The anodic reaction is unaffected by the change in mesh density; whereas, the cathodic reaction is influenced at higher current densities, where the influence of mass transfer is more apparent. A finer mesh is needed to model the regions along the electrode surface and at the metal-liquid-air interface where the oxygen concentration gradients

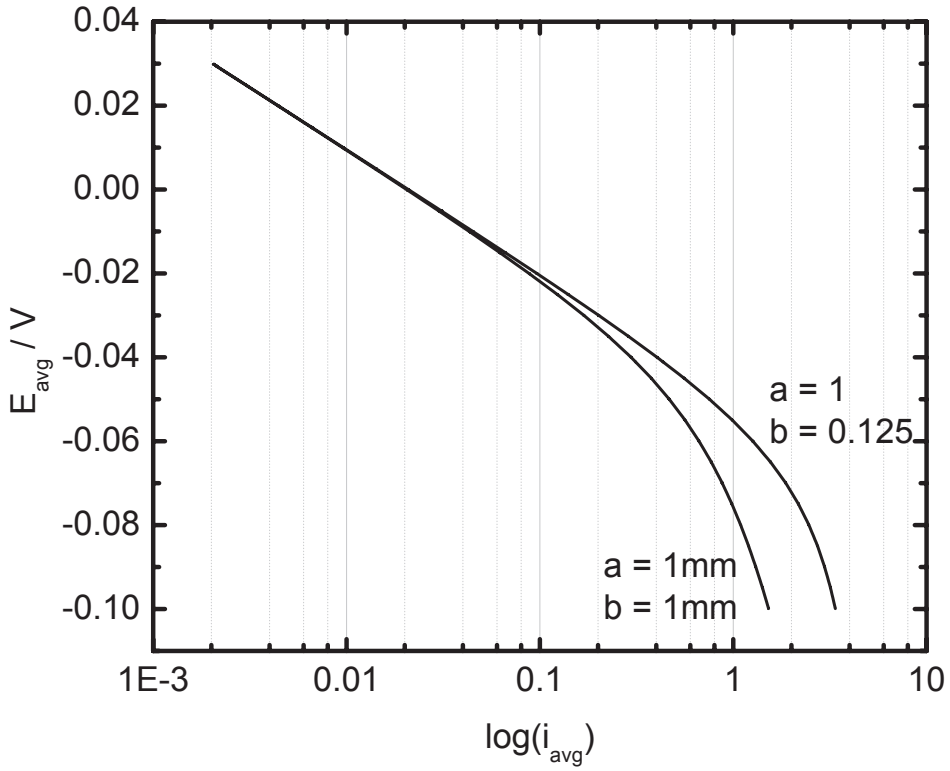

Figure 4-18. Cathodic polarization curve for oxygen reduction with drop shape as a parameter.

are largest. Possible sources of the errors include the mesh density and the chosen time step. Finer mesh might be required

4.1.3.5 Deposit Model - Influence of Uncovered Region

The ratio of the radius covered by the deposits to the outer bulk solution region radius (r_s/r_b) as shown in Figure 4-20 was studied since it could be an influential factor for the initiation of pitting. As illustrated in Figure 4-21, the potential variation depended strongly on r_s/r_b. A large potential variation at large values of r_s/r_b as shown in Figure 4-11A may result in pitting and, thus, under-deposit corrosion.

4.2 De-aerated Model-CO_2

The objective of Section 4.2 is to extend the aerated under-deposit corrosion model to the case of de-aerated conditions containing dissolved CO_2. It employs the same approach as the O_2 model to deal with the concentration gradient of ionic species,

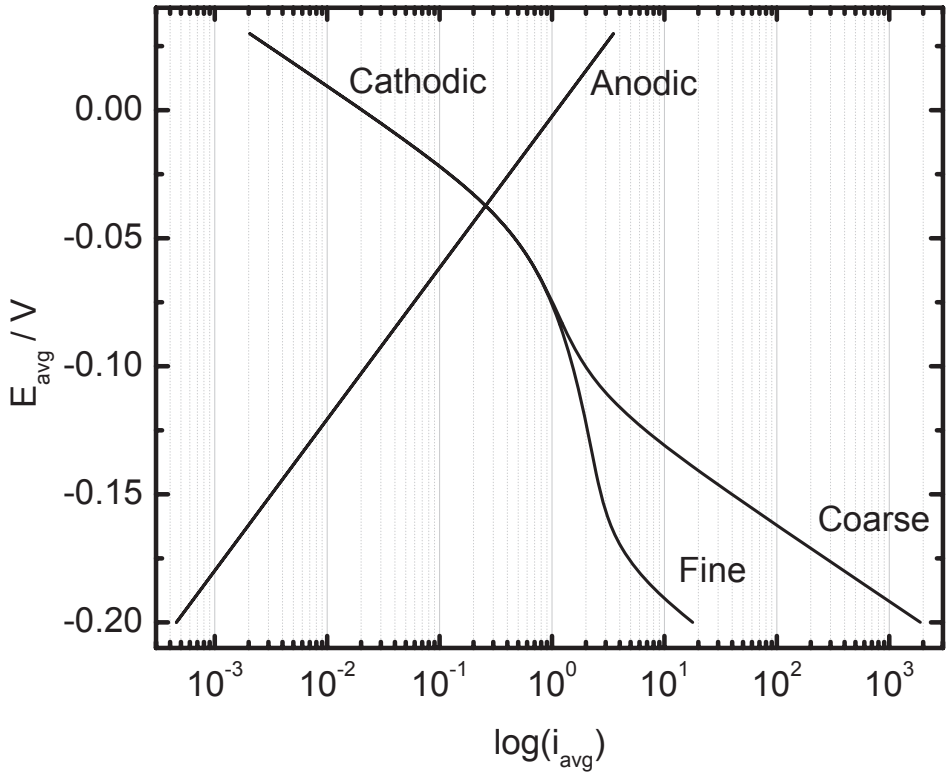

Figure 4-19. Cathodic and anodic polarization curves with mesh density as a parameter.

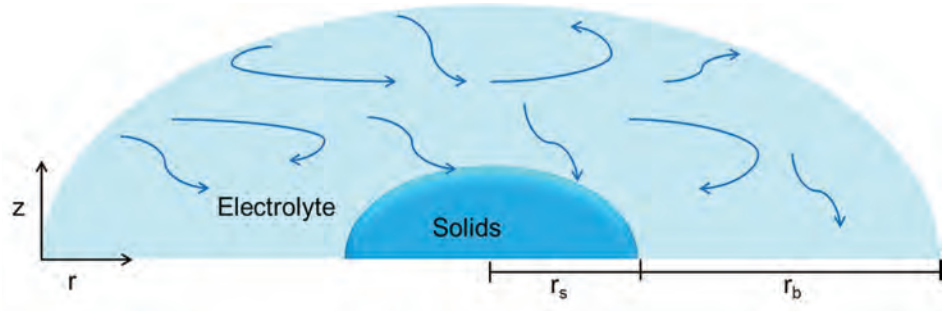

Figure 4-20. Schematic representation of the Deposit model.

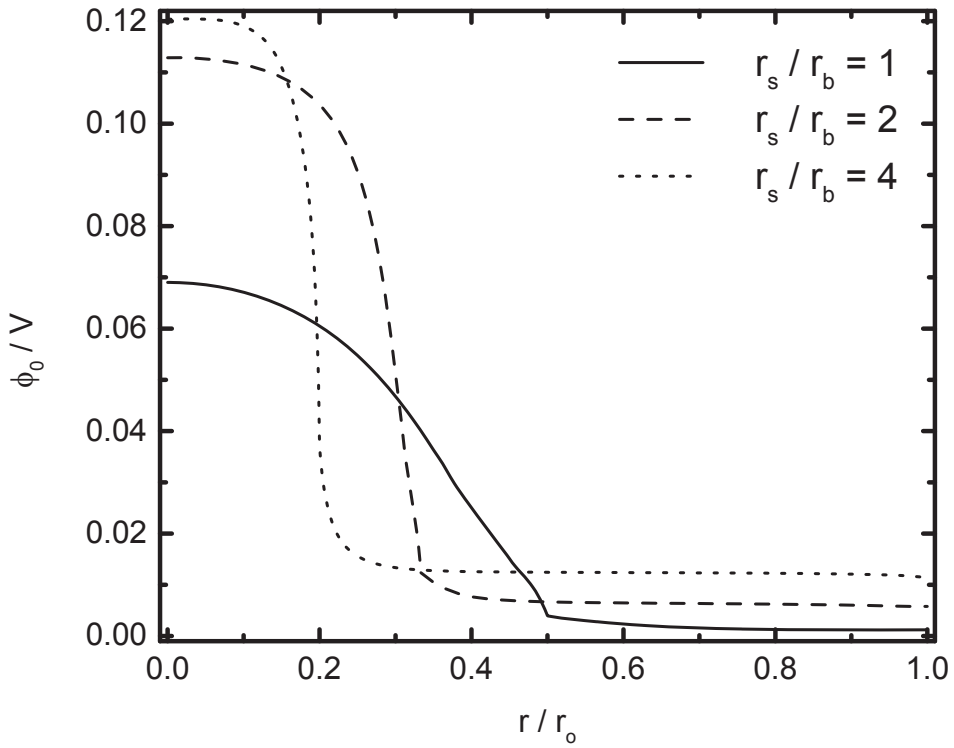

Figure 4-21. Calculated potential distributions along electrode surface at the time of maximum potential variation with r_s/r_b as a parameter.

more complex homogeneous and heterogeneous reactions, and the turbulent flow behavior in the de-aerated bulk region. For corrosion in the condition containing CO_2, the deprotonation of carbonic species plays an important role. The mechanism of dissociation of carbonic species has been studied since 1975 and large number of mechanisms have been proposed. In this work, two mechanisms of the hydration and dissociation of CO_2 were employed and studied. One was proposed by Remita [58], which assumed that the first dissociation step of H_2CO_3 was fast enough to ignore the existence of H_2CO_3. Hydrogen evolution evolved directly from H^+ was assumed to be the only contribution of the cathodic reaction. The model adopted by the mechanism proposed by Remita [58] is referred as Remita's Model in the following contents. Another mechanism was proposed by Nordsveen [47], which increased the complexity of this model by involving the hydration of CO_2, two dissociation steps of H_2CO_3, and cathodic reactions were assumed to be the hydrogen evolution evolved from both H^+ and H_2CO_2.

The model adopted by the mechanism proposed by Nordsveen [47] is referred as Nordsveen's Model in the following contents. The solution containing dissolved CO_2 shows that, with small modifications, the under-deposit model can be adapted to other conditions by adding or removing species and reactions.

Under certain conditions, the metal surface under the dissolved CO_2 solutions can experience both active and passive behavior caused by $FeCO_3$. To explore these conditions, parameters were taken from the values Remita [58] and Nordsveen [47] used to allow the open-circuit potential distribution on the metal surface to encompass the region between passive and active behavior. The parameters used in the calculations are presented in Table 4-5, Table 4-6, and 4-7. Models for solutions containing dissolved CO_2 involving more complicated reactions than the solutions containing dissolved O_2; therefore, stability issue was observed. A smaller time step and finer mesh size were suggested to obtain more stable results.

4.2.1 The Comparisons between Mechanisms Proposed by Remita and Nordsveen

Two corrosion mechanisms for the solution containing dissolved CO_2 were employed and compared in the one-quarter-ellipse geometry. The mechanism proposed by Remita was under the assumption that the existence of H_2CO_3 can be neglected and only the hydrogen evolution directly from H^+ plays a role in the cathodic reaction. Nordsveen took the existence of H_2CO_3 into account and assumed that hydrogen evolved from both H^+ and H_2CO_3. The mechanism proposed by Nordsveen described the rate constants as a function of temperature, pressure, and the composition of a solution. In the contrary, for the mechanism proposed by Remita, the rate constants are the experimental results at 25 °C and 1 atm. In this work, both models were calculated at 25 °C and 1 atm to compare the results. It took 40 times longer for the Nordsveen's model to obtain the same surface coverage of $FeCO_3$ compared with the Remita's model.

Table 4-5. Parameters for the simulations in CO_2 Deposit model with the mechanism proposed by Remita.

CO_2 Droplet Model (one-quarter ellipse Figure 3-2A)		
i_{0,H_2}	4.0×10^{-3}	A/cm^2
β_{H_2}	0.07	V/decade
$i_{0,Fe}$	3.89×10^{-3}	A/cm^2
$b_{Fe^{2+}}$	0.06	V/decade
$i_{p,Fe}$	1.00×10^{-16}	A/cm^2
D_{H^+}	9.31×10^{-5}	cm^2/s
D_{OH^-}	5.26×10^{-5}	cm^2/s
$D_{Fe^{2+}}$	0.72×10^{-5}	cm^2/s
D_{O_2}	1.97×10^{-5}	cm^2/s
$D_{NO_3^-}$	1.90×10^{-5}	cm^2/s
D_{K^+}	1.98×10^{-5}	cm^2/s
D_{CO_2}	1.96×10^{-5}	cm^2/s
$D_{HCO_3^-}$	1.05×10^{-5}	cm^2/s
$D_{CO_3^{2-}}$	9.20×10^{-5}	cm^2/s
K_w	9.02×10^{-9}	mol^2/m^6
K_{ca}	1.78×10^{-1}	mol/m^3
K_{bi}	4.94×10^{-8}	mol/m^3
H_{CO_2}	3.3×10^{-5}	mol/cm^3 bar
T	298.15	K
R	8.3143	J/mol K
$c_{CO_2}(0)$	$P_{CO_2} \times H_{CO_2}$	mol/m^3
$c_{HCO_3^-}(0)$	0.113	mol/m^3
$c_{CO_3^{2-}}(0)$	4.7×10^{-8}	mol/m^3
$c_{H^+}(0)$	0.142	mol/m^3
$c_{OH^-}(0)$	7.04×10^{-8}	mol/m^3
$c_{Fe^{2+}}(0)$	0	mol/m^3
$K_{sp,FeCO_3}$	1.5×10^{-11}	
P_{CO_2}	1	bar

For the mechanism without the existence of H_2CO_3, the total current density along the metal surface after the formation of precipitate were shown in Figure 4-22A. The calculated total current density based on the mechanisms proposed by Nordsveen were plotted in Figure 4-22B. The corresponding potential were plotted in Figure 4-23 which indicates that the corrosion occurred in the whole covered region for both mechanisms. The cathodic reaction was favored in the region close to where

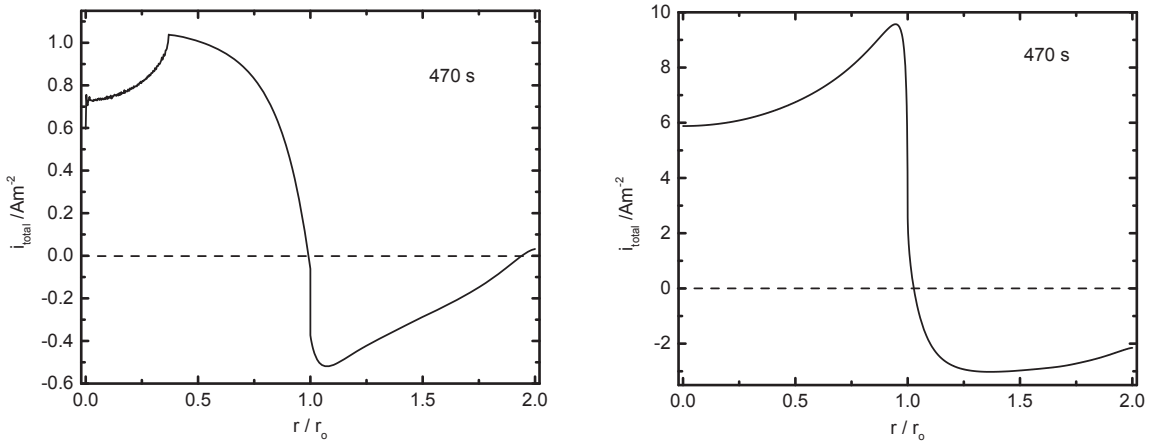

A B

Figure 4-22. The distribution of total current density at $t = 470$ s for the mechanisms A) proposed by Remita B) proposed by Nordsveen of the CO_2 Deposit model.

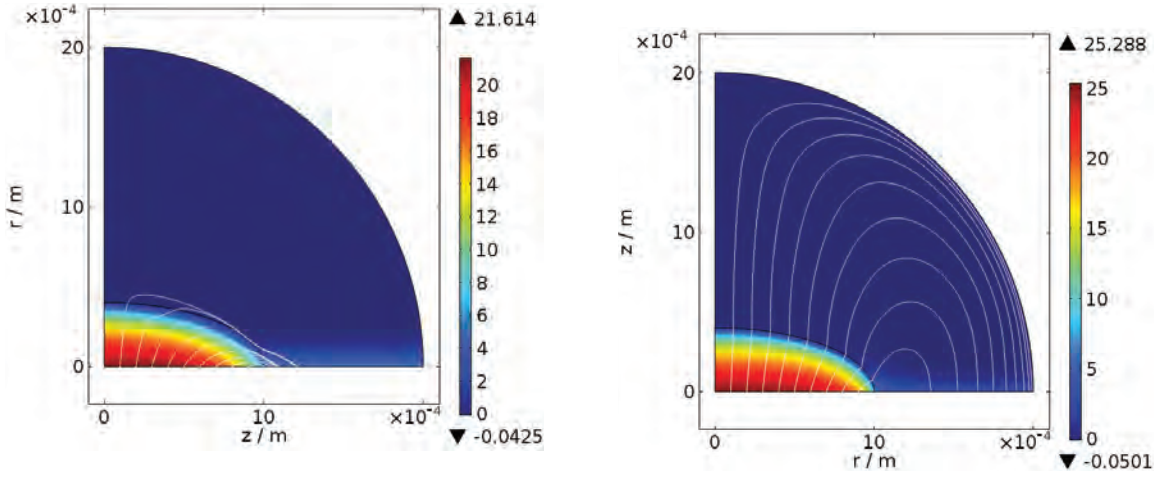

A B

Figure 4-23. The potential distributions at $t = 470$ s for the mechanisms A) proposed by Remita B) proposed by Nordsveen of the CO_2 Deposit model.

Table 4-6. Parameters for the simulations in CO_2 Droplet model with the mechanism proposed by Nordsveen.

CO_2 Droplet Model (one-quarter ellipse Figure 3-2A)					
i_{0,H_2}	5.0×10^{-6}	A/cm^2	T	298.15	K
i_{0,H_2CO_3}	6.0×10^{-6}	A/cm^2	R	8.3143	J/mol K
$c_{H^+,ref}$	0.1	mol/m^3	ρ_s	3.9	g/cm^3
$c_{H_2CO_3,ref}$	0.1	mol/m^3	δ	7.0×10^{-9}	m
b_{H_2}	0.12	V/decade	$c_{CO_2}(0)$	$P_{CO_2} \times K_{sol}$	
$b_{H_2CO_3}$	0.2	V/decade	$c_{H_2CO_3}(0)$	0.08215	mol/m^3
$E_{H_{2,ref}}$	0.12	V/decade	$c_{HCO_3^-}(0)$	0.12102	mol/m^3
$E_{H_2CO_{3,ref}}$	0.2	V	$c_{CO_3^{2-}}(0)$	4.9449×10^{-8}	mol/m^3
$i_{0,Fe}$	1×10^{-4}	A/cm^2	$c_{H^+}(0)$	0.12102	mol/m^3
$b_{Fe^{2+}}$	0.04	V/decade	$c_{OH^-}(0)$	7.451×10^{-8}	mol/m^3
$E_{Fe^{2+}_{ref}}$	-0.44	V	$c_{Fe^{2+}}(0)$	0	mol/m^3
$i_{p,Fe}$	1.00×10^{-1}	A/cm^2	$K_{sp,FeCO_3}$	1.29×10^{-11}	
D_{H^+}	9.31×10^{-5}	cm^2/s	A_p	1.77×10^{12}	
D_{OH^-}	5.26×10^{-5}	cm^2/s	E_a	64.9	KJ/mol
$D_{Fe^{2+}}$	0.72×10^{-5}	cm^2/s	P_{CO_2}	1×10^5	Pa
D_{O_2}	1.97×10^{-5}	cm^2/s	*ionic*	0	
$D_{NO_3^-}$	1.90×10^{-5}	cm^2/s	K_{sol}	0.031841	
D_{K^+}	1.98×10^{-5}	cm^2/s			
D_{CO_2}	1.96×10^{-5}	cm^2/s			
$D_{H_2CO_3}$	2.00×10^{-5}	cm^2/s			
$D_{HCO_3^-}$	1.05×10^{-5}	cm^2/s			
$D_{CO_3^{2-}}$	9.20×10^{-5}	cm^2/s			
K_w	9.02×10^{-9}	mol^2/m^6			
K_{hy}	2.58×10^{-3}				
K_{ca}	1.78×10^{-1}	mol/m^3			
K_{bi}	4.94×10^{-8}	mol/m^3			
$k_{hy,f}$	2.60×10^{-2}	/s			
$k_{hy,b}$	10.08	/s			

the corrosion occurred for the mechanism proposed by Remita; while the whole outer surface acted as a cathode for the mechanism proposed by Nordsveen. The cathodic current densities of the hydrogen evolution from H_2CO_3 and H^+ were plotted in Figure 4-24. Figure 4-24B indicates the significant contribution of hydrogen evolution from H_2CO_3 in cathodic reactions. The parameters applied in Remita's model were based on experiments conducted at room temperature and pressure; while most of

Table 4-7. Parameters for the simulations in CO_2 Deposit model with the mechanism proposed by Nordsveen.

CO_2 Deposit Model (two-quarter ellipse Figure 3-2B)					
i_{0,H_2}	5.0×10^{-6}	A/cm^2	T	298.15	K
i_{0,H_2CO_3}	6.0×10^{-6}	A/cm^2	R	8.3143	J/mol K
$c_{H^+,ref}$	0.1	mol/m^3	ρ_s	3.9	g/cm^3
$c_{H_2CO_3,ref}$	0.1	mol/m^3	δ	7.0×10^{-9}	m
b_{H_2}	0.12	V/decade	$c_{CO_2}(0)$	$P_{CO_2} \times K_{sol}$	
$b_{H_2CO_3}$	0.2	V/decade	$c_{H_2CO_3}(0)$	0.08215	mol/m^3
$E_{H_{2,ref}}$	0.12	V/decade	$c_{HCO_3^-}(0)$	0.12102	mol/m^3
$E_{H_2CO_{3,ref}}$	0.2	V	$c_{CO_3^{2-}}(0)$	4.9449×10^{-8}	mol/m^3
$i_{0,Fe}$	1×10^{-4}	A/cm^2	$c_{H^+}(0)$	0.12102	mol/m^3
$b_{Fe^{2+}}$	0.04	V/decade	$c_{OH^-}(0)$	7.451×10^{-8}	mol/m^3
$E_{Fe^{2+}_{ref}}$	-0.44	V	$c_{Fe^{2+}}(0)$	0	mol/m^3
$i_{p,Fe}$	1.00×10^{-1}	A/cm^2	$K_{sp,FeCO_3}$	1.29×10^{-11}	
D_{H^+}	9.31×10^{-5}	cm^2/s	A_p	1.77×10^{12}	
D_{OH^-}	5.26×10^{-5}	cm^2/s	E_a	64.9	KJ/mol
$D_{Fe^{2+}}$	0.72×10^{-5}	cm^2/s	P_{CO_2}	1×10^5	Pa
D_{O_2}	1.97×10^{-5}	cm^2/s	*ionic*	0	
$D_{NO_3^-}$	1.90×10^{-5}	cm^2/s	K_{sol}	0.031841	
D_{K^+}	1.98×10^{-5}	cm^2/s	ϵ	$0.2^{(1.5)}$	
D_{CO_2}	1.96×10^{-5}	cm^2/s	ν	1.05×10^{-6}	m^2/s
$D_{H_2CO_3}$	2.00×10^{-5}	cm^2/s	A_1	1.0972×10^{-4}	
$D_{HCO_3^-}$	1.05×10^{-5}	cm^2/s	A_2	3.295×10^{-6}	
$D_{CO_3^{2-}}$	9.20×10^{-5}	cm^2/s			
K_w	9.02×10^{-9}	mol^2/m^6			
K_{hy}	2.58×10^{-3}				
K_{ca}	1.78×10^{-1}	mol/m^3			
K_{bi}	4.94×10^{-8}	mol/m^3			
$k_{hy,f}$	2.60×10^{-2}	/s			
$k_{hy,b}$	10.08	/s			

the parameters in the Nordsveen's mechanism were obtained from experiments with temperatures from 40°C to 60°C. It represents that the existence of H_2CO_3 is not negligible for high temperature and the mechanism proposed by Nordsveen has the limitation of temperature range. However, protective iron carbonate or iron carbide films usually are observed under higher temperature and pressure. The mechanism proposed by Nordsveen can provide more appropriate approach to study the corrosion with

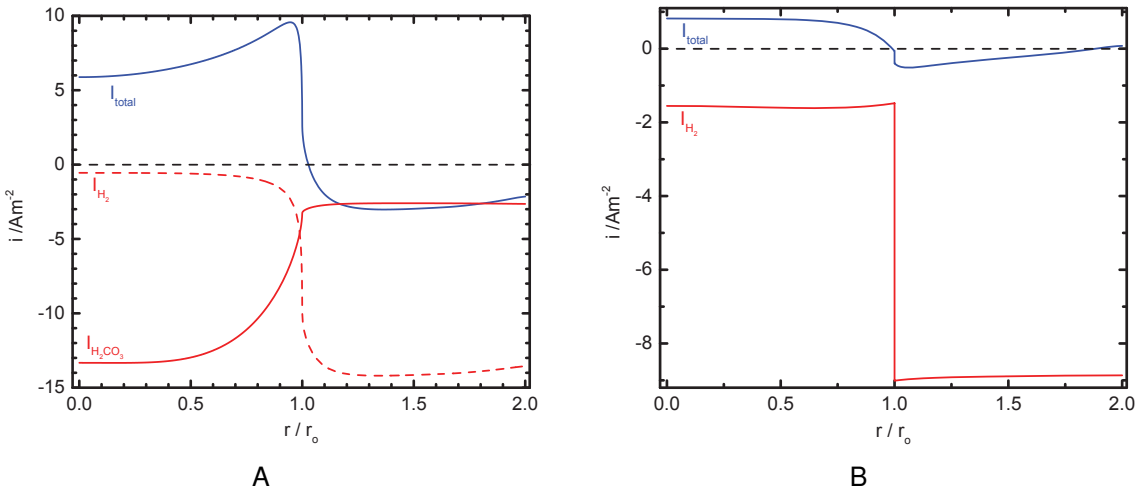

Figure 4-24. The distributions of current density at $t = 470$ s for the mechanisms A) proposed by Remita B) proposed by Nordsveen of the CO_2 Deposit model. ch4

the formation of precipitates. Therefore, the mechanism proposed by Nordsveen was employed in the two-concentric-quarter-ellipse geometry to study the galvanic coupling effect resulted from the formation of precipitates.

4.2.2 Passivation Behavior

The results were presented in terms of two sets of calculations. For the one-quarter -ellipse geometry (CO_2 Droplet in Table 4-6), the shift of passivated area can be illustrated in the changes of the total current density. The two-concentric-quarter-ellipse geometry (CO_2 Deposit in Table 4-7) was applied to evaluate under-deposit corrosion and the influences of both the formation of precipitates and the surrounded turbulent flow. The precipitates started to form from the center and accumulated towards to the periphery because the lack of CO_3^{2-} in the solution. The concentration of Fe^{2+} is the criteria in the formation of $FeCO_3$. The pH value above the metal surface was presented to show the ability of predicting local concentration of ionic species in both Droplet and Deposit models.

4.2.2.1 CO_2 Droplet Model

The role of film passivation is evident in Figure 4-25 in which distribution of current

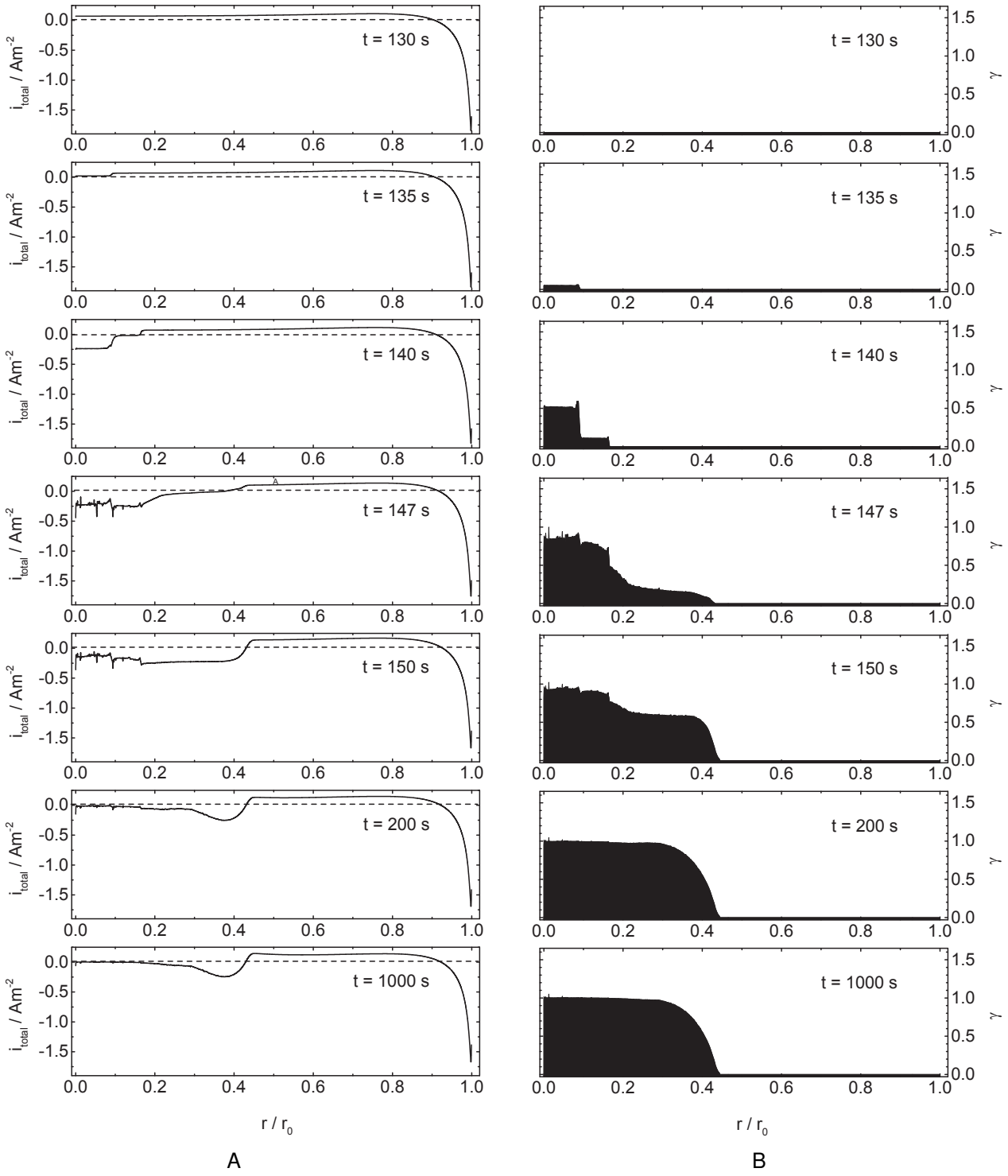

Figure 4-25. Radial distributions of calculated A) total current density and B) surface coverage (γ) at the electrode surface with time as a parameter for the CO_2 Droplet model.

density (Figure 4-25A) and surface coverage (Figure 4-25B) were presented at different times for the CO_2 Droplet model. At short times, due to the greater accessibility to carbon dioxides, the cathodic reaction dominates at the periphery of the droplet. Ferrous ions were assumed to be produced by the anodic reaction and react with carbonate ions produced by the dissociation reactions of carbonic acid to form ferrous carbonate. The formation of $FeCO_3$ can be indicated by the surface coverage which is shown in Figure 4-25B. As time increases, the surface coverage approaches the full coverage value ($\gamma = 1$). The precipitates deposited from the center and extended to the periphery region until the system reaches equilibrium. The precipitate $FeCO_3$ was assumed to be protective and to passivate only the iron dissolution reaction. Ferrous ions are the criteria of forming ferrous carbonate since carbonate ions are limited by the slow hydration of carbon dioxides. The active-passive transition was assumed to be a consequence of the formation of precipitates. When the system reaches the equilibrium state, corrosion occurs at the covered region close to the boundary of occluded and the bulk solution region. The corresponding changes of potential distribution were plotted in Figure 4-26. The precipitates act as the protective film on the metal surface and shield the reacting surface. The pH value decreases after the formation of $FeCO_3$ since the consumption of CO_3^{2-} prompt the formation of H^+. The pH value right above the surface was plotted in Figure 4-27 with time as a parameter and indicates a large change in a short period of time (0.1 s to 130 s). Smaller time step and finer mesh were expected to be employed to understand the relationship of the two cathodic reaction (Equation 3–32 and Equation 3–30), two dissociation steps of H_2CO_3, and hydration of CO_2.

4.2.2.2 CO_2 Deposit Model

The influence of turbulent flow can be observed in Figure 4-28. The surrounded turbulent flow enhanced the cathodic reaction in the outer region; therefore, the corrosion under the covered region became more severe. After the existing carbon dioxide was all consumed, the diffused carbon dioxide brought to the reacting surface

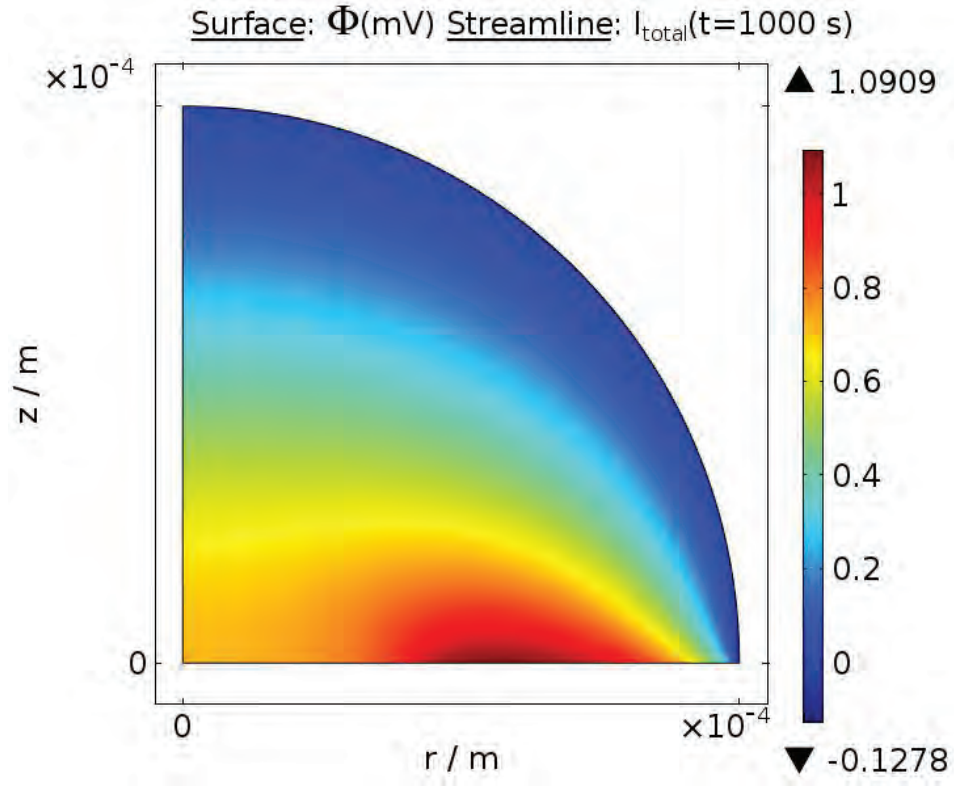

Figure 4-26. Potential distribution for the false color representation and streamline representation of current density at $t = 1000$ s calculated for the CO_2 Droplet model.

in the turbulent flow was faster than the one in the covered region. As a consequence, the cathodic reaction was favorable in the surrounding area while the anodic reaction dominated in the center. The passivation behavior was observed as the result of the formation of precipitates which is shown in Figure 4-29 and 4-30. Iron carbonates was assumed to be semi-conductive in this calculation and to passivate only the iron dissolution reaction. The corresponding changes of potential distribution were plotted in Figure 4-30. The maximum potential difference was obtained at the initiation of precipitation with the maximum anodic current density. It provides sufficient ferrous and carbonate ions for precipitation. The potential distribution plotted in Figure 4-31 when the covered region reaches the maximum surface coverage. The precipitates continues accumulating on the metal surface and the corrosion remains active under the

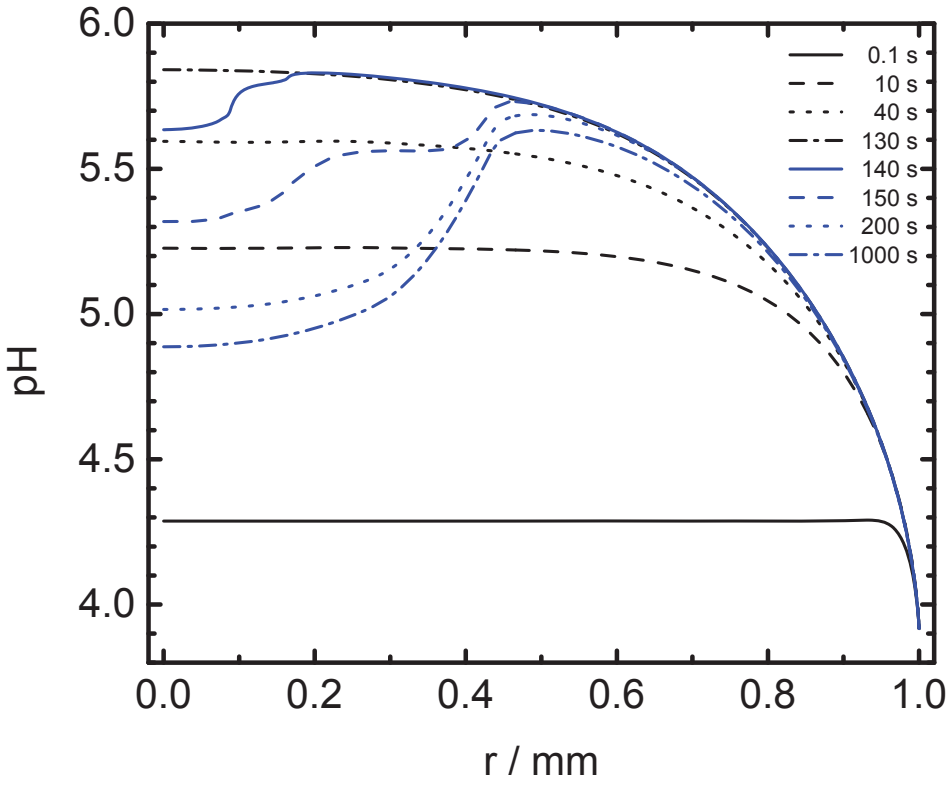

Figure 4-27. The pH distribution as a function of time calculated for the CO_2 Droplet model.

predefined covered region due to the carbon dioxides gradient driven by the surrounding turbulent flow.

4.2.3 The Influence of Time Step

More complicated homogeneous reactions and cathodic reaction were involved in the CO_2 model, such as the hydration of CO_2, the two dissociate steps of H_2CO_3, and two cathodic reactions (the reduction of H^+ and H_2CO_3). The rates of each reaction vary widely and more iterations were required for the CO_2 model compared with the O_2 model. The hydration reaction was assumed to be much slower compared with the dissociation reactions. A large change of pH was observed with a short period of time (0.1 s to 130 s in Figure 4-27) as the reaction progresses. Different cathodic reaction was preferred at different stage of reaction; therefore, time step plays an important role in the CO_2 model in order to obtain more correct and stable results as shown in Figure

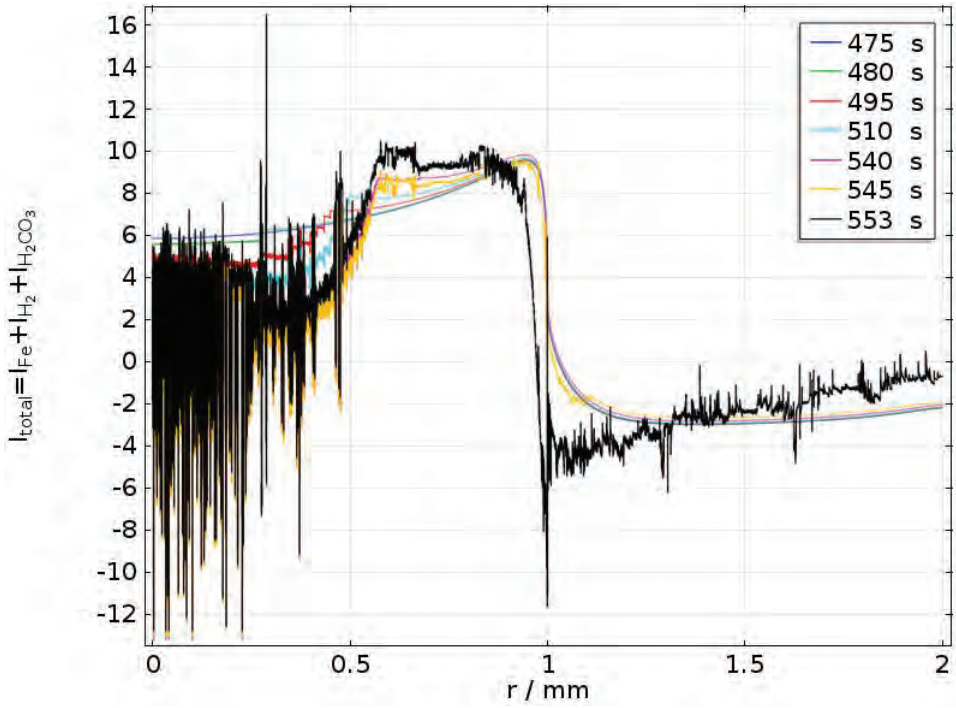

Figure 4-28. Radial distributions of calculated total current density at the electrode surface with time as a parameter for the CO_2 Deposit model.

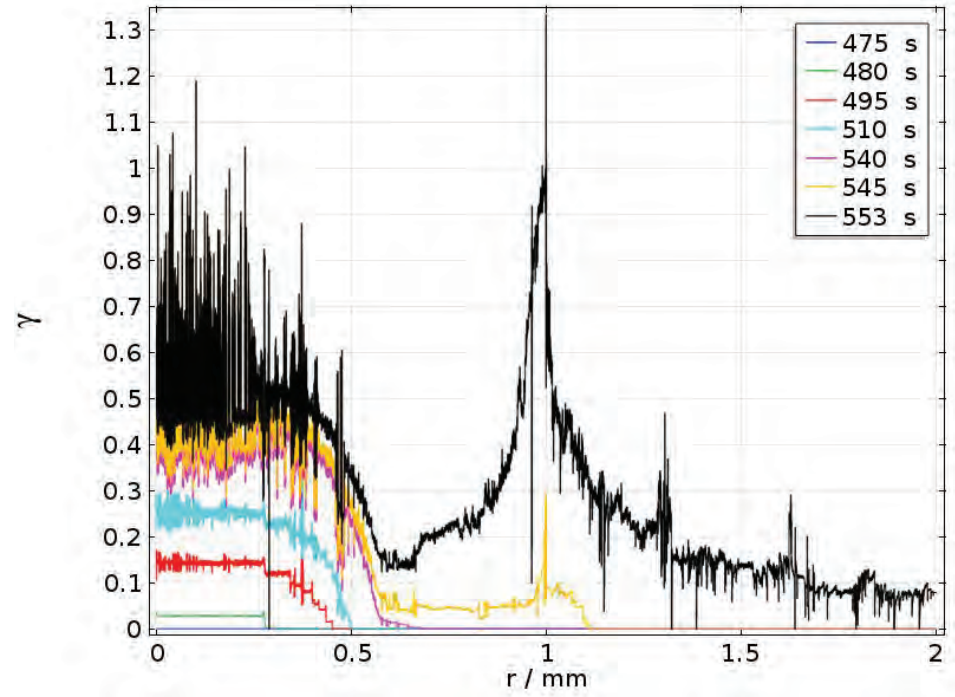

Figure 4-29. Radial distributions of calculated surface coverage at the electrode surface with time as a parameter for the CO_2 Deposit model.

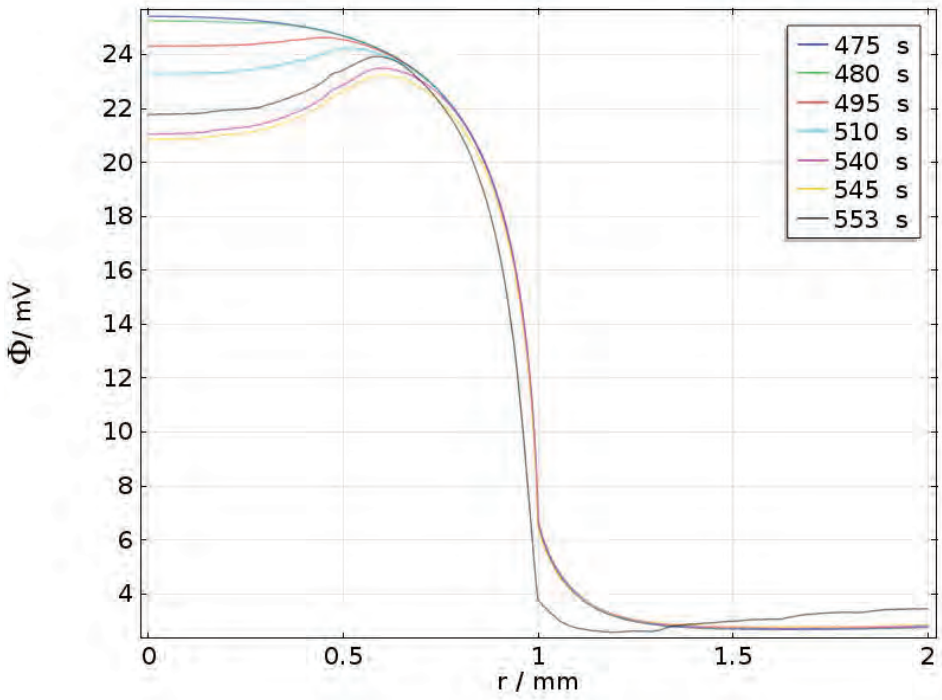

Figure 4-30. Potential distribution along electrode surface with time as a parameter calculated for the deposits surrounded by bulk solutions.

4-32. The smaller time step not only improve the roughness of the results but also the value of it. Smaller time step was required in more complicated model to obtain more accurate results.

4.2.4 The Influence of Mesh Size

The spikes and roughness of the results were observed in both Droplet and Deposit model. The results obtained from the Droplet model was improved by using smaller time step, however, the results obtained from Deposit model can not be improved by applying smaller time step. The geometry was more complicated for the Deposit model compared with the Droplet model; therefore, using finer mesh was expected to obtain a more accurate results. For the Droplet model, singularity problems could occur at the periphery. The distribution of total current density along the metal surface with mesh size as the parameter was plotted in Figure 4-33. It shows the calculated results changed with different mesh size, especially for the region fairly close to the water-air interface.

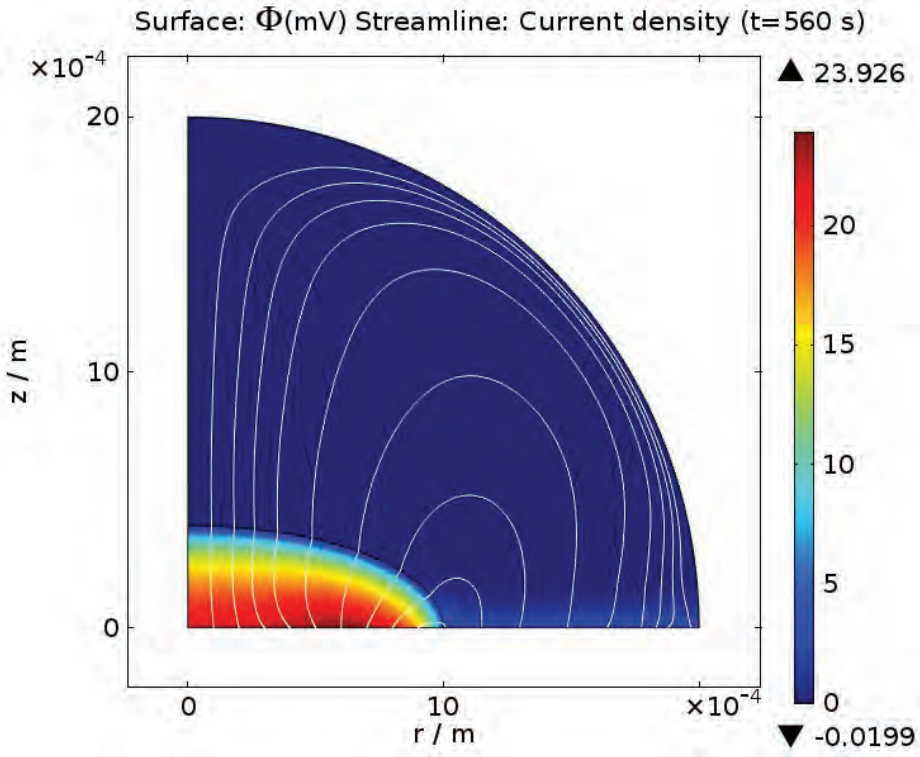

Figure 4-31. Potential distribution for the false color representation and streamline representation of current density at t= 560 s calculated for the deposits surrounded by bulk solutions.

Table 4-8. Differences for the simulations in CO_2 Droplet model with different mesh size by Remita.

Maximum Mesh Size / m	4×10^{-5}	1×10^{-5}	1×10^{-6}	1×10^{-7}	1×10^{-8}
ε from Equation 4–4	6.07×10^{-1}	2.98×10^{-2}	1.42×10^{-2}	6.65×10^{-4}	0

The comparison of different mesh size can be calculated by using Equation 4–4 as follows

$$\varepsilon = \left| \frac{\left(\int_0^r i_{\text{ref}}\, r\mathrm{d}r\mathrm{d}\theta\right) - \left(\int_0^r i\, r\mathrm{d}r\mathrm{d}\theta\right)}{\int_0^r i_{\text{ref}}\, r\mathrm{d}r\mathrm{d}\theta} \right| \quad \text{for } i \text{ and } i_{\text{ref}} > 0 \tag{4–4}$$

where i_{ref} is the total current density calculated by using the 4×10^{-8} /m as the maximum mesh size which was also used in the following calculations. The results were presented in Table 4-8. Finer mesh at the periphery was employed in the Deposit model, but it did not improve the quality of the results after the formation of precipitates as shown in Figure 4-34. The roughness of the curves was still observed after the formation of precipitates in the covered region. The results was not changed by using

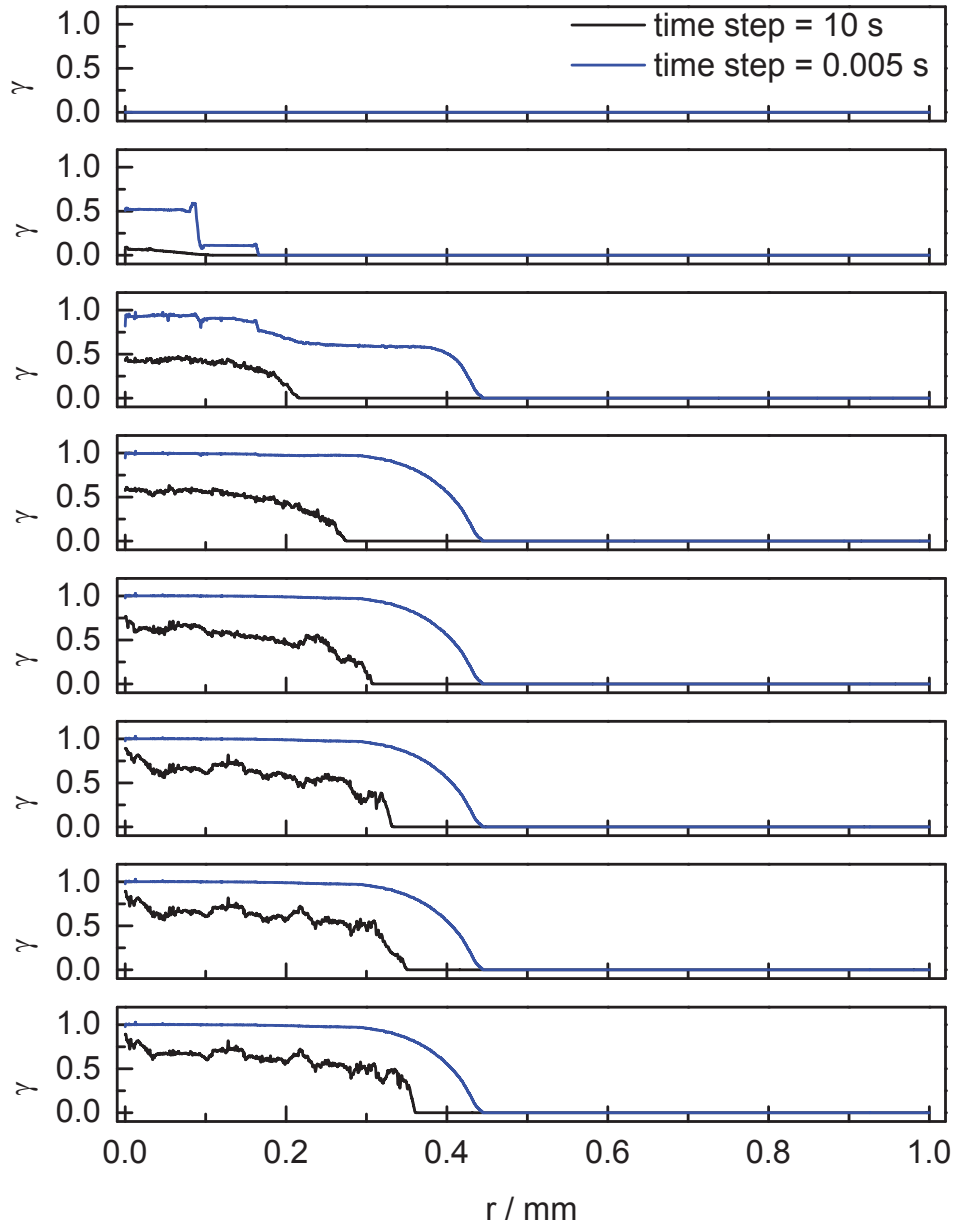

Figure 4-32. Radial distributions of calculated surface coverage at the electrode surface with time step as a parameter for the CO_2 Droplet model.

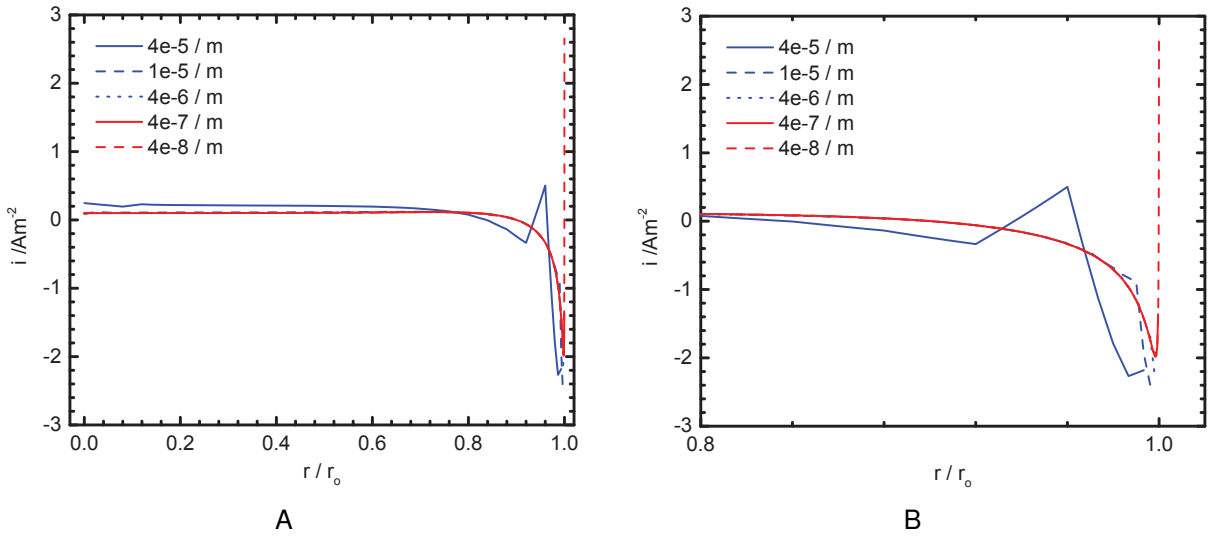

Figure 4-33. Radial distributions of calculated A) total current density and B) the total current density near the periphery region at the electrode surface with time as a parameter for the CO_2 Droplet model.

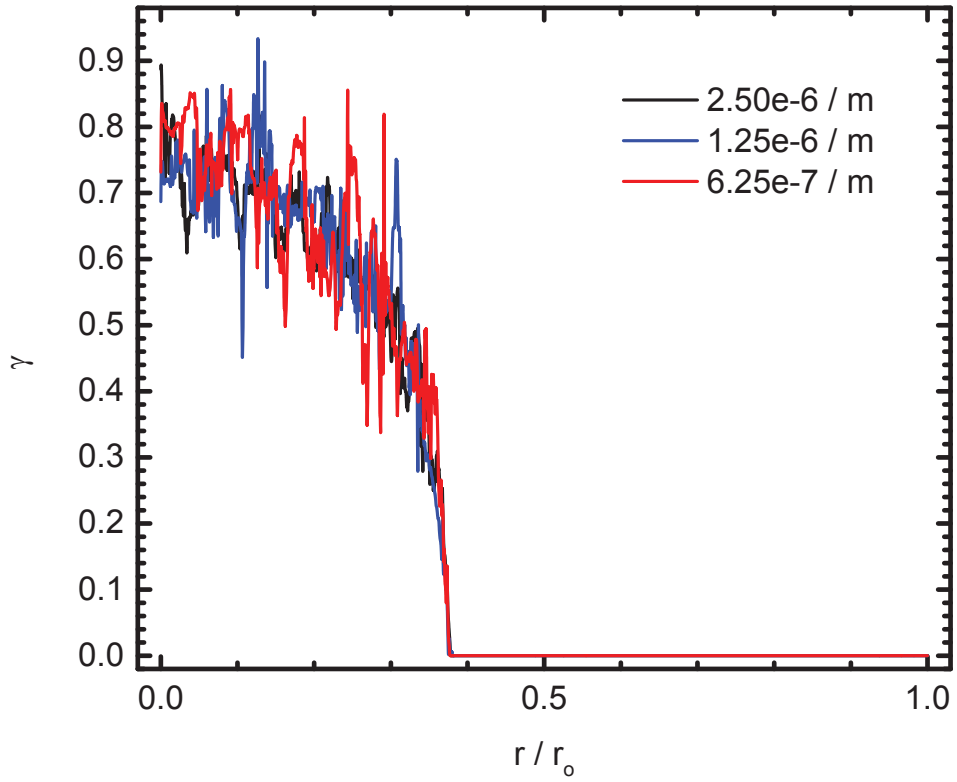

Figure 4-34. Radial distributions of calculated total current density at the electrode surface with maximum mesh element size as a parameter for the CO_2 Droplet model.

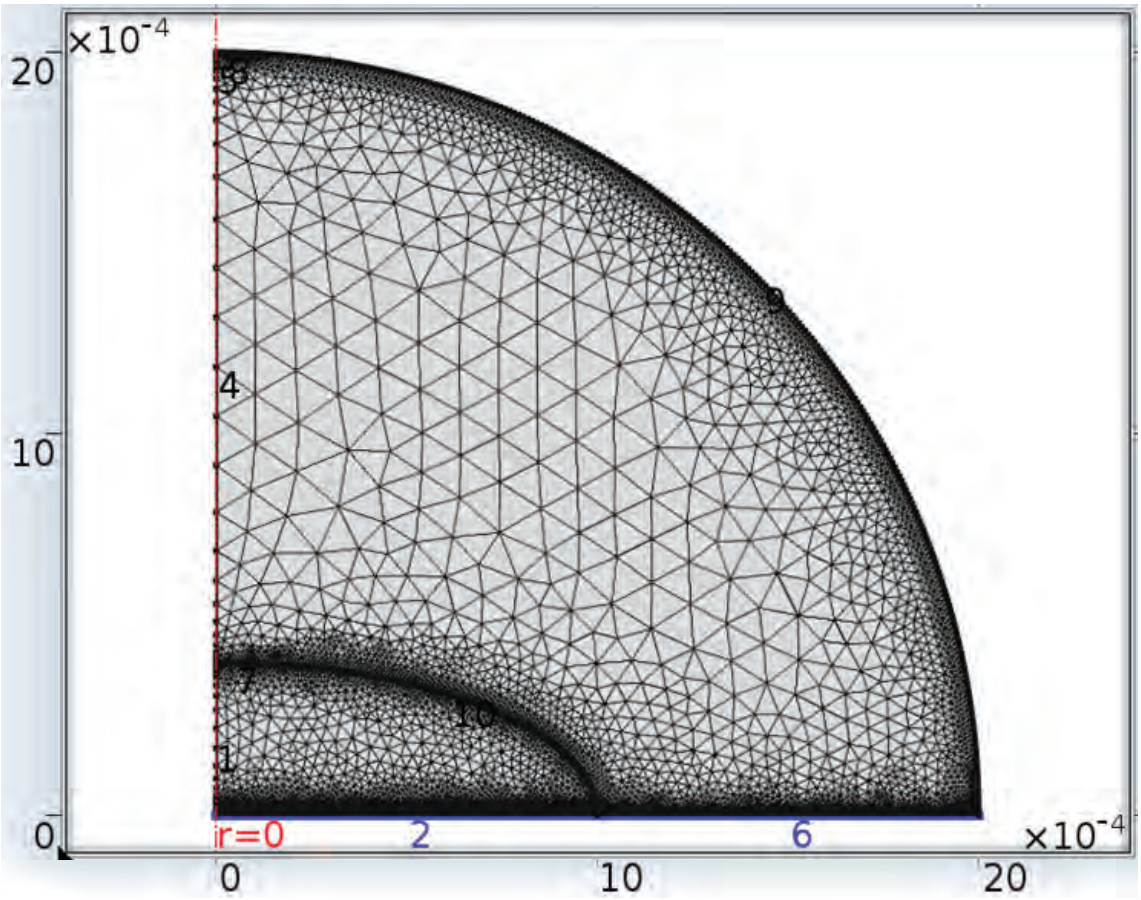

Figure 4-35. Schematic representation of the distributions of mesh density for the Deposit model.

finer mesh. However, the roughness of the results can be improved by using smaller time step as shown in Figure 4-32. For the Deposit model, the roughness of the curves can not be resolved by using smaller time step size. Singularity problems could occur at both the periphery and the interface of inner occluded and the outer bulk region for the Deposit model. Since the roughness appeared after the formation of precipitates, finer mesh size right above the metal surface was also employed as shown in Figure 4-35. However, employing finer mesh did not improve the roughness of the curves. It changes the results since the surface coverage since the current densities were coupling with the formation of $FeCO_3$. Figure 4-36 represents the distribution of surface coverage with maximum mesh element size as a parameter.

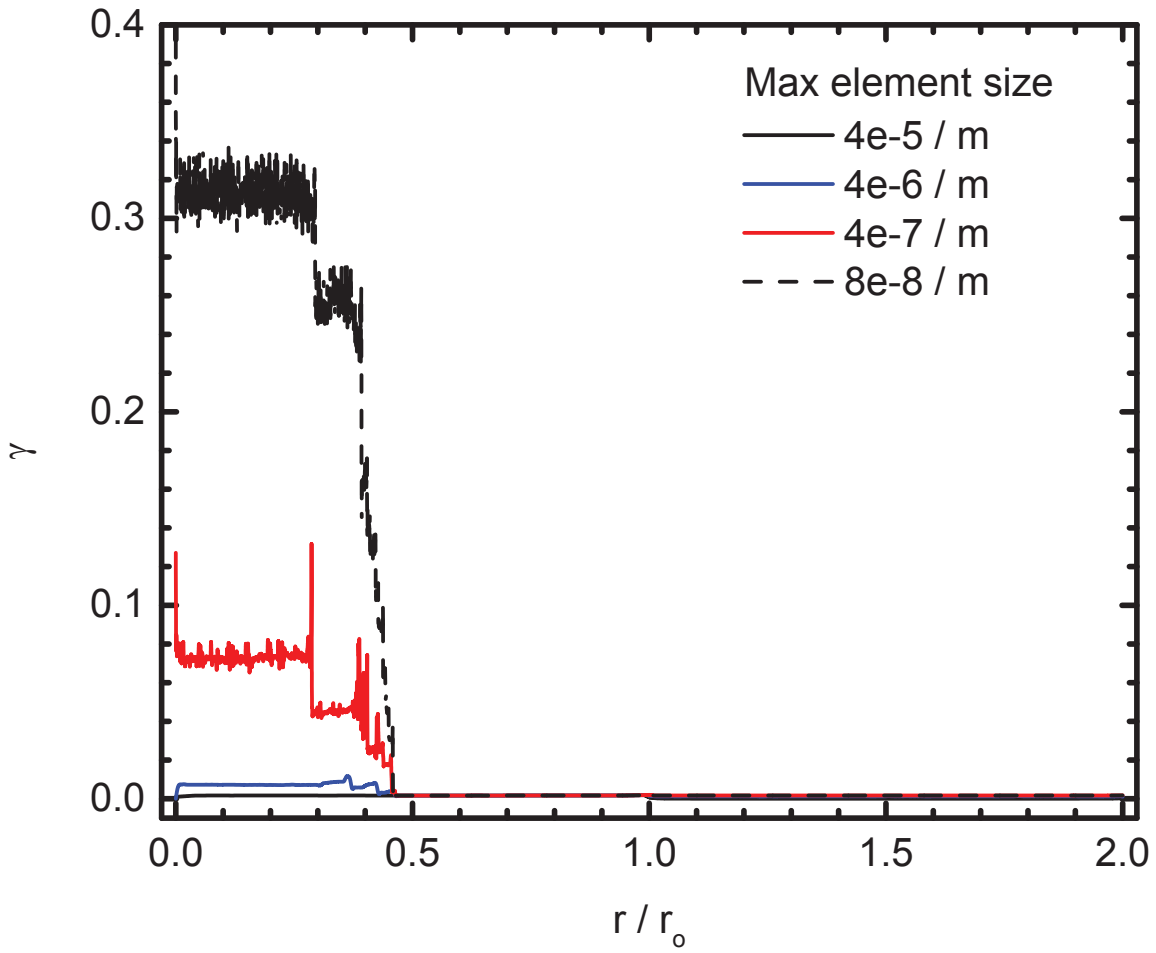

Figure 4-36. Radial distributions of calculated surface coverage at the electrode surface with maximum mesh element size as a parameter for the CO_2 Droplet model.

CHAPTER 5
OVERVIEW OF UNDER-DEPOSIT CORROSION MODEL

The under-deposit model can be categorized into Droplet and Deposit model by the physical configuration. Both Droplet and Deposit models were studied in aerated (O_2) and de-aerated (CO_2) media.

The Droplet model involved a complicated coupling of nonuniform mass transfer, potential distributions, and the active-passive transitions which was assumed to be resulted from the formation of precipitates. The solutions containing dissolved O_2 was used as the stepping stone to find the appropriate parameters, geometries, and mesh qualities. The polarization curves were plotted first to demonstrate the active-passive transitions with a series of applied potential at steady-state calculations. The importance of droplet size and shape and the mesh quality was addressed in the steady-state calculations. The concentration distributions of the dissolved gas vary along the metal surface since the diffusion path was different between the periphery and the center. This variation build up a concentration gradient and provides the driving force for the reactions. Maximum eccentricity was used to show the differential concentration cell behavior. A reasonable mesh size was applied to obtain correct results without costing significant calculation time. Finer mesh might be required when the complexity of the model increases in the model development, especially for the solutions containing dissolved CO_2. A time variable was introduced to study the distribution of reacting species at open-circuit potential. As time increases, the precipitates accumulated on the metal surface and distributed differently due to the mechanism of the involved reactions. In the presence of active-passive behavior, the center of the drop can remain active while the electrode near the edge of the drop passivates resulted from the formation of $Fe(OH)_2$ and $Fe(OH)_3$ for the O_2 model. For the CO_2 model, the precipitates started to form in the center since the insufficient concentration of CO_3^{2-} resulted from the dissociation steps of HCO_3^- and H_2CO_3.

The Deposit model is an extension of the Droplet model. The scale was enlarged to simulate an occluded region resulted from the corrosive deposits and sands inside a pipeline. The inner ellipse acts as an occluded region and is surrounded by a bulk system (outer ellipse). The covered area was treated as a porous medium, and the effective diffusion coefficient of species could be expressed by the Bruggeman approximation. The surrounding bulk solution was assumed to be a turbulent flow and could be described by adding the eddy diffusivity term. The cathodic reaction was preferred in the outer surface since the turbulent flow helped bring the dissolved gas on to metal surface; therefore, enhanced the iron dissolution in the occluded region.

The O_2 model is the stepping stone to construct the under-deposit corrosion model and the CO_2 model shows the capability of implementing the current model structure to different environments. Two mechanisms proposed by Remita and Nordsveen were studied for the solution containing dissolved CO_2. The mechanism proposed by Nordsveen was employed since it shows the corrosion occurring under the deposits. The CO_2 model involves more complex homogeneous reactions and electrochemical reactions. The dissolved O_2 provides a direct source for oxygen reduction in the O_2 model; while the hydration and dissociation reactions were required to provide H_2CO_3 and H^+ for cathodic reaction in CO_2 model. Smaller time step was required instead of finer mesh since the CO_2 involves more chemical reaction and have different reaction rates. With some modifications, this under-deposit model can applied to different conditions, such as solutions containing H_2S or both CO_2 and H_2S. The formation of precipitates and the local concentration values can be calculated if all the required parameters are given.

CHAPTER 6
CONCLUSIONS

This work provides a framework to study localized corrosion in aerated and de-aerated solutions. Unlike to other models [20, 47], a localized corrosion and the galvanic effect resulted from the formation of precipitates were studied in this work. The region of anodic and cathodic behavior was not assumed *a priori*. The active-passive transition was treated as a result of deposition of films composing of corrosion products. Time variable was introduced to study the formation and local distribution of precipitates. The ionic species was calculated by using conservation equations but, rather, by using Laplace's equation. Therefore, the local concentrations (pH), current density (corrosion rate), and the properties of precipitates can all be studied and correlated simultaneously. However, finer mesh and smaller time step are expected to be required to solve for conditions at higher temperature and pressure to study the galvanic coupling effect resulted from the protective precipitates.

This work studies interactions among chemical reactions, electrochemical reactions, deposition of films, and mass transport. The model development was sequentially presented in Chapter 3. The system containing dissolved oxygen was studied to build a basic structure for the under-deposit model. A similar approach with more complex homogeneous reactions were applied for system containing dissolved CO_2. Two geometries were used in system containing O_2 and CO_2 to study the formation of precipitates on the bare metal surface and the actual fluid effect on the metal surface with the preexisting deposits. The one-ellipse geometry, also called Droplet model in this work, was employed to study the differential concentration cells resulted from the concentration gradient of dissolved gas due to the diffusion path differences. The two-ellipse geometry, also called Deposit model in this work, was used to simulate the pipe flow and study the effect of the turbulent flow on the cathodic reactions.

Differential concentration cells were shown to be formed in both the Droplet model and the model of a predefined deposit surrounded by the turbulent flow. The differences of the diffusion behaviors in adjacent areas created two distinct environments and caused galvanic coupling. Calculations for a series of applied potential at steady-state were performed to show the active-passive transitions. In the presence of active-passive behavior, the anodic current shows the transition curve; whereas, the cathodic current displays the mass-transfer-limited plateau. Time-dependent calculations at the corrosion potential (open-circuit condition) were performed to study the formation of precipitates and the local concentrations and current density. For the Droplet model of both conditions containing O_2 and CO_2, the cathodic reactions are preferred at periphery region and corrosion occurs at the center due to the accessibility of dissolved gases. However, the distribution of precipitate for the O_2 and CO_2 models are different. For Droplet model containing O_2, the center of the drop can remain active while the electrode near the edge of the drop passivates by the accumulation of $Fe(OH)_2$. The species Fe^{2+} and OH^- reach the solubility product value near the cathodic reaction dominated region since OH^- is the product of oxygen dissociation. For the Droplet model containing CO_2, the species $FeCO_3$ began to accumulate in the anodic reaction dominated area because carbonate is a product of homogenous reaction. For the deposit model containing O_2, it shows a 0.1 / V potential drop resulted from the surrounding turbulent flow and the predefined deposit region. The corrosion occurred under the predefined deposit. Turbulent flow enhances the cathodic reactions in the bulk region because it brings the reacting species to the metal surface. Pitting potential may be observed if more corrosive conditions are given and therefore under-deposit corrosion may be one of the conditions for the initiation of pitting. For the Deposit model containing CO_2, unstable results were obtained since it involves more complicated reactions and singularity problems due to the boundary conditions and the water chemistry. More accurate results can be obtained with finer mesh and smaller time

step, but both require long calculation time and large cost of memory. Confirming the mesh size and time step is suggested to be the first step if any changes are made in the models. Finer mesh at the boundaries and smaller time steps for systems involving more complex reactions are also suggested. The maximum eccentricity of the droplet was suggested to be used to obtain the maximum concentration gradient of dissolved gases in this type of work. For the Deposit model, the area ratio of predefined deposit region to the bulk region is important. The larger ratio can generate larger potential drop and can lead us to more serious corrosion.

CHAPTER 7
SUGGESTIONS FOR FUTURE WORK

The model structure of the present work are used to propose additional steps for the continuation of this project. Solutions containing CO_2 can lead to more severe corrosion problem; therefore, the extension of the CO_2 model is proposed in Chapter 7. The CO_2 Droplet and CO_2 Deposit models are proposed to extend by using 3-D coordinates instead of 2-D axi-symmetric coordinates. Turbulent flow is suggested to be calculated in the channel flow model to study the corrosion with more realistic flow dynamics, such as the low-Reynolds number k-ε turbulence model in COMSOL Multiphysics. A new boundary condition are suggested to be included to simulate how defect expand with the calculated corrosion rate. More corrosive conditions containing more reacting species are suggested to also be studied.

7.1 2-D Axi-Symmetric to 3-D

The CO_2 Droplet and CO_2 Deposit models are proposed to extend from a 2-D axi-symmetric coordinates to a 3-D coordinates in COMSOL Multiphysics. A hemi-ellipsoid is suggested to be used in this calculation and the results can be compared with the 2-D axi-symmetric coordinates results. Non-symmetric geometry can also be calculated, the relationship between the shape and the onset of the formation of precipitates can be discussed. This model can provide a framework for the channel flow model in 3-D.

7.2 2-D Low-Reynolds Number k-ε Turbulence Model

The physical configuration of the previous model is suggested to be modified to simulate the flow dynamics in the pipelines more accurately. The schematic diagram of the channel flow model is shown in Figure 7-1. A 2-D coordinate can be used as the first step to validate the physics. A turbulence model which yields more accurate results for the flow close to the wall turbulent flow can be applied in this stage. Mass transfer boundary layer is often embedded inside momentum boundary layer for water system.

Figure 7-1. Schematic representations of the channel flow model.

In order to avoid the numerical difficulties in the momentum boundary layer, the first grid point of the calculation is always placed ”far” away from where major concentration gradient occurs. The estimated value for the concentration gradient at wall is less than the actual value. The wall flux of reacting species based on the boundary layer solution is

$$N_{wall} \approx -D\frac{C_b - C_s}{dx_2} \tag{7–1}$$

and the actual value should be described as

$$N_{wall} \approx -D\frac{C_b - C_s}{dx_1} \tag{7–2}$$

where dx_1 and dx_2 can be represented in Figure 7-2. The low-Reynolds number k$-\xi$ model is capable of calculating mass transfer with properly solving momentum transport and the calculation grid point can be place as close as possible to the wall surface. The build-in model The flow recirculation exists inside the predefined defect (the dark blue region in Figure 7-1) and the turbulent behavior can be described by applying the low-Reynolds number k-ε model built in COMSOL Multiphysics. Concentration cells formed due to the formation of precipitation where CO_2 is depleted, while other places are not.

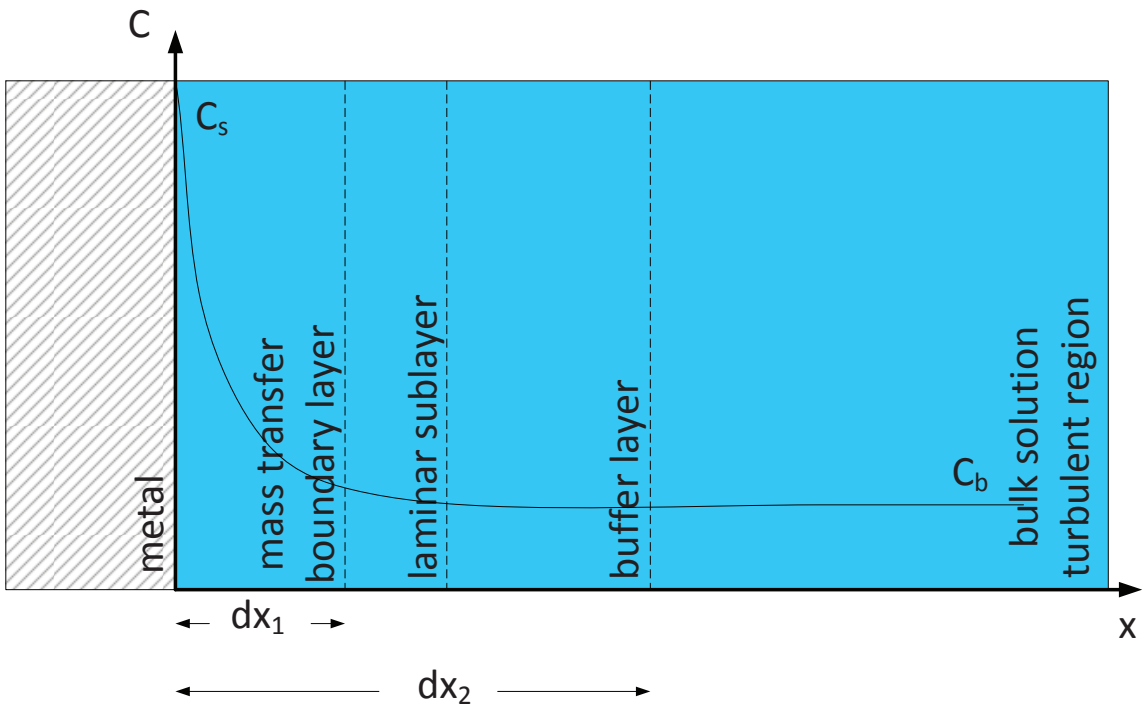

Figure 7-2. Schematic representations of concentration profile in turbulent flow.

7.3 3-D Low-Reynolds Number k-ε Turbulence Model

The 2-D channel flow model is proposed to be extended to a 3-D channel flow model. The metal surface in the predefined defect region acts as an anode and the cathodic reactions are dominated on the metal surface of the rest of the pipeline. The ratio of the size of the predefined defect to the radius and length of the pipeline plays an import role in this model.

7.4 Moving Boundary

The above model is proposed to be extended by replacing the predefined semi-circle defect with different shape of the defect and also employ the moving boundary conditions to study the defect expansion with calculated corrosion rate. The corrosion rate depends on the anodic current density and can be applied on the boundary of defect to predict the propagation of corrosion damage. Figure 7-3 shows the predefined defect region and the expansion of it when the moving boundary condition applied to the metal surface. The results are expected to be able to predict the

Figure 7-3. Schematic representations of the channel flow model with moving boundary conditions on the predefined defect.

size of the defect as time increases and can be compared with the experimental results. The changes in pH can be expected in this calculations.

7.5 More Corrosive Conditions

More corrosive conditions are proposed to be taken into account, such as solutions containing Cl^-, H_2S, and HS^-. The existence of chloride ions could lead us to study the pit initiation mechanism and the progression corrosion. Pitting corrosion could be the consequence of the protective film breakdown, which can be resulted from the water chemistry. Deficient O_2 or CO_2 and the existence of chlorides may enhance the breakdown of the passive film and pit propagation. Hydrogen sulfide can be more corrosive to stainless steel because not only the effect of increasing acidity but also the existence of other localized corrosion mechanism i.e., ”Sulfide Stress Cracking (SSC)”. At 25°C, two kinetics of the precipitation reaction between ferrous ions and dissolved sulfide were proposed by Rickard [64]. The first reaction can be expressed by

$$Fe^{2+} + H_2S = FeS_{(s)} + 2H^+ \tag{7–3}$$

and the other competing reaction can be represented by

$$Fe^{2+} + 2HS^- = Fe(HS)_{2(s)} \tag{7–4}$$

$$Fe(HS)_{2(s)} = FeS_{(s)} + H_2S \tag{7–5}$$

The mechanism of the formation of FeS at higher temperature was discussed in other places [65, 66].

REFERENCES

[1] *Pipline Accident Report: Natural Gas Pipeline Rupture and Fire Near Carlsbad, New Mexico August 19, 2000*, Technical report, National Transportation Safety Board, Washington, D.C. (2003).

[2] G. Koch, M. Brongers, N. Thompson, Y. Virmani, and J. Payer, *Corrosion Cost and Preventive Strategies in the United States*, Technical report, CC Technologies Laboratories and NACE International, Dublin, OH and Houston, TX (2001).

[3] N. H. N.P. Brown, *Slurry Handling: Design of Solid-liquid Systems*, 1st edition (London: Elsevier Applied Science: Springer, 1991).

[4] H. Lei, Z. Huang, W. Liang, Y. Mao, and P. Que, "Ultrasonic pig for submarine oil pipeline corrosion inspection," *Russian Journal of Nondestructive Testing*, **45** (2009) 285–291. 10.1134/S106183090904010X.

[5] R. Nyborg, "Overview of CO_2 Corrosion Models for Wells and Pipelines," in *Corrosion/2002*, 02-233 (Houston, TX: NACE International, 2002) 1–16.

[6] C. de Waard and D. E. Milliams, "Carbonic Acid Corrosion of Steel," *Corrosion*, **31** (1975) 177–181.

[7] L. G. S. Gray, B. G. Anderson, M. J. Danyxh, and P. G. Tremaine, "Mechanism of Carbon Steel Corrosion in Brines Containing Dissolved Carbon Dioxide at pH 4," in *Corrosion/1989*, 89-464 (Houston, TX: NACE International, 1989) 1–19.

[8] S. Nešić, M. Nordsveen, R. Nyborg, and A. Stangeland, "A Mechanistic Model for Carbon Dioxide Corrosion of Mild Steel in the Presence of Protective Iron Carbonate Films - Part 2: A Numerical Experiment," *Corrosion*, **59** (2003) 489–497.

[9] S. Nešić, J. Postlethwaite, and S. Olsen, "An Electrochemical Model for Prediction of Corrosion of Mild Steel in Aqueous Carbon Dioxide Solutions," *Corrosion*, **52** (1996) 280–294.

[10] A. Anderko and P. J. Shuler, "Modeling the Formation of Iron Sulfide Scales Using Thermodynamic Simulation Software," in *Corrosion/1998*, 98-064 (Houston, TX: NACE International, 1998) 1–15.

[11] S. Nešić, M. Nordsveen, R. Nyborg, and A. Stangeland, "A Mechanistic Model for CO_2 Corrosion with Protective Iron Carbonate Films," in *Corrosion/2001*, 01-040 (Houston, TX: NACE International, 2001) 1–28.

[12] G. Schmitt, T. Gudde, and E. Strobel-Effertz, "Fracture Mechanical Properties of CO_2 Corrosion Product Scales and Their Relation to Localized Corrosion," in *Corrosion/1996*, 96-009 (Houston, TX: NACE International, 1996) 1–21.

[13] R. Nyborg, “Initiation and Growth of Mesa Corrosion Attack During CO_2 Corrosion of Carbon Steel,” in *Corrosion/1998*, 98-048 (Houston, TX: NACE International, 1998) 1–11.

[14] J. Han, Y. Yang, B. Brown, and S. Nešić, “Electrochemical Investigation of Localized CO_2 Corrosion on Mild Steel,” in *Corrosion/2007*, 07-323 (Houston, TX: NACE International, 2007) 1–25.

[15] S. B. de Wexler and J. R. Galvele, “Anodic Behavior of Aluminum Straining and a Mechanism for Pitting,” *Journal of The Electrochemical Society*, **121** (1974) 1271–1276.

[16] J. R. Galvele, “Transport Processes in Passivity Breakdown - 2. Full Hydrolysis of the Metal Ions,” *Corrosion Science*, **21** (1981) 551 – 579.

[17] M. Alvarez and J. Galvele, “Pitting of High Purity Zinc and Pitting Potential Significance,” *Corrosion*, **32** (1976) 285 – 294.

[18] R. C. Alkire and D. Siitari, “Initiation of Crevice Corrosion,” *Journal of The Electrochemical Society*, **129** (1982) 488–496.

[19] S. Nešić and J. Postlethwaite, “Relationship between The Structure of Disturbed Flow and Erosion Corrosion,” *Corrosion*, **46** (1990) 874–880.

[20] J. Postlethwaite, S. Nešić, G. Adamopoulos, and D. Bergstrom, “Predictive Models for Erosion-Corrosion under Disturbed Flow Conditions,” *Corrosion Science*, **35** (1993) 627–633.

[21] R. Wood and T. Jones, “Investigations of Sand-Water Induced Erosive Wear of AISI 304L Stainless Steel Pipes by Pilot-Scale and Laboratory-Scale Testing,” *Wear*, **255** (2003) 206 – 218.

[22] R. Alkire, D. Ernsberger, and D. Damon, “The Role of Conductivity Variations Within Artificial Pits During Anodic Dissolution,” *Journal of The Electrochemical Society*, **123** (1976) 458–464.

[23] R. Alkire and D. Siitari, “The Location of Cathodic Reaction during Localized Corrosion,” *Journal of The Electrochemical Society*, **126** (1979) 15–22.

[24] U. R. Evans, *The Corrosion and Oxidation of Metals: Scientific Principles and Practical Applications* (London: E. Arnold Ltd., 1960).

[25] G. Hinds, P. Cooling, S. Zhou, and A. Turnbull, “Underdeposit Test Method for Assessing Performance of Corrosion Inhibitors,” in *EUROCORR 2008* (European Federation of Corrosion, 2008) 1–11.

[26] G. Hinds, P. Cooling, and A. Turnbull, “Testing of Inhibitors for Underdeposit Corrosion in Sour Conditions,” in *EUROCORR 2009* (European Federation of Corrosion, 2009) 1–9.

[27] R. Alkire and G. Nicolaides, “Differential Aeration Corrosion of a Passivating Metal under a Moist Film of Locally Variable Thickness,” *Journal of the Electrochemical Society*, **121** (1974) 183 – 190.

[28] F. LaQue, “Theoretical Studies and Laboratory Techniques in Sea Water Corrosion Testing Evaluation,” *Corrosion*, **13** (1957) 33 – 44.

[29] F. L. LaQue, “Electrochemistry and Corrosion (Research and Tests),” *Journal of The Electrochemical Society*, **116** (1969) 73C–77C.

[30] N. Vahdat and J. Newman, “Corrosion of an Iron Rotating Disk,” *Journal of the Electrochemical Society*, **120** (1973) 1682 – 1686.

[31] C. G. Law Jr. and J. Newman, “Corrosion of a Rotating Iron Disk in Laminar, Transition, and Fully Developed Turbulent Flow,” *Journal of the Electrochemical Society*, **133** (1986) 37 – 42.

[32] M. E. Orazem and M. G. Miller, “The Distribution of Current and Formation of a Salt Film on an Iron Disk below the Passivation Potential,” *Journal of The Electrochemical Society*, **134** (1987) 392–399.

[33] S. Srinivasan and R. D. Kane, “Prediction of Corrosivity of CO_2/H_2S Production Environments,” in *Corrosion/1996*, 96-11 (Houston, TX: NACE International, 1996) 1–23.

[34] M. B. Kermani and A. Morshed, “Carbon Dioxide Corrosion in Oil and Gas Production - A Compendium,” *Corrosion*, **59** (2003) 659–683.

[35] S. Nešić, “Key Issues Related to Modelling of Internal Corrosion of Oil and Gas Pipelines - A Review,” *Corrosion Science*, **49** (2007) 4308–4338.

[36] G. Schmitt and M. Hörstemeier, “Fundamental Aspects of CO_2 Metal Loss Corrosion - Part II: Mechanism,” in *Corrosion/2006*, 06-112 (Houston, TX: NACE International, 2006) 1–26.

[37] W. Sun, S. Nesic, and S. Papavinasam, “Kinetics of Iron Sulfide and Mixed Iron Sulfide/Carbonate Scale Precipitation in CO_2/H_2S Corrosion,” in *Corrosion/2006*, 06-644 (Houston, TX: NACE International, 2006) 1–26.

[38] J.-L. Crolet and M. Bonis, “Prediction of the Risks of CO_2 Corrosion in Oil and Fas Wells,” *SPE Production Engineering*, **6** (1991) 449 – 453.

[39] K. Videm and J. Kvarekval, “Corrosion of Carbon Steel in Carbon Dioxide-Saturated Solutions Containing Small Amounts of Hydrogen Sulfide,” *Corrosion*, **51** (1995) 260–269.

[40] S. N. B. Brown, S. R. Parakala, “CO_2 Corrosion in the Presence of Trace Amount of H_2S,” in *Corrosion/2004*, 04-736 (Houston, TX: NACE International, 2004) 1–27.

[41] A. Valdes, R. Case, M. Ramirez, and A. Ruiz, "The Effect of Small Amount of H_2S on CO_2 Corrosion of a Carbon Steel," in *Corrosion/1998*, 98-022 (Houston, TX: NACE International, 1998) 1–14.

[42] K. S. George and S. Nešić, "Investigation of Carbon Dioxide Corrosion of Mild Steel in the Presence of Acetic Acid - Part 1: Basic Mechanisms," *Corrosion*, **63** (2007) 178–186.

[43] J. O. Bockris, D. Drazic, and A. R. Despic, "The Electrode Kinetics of the Deposition and Dissolution of Iron," *Electrochimica Acta*, **4** (1961) 325–361.

[44] S. Nešić, N. Thevenot, J. Crolet, and D. Drazic, "Electrochemical Properties of Iron Dissolution in the Presence of CO_2 - Basics Revisited," in *Corrosion/1996*, 96-003 (Houston, TX: NACE International, 1996) 1–23.

[45] Y. Garsany, D. Pletcher, D. Sidorin, and W. M. Hedges, "Quantifying the Acetate-Enhanced Corrosion of Carbon Steel in Oilfield Brines," *Corrosion*, **60** (2004) 1155–1167.

[46] S. Nešić, B. F. M. Pots, J. Postlethwaite, and N. Thevenot, "Superposition of Diffusion and Chemical Reaction Controlled Limiting Currents - Application to CO_2 Corrosion," *The Journal of Corrosion Science and Engineering*, **1** (1995) Paper 3: 1–14.

[47] M. Nordsveen, S. Nešić, R. Nyborg, and A. Stangeland, "A Mechanistic Model for Carbon Dioxide Corrosion of Mild Steel in the Presence of Protective Iron Carbonate Films - Part 1: Theory and Verification," *Corrosion*, **59** (2003) 443–456.

[48] E. Dayalan, F. D. de Moraes, J. R. Shadley, S. A. Shirazi, and E. F. Rybicki, "CO_2 Corrosion Prediction in Pipe Flow Under $FeCO_3$ Scale-Formation Conditions," in *Corrosion/1998*, 98-051 (Houston, TX: NACE International, 1998) 1–19.

[49] E. W. J. van Hunnik, B. F. M. Pots, and E. L. J. A. Hendriksen, "The Formation of Protective $FeCO_3$ Corrosion Product Layer in CO_2 Corrosion," in *Corrosion/1996*, 96-006 (Houston, TX: NACE International, 1996) 1–22.

[50] J. S. Newman and K. E. Thomas-Alyea, *Electrochemical Systems* (John Wiley and Sons, Inc., 2004).

[51] S. Nešić and K.-L. J. Lee, "A Mechanistic Model for Carbon Dioxide Corrosion of Mild Steel in the Presence of Protective Iron Carbonate Films - Part 3: Film Growth Model," *Corrosion*, **59** (2003) 616–628.

[52] A. Anderko, "Simiulation of $FeCO_3$/FeS Scale Formation Using Thermodynamic and Electrochemical Models," in *Corrosion/2000*, 00-102 (Houston, TX: NACE International, 2000) 1–18.

[53] A. Anderko and R. D. Young, "Simulation of CO_2/H_2S Corrosion Using Thermodynamic and Electrochemical Models," in *Corrosion/1999*, 99-031 (Houston, TX: NACE International, 1999) 1–19.

[54] G. I. Ogundele and W. E. White, "Observations of the Influences of Dissolved Hydrocarbon Gases and Variable Water Chemistries on Corrosion of an API-L80 Steel," *Corrosion*, **43** (1987) 665–673.

[55] B. Linter and G. Burstein, "Reactions of pipeline steels in carbon dioxide solutions," *Corrosion Science*, **41** (1999) 117 – 139.

[56] C. de Waard, U. Lotz, and D. E. Milliams, "Predictive Model for CO2 Corrosion Engineering in Wet Natural Gas Pipelines," *Corrosion*, **47** (1991) 976–985.

[57] B. Mishra, S. Al-Hassan, D. L. Olson, and M. M. Salama, "Development of a Predictive Model for Activation-Controlled Corrosion of Steel in Solutions Containing Carbon Dioxide," *Corrosion*, **53** (1997) 852–859.

[58] E. Remita, B. Tribollet, E. Sutter, F. Ropital, X. Longaygue, J. Kittel, C. Taravel-Condat, and N. Desamais, "A Kinetic Model for CO2 Corrosion of Steel in Confined Aqueous Environments," *Journal of The Electrochemical Society*, **155** (2008) C41–C45.

[59] A. C. West, "Comparison of Modeling Approaches for a Porous Salt Film," *Journal of the Electrochemical Society*, **140** (1993) 403–408.

[60] G. Schmitt and M.Mueller, "Critical Wall Shear Stresses in CO2 Corrosion of Carbon Steel," in *Corrosion/1999*, 99044 (San Antonio, TX: NACE International, 1999) .

[61] W. G. Whitman, R. P. Russell, and G. H. B. Davis, "The Solubility of Ferrous Hydroxide and Its Effect upon Corrosion," *Journal of the American Chemical Society*, **47** (1925) 70–79.

[62] D. L. Leussing and I. M. Kolthoff, "The Solubility Product of Ferrous Hydroxide and the Ionization of the Aquo-Ferrous Ion," *Journal of the American Chemical Society*, **75** (1953) 2476–2479.

[63] R. B. Bird, W. E. Stewart, and E. N. Lightfoot, *Transport Phenomena* (New York: John Wiley & Sons, 1960).

[64] D. Rickard, "Kinetics of FeS Precipitation: Part 1. Competing Reaction Mechanisms," *Geochimica Cosmochimica Acta*, **59** (1995) 4367–4379.

[65] N. Harmandas and P. Koutsoukos, "The formation of iron(II) sulfides in aqueous solutions," *Journal of Crystal Growth*, **167** (1996) 719 – 724.

[66] H. Tokuda, D. Kuchar, N. Mihara, M. Kubota, H. Matsuda, and T. Fukuta, “Study on reaction kinetics and selective precipitation of Cu, Zn, Ni and Sn with $\{H2S\}$ in single-metal and multi-metal systems,” *Chemosphere*, **73** (2008) 1448 – 1452.

BIOGRAPHICAL SKETCH

Ya-Chiao (Jo) Chang graduated from the National Taiwan University with a Bachelor of Science degree in chemical engineering in 2008. She entered graduate school in August of 2008 at the University of Florida. In 2009, Jo pursued her doctorate in chemical engineering and joined Professor Mark Orazems research group which specializes in electrochemical engineering. In the summer of 2013, Jo had an internship in BP America. This internship allowed Jo to apply her under-deposit corrosion models to other systems which is an extension to her doctoral research. During her time at the University of Florida, Jo was married to Te-Yu Kao in 2013. She received her Ph.D. from the University of Florida in the fall of 2013.